Behavior of Fiber-Metal-Elastomer-Hybrid-Laminates

Zur Erlangung des akademischen Grades
Doktor der Ingenieurwissenschaften
der Fakultät für Maschinenbau
Karlsruher Institut für Technologie (KIT)

genehmigte
Dissertation
von

M.Sc. Matthias Stoll
aus Stuttgart

Tag der mündlichen Prüfung:	09. November 2018
Referent:	Prof. (apl.) Dr.-Ing. Kay André Weidenmann
Korreferent:	Prof. Dr.-Ing. Jürgen Fleischer

Preface

This work was conducted during my employment as research assistant in the group Hybrid and Lightweight materials at the Institute for Applied Materials - Materials Science and Engineering (IAM-WK) at the Karlsruhe Institute of Technology (KIT).
This work was supervised by Professor (apl.) Kay André Weidenmann and co-supervisor Prof. Dr.-Ing. Fleischer from the Institute for Production Science to whom I express my most sincere gratitude. The guidance, support and discussions were essential and the personal dedication to support the thesis and the constructive dialogues lead to success in the end.
I want to express my gratitude to the Baden-Württemberg Stiftung for financing this project allowing the research, which led to this manuscript.
I want to thank M.Sc. Sven Roth and Dipl.-Ing. Woramon Pangboonyanon for the collaboration concerning manufacturing, dialogues about our research fields and the willingness to do extra work.
My colleagues at IAM-WK deserve my deep gratitude for an extraordinary work atmosphere and collaboration. I thank M.Sc. Peter Rupp for the discussions in our office, which always led in the right direction.
Mr. Ralf Rössler, Marc Brecht, Arndt Hermeneit and Sebastian Höhne supported me throughout many technical problems. Additionally I want to thank all students, who worked with me either as a student assistant or during their thesis. To name are Jakob Technau, Manuel Kramar, Ina Kohlschreiber, Franziska Stemmer, Arnaud Feuvrier and Marian Weißschuh.
Finally I thank my family and my friends for their encouragement,support and motivation, without it this thesis would not have been written. I thank Vanessa for the patience and encouragement invested in me.

Kurzfassung

In Automobilen und in der Luftfahrt wurde in den letzten Jahrzehnten vermehrt auf Bauteile aus Faserverbundkunststoffen und hybriden Strukturen gesetzt. Ziel dieses Wandels waren höhere spezifische mechanische Eigenschaften, zur Gewichtsreduktion und Effizienzsteigerung. Eine Kombination von verschiedenen Materialien ermöglicht eine Struktur, die optimal zu der Belastung im Realfall passt. Eine Hybridstruktur kann durch die Kombination unterschiedlicher Materialklassen Eigenschaften erhalten, die nicht durch ein Einzelmaterial darstellbar sind.

Faser-Metall-Laminate (FML) werden in der Luftfahrt eingesetzt, da sie sehr geringe Rissausbreitungsgeschwindigkeiten zulassen, was zu erhöhten Lebensdauern und größerem Leichtbaupotential führen kann. Das bekannteste FML, Glass Laminate Aluminum Reinforced Epoxy (GLARE), besteht aus Aluminiumblechen und glasfaserverstärktem Epoxidharz.

Das größte Einsatzgebiet für das Laminat sind Passagierflugzeuge. Die Kombination der zwei sehr unterschiedlichen Materialien bringt die bereits genannten sehr guten dynamischen mechanischen Kennwerte.

Eine Verbesserung des Leichtbaupotentials des Laminats kann durch Substitution von Glasfasern durch Kohlenstofffasern erreicht werden, da Kohlenstofffasern höhere spezifische mechanische Eigenschaften besitzen. Allerdings erfordert der Einsatz von Kohlenstofffasern in einem Hybridlaminat eine Zwischenschicht, die die verschiedenen thermischen Ausdehnungskoeffizienten abfedern und gleichzeitig die Kontaktkorrosionsneigung senken kann. Es wurde eine Elastomerzwischenschicht eingefügt und hinsichtlich des Einflusses auf die Laminateigenschaften eingehend geprüft.

Die Prozessroute von GLARE im Autoklav führt zu langen Zykluszeiten, die durch eine neue Fertigungsroute drastisch reduziert werden sollten. Die neue, im Vergleich zu GLARE, kostengünstige Herstellungsroute führte zu fehlerfreien Bauteilen, wobei die Zykluszeit noch weiter reduziert wurde.
Die mechanischen Eigenschaften von Faser-Metall-Elastomer-Laminaten (FMEL) wurden hinsichtlich der Eigenschaften der Einzelmaterialien ermittelt. Ein besonderer Fokus lag auf der Grenzflächenanalyse unter diversen Lasten, um den Widerstand gegen Delamination zu beschreiben. Nach einer systematischen Materialauswahl wurden quasistatische Versuche genutzt, um die mechanischen Eigenschaften des Laminats im Vergleich zu einem Faser-Metall-Laminat (FML) ohne Elastomerschicht zu zeigen und den Einfluss der Zwischenschicht auf die mechanischen Eigenschaften vergleichend zu beleuchten. Die Experimente wurden von Infrarotbildgebung, CT-Scans und Digital Image Correlation (DIC) unterstützt. Die unterstützenden Messungen wurden genutzt um Schädigungen zu detektieren und die Schädigungsentwicklung zu visualisieren, was zu einem tieferen Verständnis der Eigenschaften und Mechanismen im Laminat führen sollte.
Die Eigenschaften der Einzelschichten und der Grenzflächen wurden genutzt, um das Laminatverhalten in dynamischen Experimenten vorherzusagen. Die dynamischen Versuche zeigten, dass durch die Elastomerzwischenschicht die mechanischen Eigenschaften des Laminats gesteigert werden konnten, da die duktile Zwischenschicht Delamination verhindern konnte. Die Ermüdungseigenschaften des FMEL konnten mit theoretischen Modellen validiert werden. Der Einfluss der Elastomerschicht wurde in Abhängigkeit des Versuchs beschrieben und die Eingeschaftsänderung des Laminats bewertet, um die Verbesserung des Laminats darzustellen. Die Integration der Elastomerschicht resultierte in reduzierten quasistatischen Eigenschaften, aber die dynamischen, Umwelt-, Grenzflächen- und Ermüdungseigenschaften konnten gesteigert werden.

Abstract

Components in automobiles and aviation have turned to fiber reinforced polymers and hybrid structures over the last decades. The desire to obtain high specific mechanical properties to reduce weight and gain efficiency is fueling this aspiration. The possibility to tailor materials to fit the application has also come to attention through combination of different materials and resulting in a hybrid material. A hybrid structure can show properties, which cannot be obtained by any single material. Fiber-Metal-Laminates (FML) found their application in aviation, because the extraordinary crack propagation properties resulted in longer life cycles and better lightweight potential. The most prominent FML is Glass Laminate Aluminum Reinforced Epoxy (GLARE), which consists of aluminum sheets and glass fiber reinforced epoxy. The combination of the two very different materials generates properties, which cannot be obtained by one bulk material. The laminate has extraordinary dynamic properties, such as very low crack propagation speed and high impact resistance. The laminate structure was desired to be further optimized through substituting the glass fibers with carbon fibers, which possess higher specific mechanical properties. The carbon fibers, however, force the integration of an interlayer, due to a mismatch of coefficients of thermal expansion and corrosive properties when paired with aluminum. In this study an elastomer interlayer was used and the effect of the interlayer on the laminate was thoroughly examined. A materials selection defined the constituents and the laminate succession as well as constituent thickness in the laminate. The mechanical performance of the fiber metal laminate with elastomer interlayers (FMEL) was examined concerning the effect of the constituent materials.

The laminates' mechanical properties were examined with a particular focus on the interfacial properties of the laminates under various loads to define the resistance against delamination. Quasi-static properties were used to qualify and describe all laminates concerning their lightweight potential, which was used to select the best laminate. The subsequent dynamic experiments were assisted by infrared imaging, x-ray computed tomography (CT) scans and digital image correlation (DIC). The assisting measurements were used to detect and describe the damage in the laminate to allow a deeper understanding of the laminate, its constituents and the interaction of the materials. The dynamic experiments presented an increase of mechanical properties caused by the integration of the elastomer layer, which prevented delamination through high strain. The constituents' and the interfacial properties were used to predict the laminates' behavior. The high fatigue properties of FMEL could be predicted by theoretical models. The impact of the elastomer interlayer on the laminate was examined to define benefits and disadvantages of the FMEL against the FML. The integration of the elastomer interlayer resulted in lower quasi-static, but higher interfacial, dynamic, environmental and fatigue properties.

Contents

List of symbols

Symbols

A, C	constants
b	width in mm
b_s	fatigue strength exponent
c	fatigue ductility exponent
δ	deflection in mm
ε	strain in %
ε_f	fatigue ductility coefficient in %
E	Young's Modulus or stiffness in GPa
E_0	initial stiffness in GPa
f	frequency in Hz
F	force in N
I_y	axial moment of inertia in mm^4
K_{bs}	equivalent bending-shear stiffness
K_m	plate membrane stiffness stiffness
l	length in mm
m	mass in kg
n	constant exponent
n_s	contact deformation stiffness
N_b	cycles to failure
ρ	density in g/cm^3
S	stiffness criterion in N/mm
σ	stress in MPa
σ_f	fatigue strength coefficient in MPa
t	thickness in mm
T	temperature in °C
v	volume fraction in the FRP
w	plate total transverse deflection at the center in mm

Indices

$(.)_f$	fiber
$(.)_m$	matrix
$(.)_{a,el}$	elastic amplitude
$(.)_{a,pl}$	plastic amplitude

Abbreviations

AFRP	Aramid Fiber Reinforced Polymer
ARALL	Aramid fiber Reinforced ALuminum Laminate
CAI	Compression After Impact
CARALL	CArbon fiber Reinforced ALuminum Laminate
CFRP	Carbon Fiber Reinforced Polymer
CLT	Classical Laminate Theory
CT	Computed x-ray Tomography
CTE-mismatch	mismatch of Coefficients of Thermal Expansion
DCB	Double Cantilever Beam
DIC	Digital Image Correlation
DIN	German Institute for Standardization
EN	European Organization for Standardization
FMEL	Fiber Metal Laminate with Elastomer interlayer
FML	Fiber Metal Laminate
FRP	Fiber Reinforced Polymer
GFRP	Glass Fiber Reinforced Polymer
GLARE	Glass Laminate Aluminum Reinforced Epoxy
ISO	International Organization for Standardization
NCF	Non-Crimp Fabric
QI	Quasi-Isotropic
TMF	Thermal-Mechanical Fatigue
UTS	Ultimate Tensile Strength

1 Introduction

1.1 Motivation

A worldwide trend to reduce the consumption of resources using lightweight constructions initiate engineers to thrive towards new materials, structures and processes to reduce harm to the environment. The weight reduction of a structure in automobiles or aircrafts benefits the fuel efficiency. Lightweight structures can either be obtained by using materials with a low density or by optimized load bearing design. The best suited material for a certain load, which is predominant in an application, defines the lightweight potential for this structure. Therefore, new materials or structures consisting of multiple materials are researched to find better materials for higher efficiency.
Fiber reinforced polymers (FRP) become more widely used due to the low density of the polymer matrix and the high mechanical properties of the fiber. Glass fiber or carbon fiber reinforced polymers are most widely used. Carbon fibers have a higher stiffness and lower density compared to the cheaper glass fiber. The FRP allows thin walled structures to use the axial moment of inertia to assist the mechanical properties of the fibers. Continuous fibers and load path oriented design of the anisotropic FRP enable possibilities to reduce weight.
FRP components are inferior in certain applications compared to other materials, which can be caused by unwanted failure mechanisms, dynamic properties or issues with environmental loads. Thus, a combination of materials can be used to combine the benefit of each material. Fiber-Metal-Laminates (FML) exhibit properties, where they behave far superior compared to bulk materials, thus, resulting in a widespread application in aircraft fuselages.

These commercially available Fiber-Metal-Laminates are called GLARE (Glass Laminate Aluminum Reinforced Epoxy). They combine aluminum and glass fiber reinforced epoxy, and found their application in aviation [1, 2, 3] due to unique mechanical behavior. The combination of the beneficial properties of the constituents caused the hybrid material to be superior in crack propagation resistance and impact damage at low densities.
In specific applications, such as aviation, quasi-static properties are less important for the materials selection of a component compared to dynamic properties, like crack propagation rates. The low crack propagation rates are caused by the FRP component and the interfacial properties between the constituent materials. The FRP has a fiber bridging effect and the interface acts as a crack stopper. These properties are not material dependent, therefore materials could be substituted to enhance the performance of the laminate in mechanical properties other than crack propagation.
Additionally to the failure mechanisms, the component weight is important in aviation, thus, limiting the constituents to lightweight materials. The FML used for this study was optimized for lightweight potential in order to reduce material and resources.
The lightweight optimization pairs the laminate materials to the anticipated loads in application. Therefore, the circumstances in application need to be known to tailor the laminate to desired needs. A laminate is predominantly loaded in bending, which shall be used for the materials selection. GLARE can be optimized to reach the maximum possible lightweight potential by substituting the glass fibers with carbon fibers.
However, CFRP paired with aluminum causes mismatch of coefficients of thermal expansion [1, 4]. The electrical potential between the constituents allows galvanic corrosion [5, 6]. This explains the selection of glass fibers to manufacture GLARE, which also have a significantly lower price.
In order to use CFRP in an FML, the CTE-mismatch and galvanic corrosion have to be suppressed, which can either be accomplished by substituting the metal layer or introducing an interlayer.

In this work an elastomer interlayer was chosen to be thoroughly characterized. The elastomer interlayer was stacked between the CFRP and aluminum layer before consolidation to increase adhesion, balance the CTE-mismatch and also inhibit corrosion by electrical decoupling. Subsequently the mechanical performance of the laminate with elastomer interlayers was evaluated against FML without interlayers to define the benefits and shortcomings of the new laminate.

1.2 Objective

The objective of this work was to systematically characterize Fiber-Metal-Laminates with elastomer interlayers (FMEL) in order to describe and predict the mechanical properties and failure mechanisms under various loadings. The laminate was desired to be a novel, sustainable material concept for automobile lightweight design in the scope of resource and material efficiency, due to high lightweight potential, load compatible design and optimized process cycle times. FML using CFRP will be manufactured to evaluate the effect of the interlayer, while the FMEL will also be compared to GLARE.

The laminate layup and its constituents were first selected for lightweight sheets under flexural loading using CES EduPack and its tool Hybrid Synthesizer from Granta Design Limited. One laminate structure is shown in figure 1.1. The laminates were manufactured using a novel process route for FML, characterized to detect manufacturing defects and to define the optimum manufacturing process. Subsequently, the micro-structure as well as the interfaces were examined to evaluate the laminates and find the best option. The laminate's behavior was investigated in quasi-static and dynamic loading leading to damage evolution and thermal-mechanical fatigue.

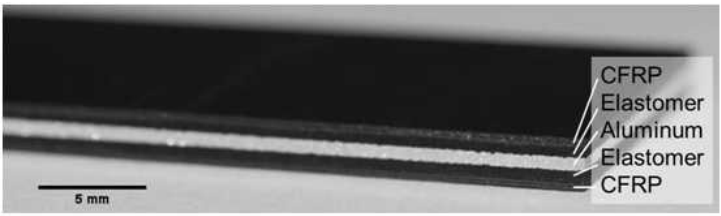

Figure 1.1: A 5-layer symmetrical FMEL specimen with CFRP face layers, aluminum core and elastomer interlayers

The final result, whether the inclusion of the elastomer in an FML, lead to an improvement compared to GLARE, CARALL and ARALL was evaluated with respect to a variety of mechanical, thermal and environmental loads.

2 State of research

2.1 Description of hybrid materials and laminates

Composite materials can be defined with the following statement: Composite materials are macroscopically quasi-homogeneous materials, which consist of two or more insoluble components. Furthermore, a hybrid composite is defined as a combination of multiple materials from different material classes, but one has to be a composite [7].
Composites generally consist of two or more components, where each material has specific duties for the structure. The properties of the composite are different from the properties of the individual components and can be tailored to generate a desired behavior. Often high specific mechanical properties are achieved with composite structures [7]. A large group within the composites is the subset of the fiber reinforced polymers (FRP). In FRP the fiber is used as a reinforcing structure to carry mechanical loads. The matrix embeds the reinforcing component and its primary task is to introduce the load into the fiber. Additionally, the matrix is used to protect the often delicate reinforcing structures from environmental harm.
The fibers define the mechanical properties of the composite, because the mechanical properties of the reinforcement are generally significantly higher than the properties of the matrix. Fibers are defined by a high length to thickness ratio, which exceeds 1000 to enable load transfer. The highest mechanical properties can be achieved using continuous fibers. A fiber is called continuous, when the length of the fiber is equal to the dimensions of the manufactured component. Technical fibers are used more frequently than natural fibers, because of easier handling, more consistent mechanical

properties and better availability. Common fiber materials are glass, aramid and carbon. These fiber materials have high strength and low density in common, which qualifies them for lightweight applications. Glass fibers are reasonably cheap with an approximate stiffness of 70 GPa and are the most frequently used fiber type. Carbon fibers possess a higher stiffness and lower density, which results in better suitability for lightweight design. However, the price of carbon fibers is significantly higher compared to glass fibers. Aramid fibers are polymer fibers with a low density and high strain, but also high costs and a intermediate stiffness. Therefore, the fibers in the FRP are selected based on the application.

The composites are categorized by the matrix material. Thus, ceramic, metal and polymer matrix composites exist. The polymer matrix composites benefit from low density, low price and established manufacturing processes.

A combination of a composite material and another material from a different materials class is called a hybrid. Common examples for hybrids are sandwich structures with FRP face sheets and a metal foam core or laminate structures with metal and FRP layers. A hybrid structure can also be represented by a locally reinforced FRP with material from a different class. Laminates consisting of FRP and metal are one subset of hybrids. The hybridization is achieved by stacking and adhesive bonding of the constituents. Laminates generally consist of bulk constituent materials and are used in sheets [8]. The hybridization leads to hybrid interfaces, where the metal and fiber reinforced polymer are joined. These interfaces are more extensive in laminates compared to other hybrid structures and impact the mechanical behavior on a larger scale. Reduced interfacial properties can result in premature delamination. Hybrids feature specific problems in the interface due to the pairing of different materials. The interface between the constituents generally is loaded by a mismatch of coefficients of thermal expansion, has a danger of corrosion and the quality of the interface is defined by the adhesive properties.

A mismatch of the coefficient of thermal expansion combined with a temperature change causes interfacial stress. A difference in chemical potential of the constituents and the contact with an electrolyte can cause galvanic corrosion. Additionally flexural loads are often primarily applied to the sheet, which result in shear stress in the interface. All the loads mentioned above can cause premature delamination and therefore, the characterization and optimization of the hybrid interface is crucial for a high-performance laminate.

2.2 General properties and applications of Fiber-Metal-Laminates

Fiber-Metal-Laminates (FML) generally consist of fiber reinforced polymers (FRP) and metal sheets [9]. The metal constituent in the laminates is often aluminum, steel or titanium. Aluminum is used based on the low density and cost [5]. Steel sheets have the disadvantage of high densities, but have a lower price and high overall properties [10]. Titanium is included because of thermal and corrosive properties [11].
The mechanical properties of the laminates highly depend on the constituents, but interfacial properties are essential for premature failure. Vogelesang et al. showed that delamination caused by impact damage would cause a stiffness decrease and failure prior to reaching the usual lifetime [1]. The interface can be weakened by environmental circumstances. The carbon fibers can introduce risk of galvanic corrosion, as the electrical potential of the components were found to promote corrosion [12] or delamination due to a mismatch of coefficients of thermal expansion (CTE-mismatch) [13].
Adhesion problems of the aramid fiber to the matrix are shown by the aramid fiber. Additionally did delamination occur in the hybrid interface during fatigue loading, which was caused by low adhesive properties [14]. A resin rich layer is positioned close to the aluminum to increase adhesion [14].

A positive aspect caused by the interface is an increased crack propagation resistance. Vlot et al. showed, that the crack stopping effect hinders cracks propagating through one material from entering adjacent materials [2], while Rodi et al. described the fiber bridging effect in FRP, which reduces crack tip stress due lower crack tip opening angles [15].

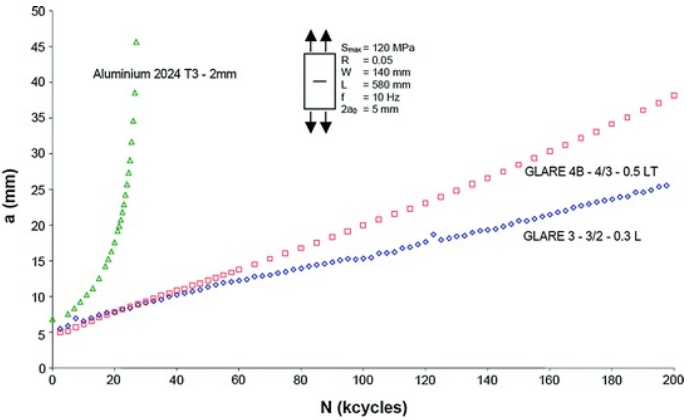

Figure 2.1: Fatigue crack propagation properties of GLARE compared to bulk aluminum [2]

The combination of both crack propagation resistance effects generates a low crack propagation rate of GLARE compared to bulk aluminum, which is displayed in figure 2.1. Hence, FML is found in aircrafts where the dynamic properties like the crack propagation rate are crucial. In aviation a low density has to be ensured to achieve high specific properties, therefore the combination of aluminum and glass fiber reinforced polymer (GFRP) is preferred [16]. The properties of the FML can be tailored to the needs by the selection of suited constituents. However, for many applications FML are still too expensive and the process cycle time is too long. To broaden the scope of FML, the process cycle times and the costs have to be reduced.

2.3 Manufacturing process for Fiber-Metal-Laminates

Fiber-metal-laminates are usually manufactured in large sheets, which are dimensionally close to the finished structural component, because the plastic formability of conventional FML after curing is low.
Hand lay-up is mostly used, where the fiber texiles are placed on the metal sheet and impregnated by hand, before the laminate is placed in the autoclave to cure. However, for good adhesion of the metal sheets to the polymer resin, the metal has to be pretreated elaborately.
The hand lay-up allows the constituents to be stacked according to the desired laminate succession. The curing cycle is carried out in an autoclave, where the polymer matrix of the FRP component is cured at elevated temperature and pressure [17].

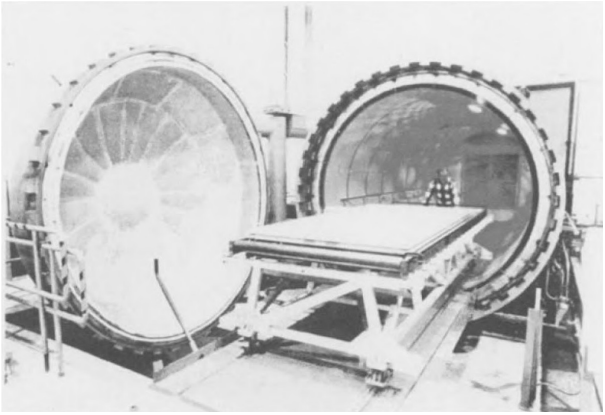

Figure 2.2: Autoclave with a GLARE sheet for consolidation [2]

The laminate in an autoclave is presented in figure 2.2, which indicates the comparably slow heating rate due to the large structure. The cycle time of the autoclave is largely affected by the heating and cooling between ambient and processing temperature as well as the long curing of the polymer.

The resulting cycle time is comparably high leading to high production costs which are also increased by the marginal automation of the process. The applications for FML could increase with a more cost effective process route. Vlot et al. and Sinke et al. indicated that it would broaden the application spectrum of FML, if the laminate could be manufactured in shorter cycles [2, 17]. A vacuum assisted technique can be used to obtain cycle times of under one hour.

Cycle time optimization

The high cycle time of the conventional FML, caused by the autoclave process and hand lay-up, leads to high production costs. The hand lay-up itself requires a long time, but also requires the resin to have a long potlife to inhibit premature curing during impregnation. The resulting curing cycle is longer due to the longer potlife. To optimize the cycle time, a different manufacturing process has to be used to allow the use of a fast curing resin. The time consuming surface treatment step of the metal layer can be avoided using an interlayer.
Fast curing resins are often consolidated with machine presses, which apply temperature and pressure for good mechanical properties in short curing cycles [7].

Forming of FML

Commercial FML can only be formed within strict boundaries, because sheet forming technologies cannot be used due to fiber fracture as shown in figure 2.3. Jong et al. showed that forming of GLARE can lead to fracture in the GFRP at high degrees of forming [18]. Figure 2.3 visualizes the formed laminate at an approximate radius of 10 mm, which led to cracks in the GFRP constituent. Therefore, FML can only used in slightly curved sheets.

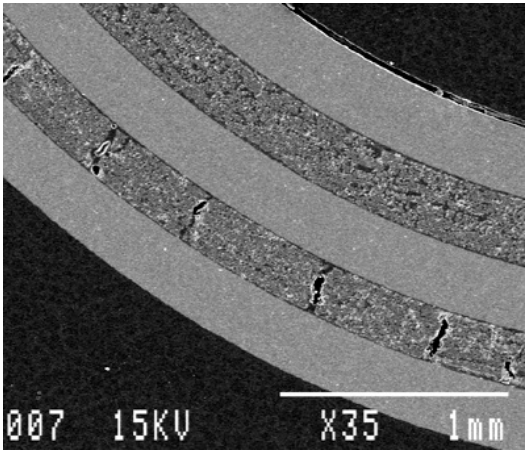

Figure 2.3: Cracks in the GFRP constituent of GLARE after forming [18]

The hand lay-up in a form can feature a slight forming radius, but no complex geometries are achievable [17]. Additionally, the forming before curing is neglected to preserve the fiber architecture.
Forming post curing resulted in slightly curved sheets, as [2] presented for the use as an aircraft fuselage. A double curved sheet can be obtained by strech forming [19]. The forming techniques are sketched in figure 2.5.

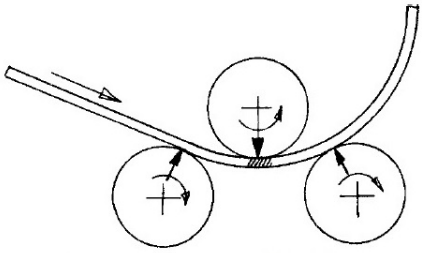

Figure 2.4: Schematic of roll forming used for cured GLARE sheets [17]

Roll forming is continuous forming process to obtain a desired curvature for single curved shells. The possibility to form GLARE in this process was proven [17], but the achievable curvature is low. GLARE with a roll radius below 1 m was not attempted, due to damage in the laminate at higher radii.

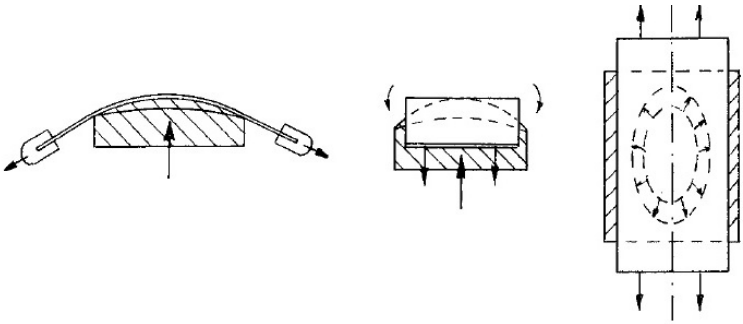

Figure 2.5: Schematic of stretch forming to form cured GLARE sheets [17]

Stretch forming is a technology to obtain double curved shells. Due to the low strain to failure of the glass fiber and the brittle interface, the forming radius of the FML is low [18]. Three point bending was used to simplify the forming step to experimentally obtain the minimum forming radius. Fiber failure was observed at a forming radius of 10 mm and a forming angle of 90 °. More complex geometries, meaning lower forming radii, can be achieved by using formed metal sheets and draping the GFRP onto them before curing. However, only three layer laminates were manufactured and then stacked to form the final dimensions of the component [17].

FML with small forming radii can be manufactured as visualized in figure 2.6. The manufacturing process used coaxial metal tubes or formed sheets and an FRP component. The FRP was draped onto the metal and then cured under pressure to obtain the laminate. The resulting structure only had three layers and needed to be stacked and glued for higher thicknesses [17].

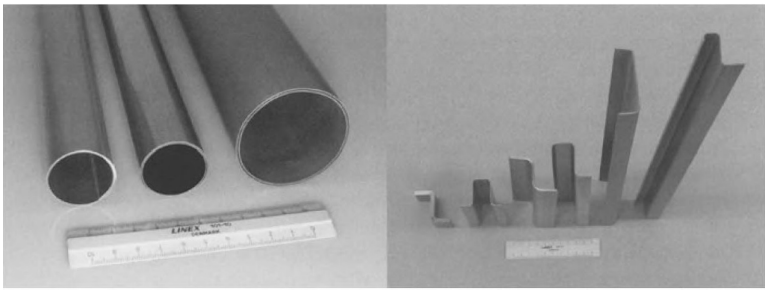

Figure 2.6: GFRP layers manufactured onto already formed metal tubes or sheets to obtain higher complexity in GLARE structures but using one alternative manufacturing process [17]

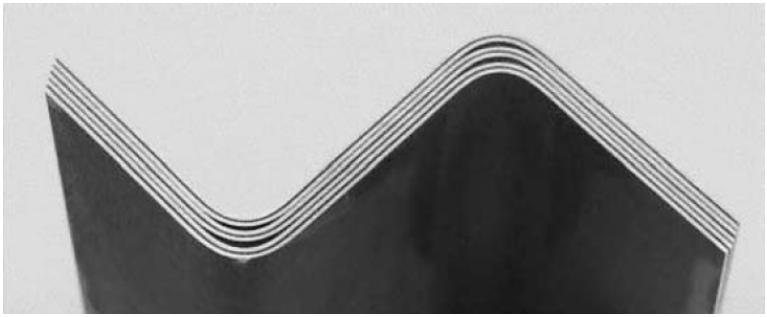

Figure 2.7: GLARE stringer built by stacking of the alternatively manufactured three-layer laminates [17]

Figure 2.7 visualizes the three-layer laminates stacked and adhesively bonded to form a stringer. The voids in the radii are negative but have to be accepted at the high degree of forming [17].

2.4 Components of Fiber-Metal-Laminates

The constituent materials and the layer succession define the mechanical properties of the laminate. The FML can have lower quasi-static properties compared to bulk materials, but the extraordinary dynamic properties generally surpass bulk materials. The stiffness of the GFRP is approximately 35 GPa, which reduces the stiffness of the aluminum from 73 GPa to 60 GPa in GLARE with 0.5 mm aluminum layers and 0.25 mm GFRP layers [20]. However, the properties presented in figure 2.1 show superior behavior.
Aluminum constituents feature high specific properties at a low price of approximately 2 €/kg, because comparable lightweight metals like magnesium and titanium resulted in prices of 5 €/kg respectively 20 €/kg. Titanium can be paired with CFRP to obtain laminates with a stiffness of 100 GPa compared to the lower stiffness of GLARE (60 GPa). The substitution of the metal and fiber result in an increase of the laminate stiffness [11]. However, the combination of CFRP and aluminum needs an interlayer against corrosion. Wang et al. showed that the corrosion in a galvanic cell was inhibited by a sol-gel coating [12]. The aramid fiber offers high strength of 3000 MPa to 3500 MPa and a low density of 1.44 g/cm^3. The low density can result in higher lightweight potential in the laminate [21].

2.4.1 Fiber reinforced polymer

Fiber reinforced polymers (FRP) consist of an embedding matrix and reinforcing fibers and the FRP constituent is used in FML for the fiber bridging mechanism. The FRP is an anisotropic material, because the orientation of the fibers define the mechanical properties [7]. The fiber orientation in FML is often biaxial to ensure a symmetrical laminate and good mechanical properties in two directions. The warpage, which results from asymmetrical shrinkage due to the fiber orientation is acceptably low in biaxial layups, but has to be monitored in highly oriented laminates [2].

The matrix needs to envelop every fiber perfectly with a good interface to be able to introduce load and prevent environmental damage [22].
The fibers used as reinforcement should have a high stiffness and strength combined with low density to be applicable for lightweight design. The fiber-matrix-adhesion is a crucial factor in the FRP, therefore often resin systems are optimized for specific fiber types. Thermosets, such as epoxy, are used in structural applications with either glass or carbon fibers, because the low viscosity ensures a good impregnation. Mostly epoxy resin was used in FML with glass fiber in GLARE, where lower quasi-static properties were obtained compared to aluminum, but the dynamic properties surpassed aluminum. Especially crack propagation properties of GLARE were superior to monolithic materials [2].
ARALL used aramid fibers, which resulted in a higher stiffness than GLARE, but lower than aluminum. The crack propagation properties were better than bulk aluminum. However, GLARE surpassed ARALL in fatigue crack properties. Adhesive problems in the hybrid interface and between fiber and matrix show the need for a resin rich interlayer to oppose delamination [14].
Unusual because of interfacial problems is the combination of carbon fibers and aluminum in CARALL, because the coefficients of thermal expansion differ and the possibility of galvanic corrosion exists. The CTE-mismatch can cause delamination, which occurred widely in the laminates [2].
Because of interfacial problems in CARALL and ahesion problems in ARALL, GLARE is used most widely in commercial applications.
Rarely thermoplastic polymers were used in FML, but the combination of titanium with carbon fibers led to the selection of PEEK. The thermoplastic matrix was selected to reduce process cycle times and increase the adhesion in the hybrid interface. Additionally was the adhesion increased by sand blasting [11, 23].

2.4.2 Metal

The isotropic metal layer in the laminate is able to endure high strains compared to the FRP. Often a metal face sheet is used to ensure varnishing and welding.
In commercial FML aluminum is used [2], but research FML may use others metals like steel. Steel sheets with polymer interlayers increased the damping of the laminate [10]. Steel layers were used as reinforcements in GLARE, when higher load bearing capability was desired. The laminate surpassed GLARE in mechanical properties, however, specific properties were not analyzed [24].
Titanium combined with PEEK results in laminates for high temperature applications and can be used for supersonic aerospace components. The adhesion is adapted to obtain high mechanical properties [11]. Rhymer et al. showed that the interface needed to be improved with alkaline-perborate treatment to prevent delamination in fatigue experiments [25].
Usually lightweight metals are used with a high stiffness to density ratio. Magnesium features a low density of $1.75\,\mathrm{g/cm^3}$, which qualifies for lightweight application. The laminate in combination with PEEK-CF has a low overall density, but the low static strength and fatigue properties of the metal sheet nullified the advantage [26].
For lightweight applications the low density aluminum is often selected, while steel is the cheapest material and will be selected if the weight is a secondary concern. Titanium and Magnesium are more difficult to include in manufacturing processes and the prices are higher, therefore these metals can be included in laminates for special applications.

2.4.3 Interface

The interface between FRP and metal layers is a crucial adhesive bond defining the structural integrity of the laminate, which needs to be optimized to inhibit premature failure. As it is a possible weak point, it needs to be evaluated and characterized to properly define the mechanical behavior of the laminate.
The interfacial properties depend on the matrix and the metal layer. Aluminum can be pretreated for the adhesion to epoxy [2]. The surface roughness was increased for mechanical interlocking and led to a maximum increase of shear strength of 33 % when the areal roughness was increased from 2 μm to 6 μm [27].
Steel interfaces can be enhanced for adhesion with the matrix by anodizing treatments, which resulted in cohesive failure and therefore excellent interfacial properties. The laminate with pretreatment showed a reduction of interfacial properties after ageing at 70 °C and 98 % relative humidity, but still surpassed the laminate without pretreatment [28].
The metal layers are generally pretreated to increase adhesion to the FRP in order to maximize the laminate properties and prevent premature failure.

2.5 Fiber-Metal-Laminates

Fiber-Metal-Laminates found their application in aviation due to a 20 % weight reduction compared to established aircraft materials and a simultaneous increase in fatigue properties. Splicing of GLARE can save additionally 20 % to 50 % compared to mechanical fastening techniques. The high strength of GLARE, which can be over 1000 MPa is significantly higher than the strength of an aluminum sheet at 430 MPa [5].

The fatigue crack propagation properties are excellent compared to bulk materials increasing the fatigue crack properties by a factor of five [2]. GLARE exhibited better safety properties compared to aluminum, because the fracture toughness behavior showed that an engine rotor failure is less critical with GLARE than with aluminum. Also did GLARE increase the fire safety, as the aluminum layer would melt off and the epoxy degrade, but the glass fibers retained the fire to the outside and kept the passengers safe. An additional benefit can be splicing as a cost effective joining method compared to riveting [29].

Additionally to the commercially available GLARE there are laminates manufactured for research purposes. Carbon fibers are paired with aluminum to enhance the specific mechanical properties by reducing the fiber density by 26 % and increasing the stiffness of the biaxial FRP constituent from 35 GPa to 65 GPa, which could be further increased with high modulus carbon fibers [30].CARALL has the danger of galvanic corrosion due to the electrical potential between the carbon fiber and aluminum sheet. The CFRP has to be electrically decoupled from the aluminum sheet using an interlayer, as presented by Wang et al. [12].

The CTE-mismatch between CFRP and aluminum can also damage the laminate. Lin et al. presented residual stress in the laminate caused by the CTE-mismatch of the constituents and the cooling from processing temperature. The resulting interfacial load can reduce the mechanical properties of the laminate [13]. ARALL showed good fatigue crack propagation properties compared to bulk aluminum, but like in GLARE, was the static stiffness below aluminum. ARALL also exhibited fiber-matrix adhesion problems and low interfacial properties between the metal and AFRP layer, which were increased using a resin rich interlayer [21, 30].

Although ARALL had promising properties compared to conventional aircraft materials, GLARE surpassed ARALL in residual strength after imapct and fatigue crack propagation properties. These results led to the application of GLARE over ARALL [31].

FML with different metal layers than aluminum are comparably rare, but the integration of steel in a laminate showed the possibility to increase load bearing capability [24]. However, the specific mechanical properties, which take the high density of steel into account were not increased.
Titanium in combination with CFRP was analyzed for high temperature applications in supersonic aerospace components. The interfacial properties of the laminate needed to be optimized to prevent delamination to fully enable the mechanical behavior [11].

2.5.1 Commercial Fiber-Metal-Laminates

GLARE is manufactured by GNK Fokker for the Airbus Group and available as a sheet with a low curvature. Windows can be be milled out after manufacturing, however the general appearance remains a slightly curved sheet.
Within the name GLARE there are different laminates featuring different fiber orientations and aluminum alloys to achieve desired mechanical properties. Different GLARE laminates for different loads are available and can be chosen according to the application. Optimized laminates for longitudinal, impact or shear loads are available through fiber orientation optimization, aluminum alloy selection and variation of the GFRP to aluminum ratio [16]. The laminate has a balanced CTE-mismatch so the aircraft can start and travel without stress in the interface and without danger of delamination.
The quasi-static properties of FML are dependent on the fiber orientation, layup and the aluminum alloy. The range for ultimate tensile strength is 331 MPa to 681 MPa in transverse direction [20]. In longitudinal direction 455 MPa to 1282 MPa can be reached [20]. High transverse properties correlate with the low longitudinal values [20, 32].

The extraordinary crack propagation properties of FML are the reason GLARE is used frequently in aircrafts. The dynamic loads in aviation after crack initiation are dominating the requirement profile for materials. The crack propagation properties of the laminates increased with increasing number of interfaces due to the crack stopping effect [16]. The FML has a fiber-bridging effect in the FRP component and the interface of the FML induces a crack stopping effect, which enhances the dynamic properties [33, 34]. A laminate consisting of aluminum and polymer layers without reinforcements showed higher crack propagation properties compared to monolithic aluminum. Especially cracks, which were only partly through the thickness resulted in a higher fatigue life of the laminate compared to the bulk material [35]. The impact and fatigue after impact of FML is also very good compared to bulk materials. The cycles to failure were increased from 25.000 cycles with aluminum to 97,200 to 127.000 cycles by GLARE 3. The failure of the aluminum was sudden, while the crack in GLARE propagated, increasing the safety properties [36].
Aircraft fuselages need to meet secondary requirements like burn through resistance. A burn through test with a flame temperature of 1100 °C showed that the aluminum and epoxy did not stop the fire, but the glass fibers retained the fire to the outside of the laminate [33].

2.5.2 Experimental Fiber-Metal-Laminates

The objective of many experimental FML was to surpass the mechanical properties of GLARE using different fibers or metal sheets. CARALL led to an increase in strength to 420 MPa compared to GLARE with 380 MPa, while also increasing the stiffness by approximately 4 GPa [37]. However, the interfacial properties often caused premature failure, which lead to lower laminate properties.
The mechanical potential of GLARE can be increased with other constituents featuring better mechanical properties.

ARALL can reach up to 70 GPa in stiffness, which is higher than GLARE, which has a maximum stiffness at 67 GPa, but only because of a 80 % volume fraction of aluminum. The higher stiffness of the aramid fiber resulted in higher laminate stiffness [14].
These other material pairings can increase the risk of delamination and have to be researched more to be applicable in components [37]. Research on aramid fiber reinforced aluminum laminates (ARALL) showed problems with fiber matrix adhesion as well as adhesion between AFRP and the aluminum layer. Additionally were the impact properties of ARALL not as good as the properties of GLARE, as the residual strength was lower [21].
Carbon fiber reinforced aluminum laminates (CARALL) showed problems concerning CTE-mismatch and corrosion. After hygrothermal aging at 80 °C and 98 % humidity the strength and stiffness were reduced by 4 %. The compression properties were reduced by the identical factor [38].
Polypropylene was also used to possibly enhance the performance of GLARE. A maleic-anhydride modified copolymer was used to increase adhesive properties to aluminum. Although the adhesive properties were acceptable, the mechanical properties of GLARE was superior [39].
The combination of PEEK with titanium, which could surpass the properties of GLARE, needed an adhesion enhancing process to prevent delamination. Sand blasting could significantly increase adhesion, which was thermally stable up to 120 °C and led to higher quasi-static properties than GLARE [23].

2.5.3 Fiber-Metal-Laminates with elastomer interlayers

Fiber-Metal-Laminates with elastomer interlayers (FMEL) intend to increase the mechanical performance of conventional FML. CARALL has the highest lightweight potential and shows problems with corrosion due to electrochemical potential [12] and with delamination due to the CTE-mismatch of the CFRP and aluminum [13].

A common solution to overcome these problems is the integration of an interlayer or a surface treatment of the metal layer. Wang et al. used a sol-gel coating to electrically decouple the constituents, which prevented corrosion [12]. Lin et al. showed the different strains in the laminate after cooling from curing temperature [13], which could cause delamination.
The FMEL uses elastomer interlayers to adhesively bond the CFRP with the aluminum layer and enable the full lightweight potential of the constituents through good interfacial properties. Sarlin showed that the elastomer could increase adhesion in a steel GFRP laminate to prevent delamination under different load scenarios [40]. The elastomer interlayer was manufactured between every FRP and metal layer to inhibit delamination and prevent corrosion [40]. The additional benefit of the interlayer was enhanced vibration properties as well as inhibited corrosion.
The galvanic corrosion can be prevented by electrically decoupling the constituents through a high electrical resistance, which is given by the elastomer layer. The laminates were exposed to thermal loads for the evaluation of the CTE-mismatch, moisture to determine the corrosion resistance and the superimposed moisture and temperature load. The adhesive strength of the interlayer with the constituents exceeded the cohesive elastomer strength even after exposure to any load, which proved the interface stronger than the elastomer layer [41].
The vibration damping due to the elastomer interlayer was analyzed using loss factor experiments. The elastomer interlayer increased the damping of the laminate. The increase in properties can be estimated using a mass weighted rule of mixture [42].
The elastomer interlayer increases the weight of the laminate and reduces the mechanical properties and whether the FMEL can surpass the properties of GLARE has to be analyzed.

2.6 Materials selection

A materials selection can be conducted according to Ashby et al. [43], where the objectives in load bearing capacity, constraints concerning different attributes and a database of all materials are used to find the best suited material. The predicted load and lightweight objective can be used to find the optimum laminate. Restrictions like geometry or manufacturing process can be applied as well to obtain the correct design through the selection.
For FML the materials selection is more complicated, since combination has to be valid for the laminate. The constituent materials should have high stiffness and strength values combined with low densities and good interfacial properties. The laminate optimization is supposed to show the lightweight potential through selection of the layer thickness and succession in the laminate.
Van Campen showed that the fiber orientation could be arranged to fit the load and stiffness [44]. A variable stiffness laminate was achieved which was optimized concerning the mechanical properties to fit an application. The layups can be optimized against fatigue crack initiation, fatigue crack propagation and residual strength for a lower wing skin, which found an optimum for 0.4 mm thick aluminum layers in the laminate [45].

2.7 Microstructure and interfacial characterization

The visualization of components and interfaces is crucial for the understanding of the laminate and to show flaws in the laminate due to the manufacturing process [17].
Figure 2.8 presents a cross-section polish of an FML with biaxially oriented GFRP layers and aluminum sheets. The interface does not exhibit flaws, where lower mechanical properties should be expected due to low interfacial properties.

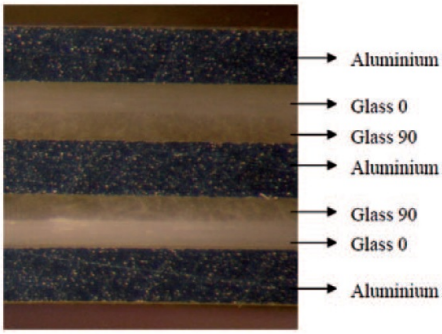

Figure 2.8: A cross-section polish of an FML with biaxial GFRP layers and aluminum presenting good interfaces [18]

2.7.1 Microstructure

The knowledge of the laminate microstructure is essential for precise statements concerning the behavior. The manufacturing process can also be supervised by analyzing the microstructure. Different techniques are used to visualize damage to the laminate in-situ, ex-situ or post mortem.

X-ray imaging

X-ray imaging can be used to find damage or pores in FRP laminates without damaging the laminate. The non-destructive testing can be conducted before mechanical testing to define the manufacturing quality and to find damage post mortem [46]. Damage like matrix cracks, fiber failure and delamination can be found in FRP after failure [47]. The evaluation of specimens throughout experiments allows deeper insights into the material behavior. The damage evolution in FRP can be defined and the appearance of different failure mechanisms depending on load can be derived [48]. The stiffness degradation in fatigue experiments can be linked to the damage evolution caused by the fatigue loading. The x-ray imaging is used to gather additional information to better describe mechanical behavior.

In the x-ray images on biaxial GFRP specimens the differentiation between primary cracks and secondary cracks could be made. Also intraply, interply and fiber fractures could be distinguished. It was shown that three dimensional images of the cracks could be deduced, while correlating the crack to a certain fracture mechanism [46]. Schilling et al. could also show voids and single fibers in μCT scans to account for the inner structure of the FRP [47].

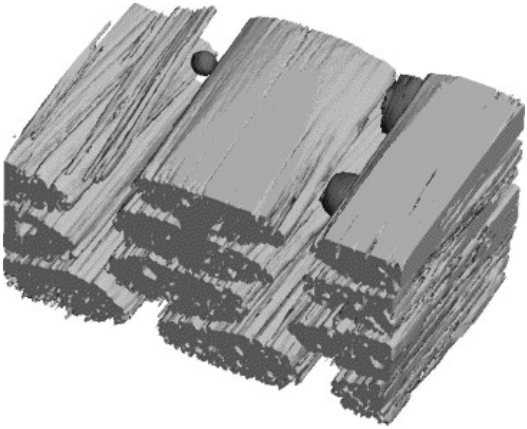

Figure 2.9: Three dimensional X-ray image of a GFRP showing fibers in grey and the voids in dark grey while the matrix was faded out [47]

Figure 2.9 shows a GFRP specimen scanned an reconstructed in a three dimensional image, which presents the glass fibers in light grey and the voids in dark grey. The matrix was faded out for better visualization. The image shows the possibility to non-destructively analyze the manufacturing process to find voids in the matrix and therefore guarantee high manufacturing quality and correlate mechanical properties to detected defects.

Cracks in woven GFRP specimens during the fatigue life can be detected to link the mechanical performance to damage in the specimens [48]. During the different cycles, the damage evolution was determined to analyze the failure mechanisms and pair the damage to the fatigue cycle regimen. It was found that transverse cracking occurs early, followed by longitudinal cracks. At approximately 50 % of the lifetime, the transverse cracks open and cause fiber matrix debonding. Resin pockets were more damage tolerant, as the resin pockets only failed shortly before specimen failure.

2.7.2 Interfacial properties

The interface of the FML is the most crucial failure initiation source for premature failure. The interfacial performance is important to retrieve the maximum laminate performance. The interfacial properties can be assessed through different experiments, can be enhanced, but insufficient interfacial properties can cause premature failure of the laminate. In ARALL, the adhesion between the FRP constituent and the metal sheet led to premature failure found by Verbruggen [14]. The interface is generally defined by Lawcock et al. through the adhesive properties of the matrix and the metal layer [49]. It was shown that the interfacial properties of CARALL can be enhanced by etching and silane coating the aluminum layers. The interfacial properties were assessed by the DCB test and the surface treatment increased the properties by a factor of six.
The adhesive quality can be determined by the failure mechanism of the laminate in shear experiments. De Freitas et al. presented a new test method to asses the interfacial properties using a peel test, which is the most critical for adhesives [50]. The interfacial values obtained with the measurement, however, can only be compared when the exact same adhesives for preparation were used.

Truong et al. used DCB tests to assess the interfacial properties of CARALL. The obtained energy release rates between 800 J/m and 1500 J/m can only be compared to other laminates, when the experiment is conducted identically. An additional criterion is an interfacial crack which does not enter either constituent [51].
The interfacial properties can be enhanced, as Lucchetta et al. showed an increase in surface roughness from 2 μm to 6 μm resulted in 33 % enhanced shear strength. Additionally to higher strength it was observed that at high surface roughness the polymer showed party cohesive fractures [27].
An elastomer interlayer was also found to increase adhesion, as steel-GFRP laminates with elastomer interlayers as the interface remained inteact in peel tests, because the cohesive strength of the elastomer was surpassed. The ductile interlayers could alter the mechanical behavior and change the brittle to ductile behavior [52].
However, the interface can cause premature delamination in compression experiments as visualized in figure 2.10.

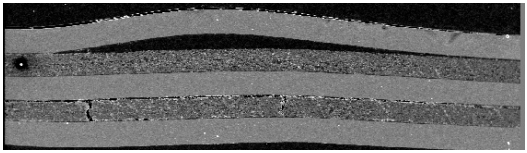

Figure 2.10: GLARE in compression with insufficient interfacial properties showing delamination buckling [18]

Figure 2.10 presents a GLARE specimen, which showed delamination due to compression combined with buckling of the aluminum layer. The interfacial properties were found insufficient to transfer the loads between the constituents, as delamination occurred prior to compressive failure. There are also cracks visible through the thickness of the GFRP constituent and along the interface.

Interlayers

An elastomer interlayer can be introduced to the laminate to increase adhesion. The elastomer interlayer has a low density and high thickness, therefore, the specific properties of a laminate with the interlayer would be reduced. However, the properties of the elastomer interlayer promise to solve the problems arising with the combination of carbon fibers and aluminum. The layer was used in a precured state, which resulted in simultaneous curing of the CFRP and elastomer [40].
It was found that the adhesion of the elastomer was enhanced further by sand blasting of the steel sheet. The surface roughness increased from 0.38 μm to 2.46 μm, which increased the peel force from 0.9 N/mm to26.88 N/mm. This enhancement of interfacial properties caused a change in fracture location from the interface into the elastomer [52].

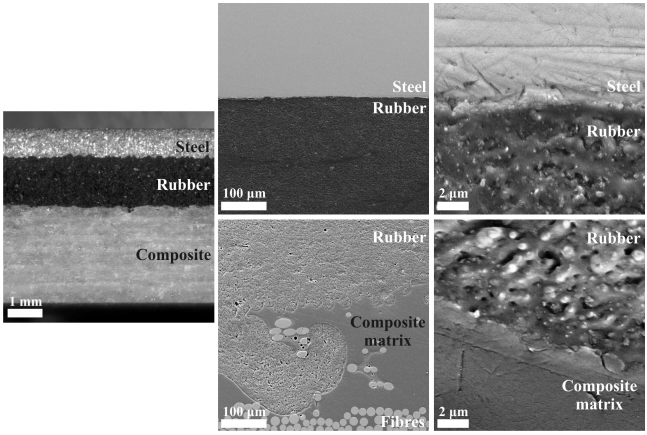

Figure 2.11: Cross-section SEM images presenting the elastomer metal and elastomer FRP interface [40]

The elastomer interlayer presented in figure 2.12 was placed between every metal and CFRP layer to enhance adhesion, inhibit corrosion and balance the CTE-mismatch. The interfacial properties of the laminate after hot,

moist or hot and moist environments remained constant, as the interlayer could balance the CTE-mismatch and prevent corrosive damage. The failure was cohesive failure in the elastomer constituent [41].
Additionally the elastomer layer increases the energy absorption and decreases damage to the structure under impact loading. Although the absorbed energy remained constant compared with structures lacking the interlayer, the damaged area was reduced by 50 % due to the elastomer [53].

2.8 Mechanical characterization

The mechanical properties of FML are assessed by quasi-static and dynamic experiments. Additionally to different load scenarios, environmental loads can damage the laminates and have to be analyzed before application. The superposition of environmental and fatigue loading, thermal mechanical fatigue, can be of interest when analyzing FML. The failure mechanisms of the laminate and the constituent responsible for the damage is analyzed to describe the behavior of the laminate.

2.8.1 Quasi-static characterization

The mechanical properties of FML can be calculated using the rule of mixture for the stiffness and the classical laminate theory (CLT) for the strength [54]. The stiffness of the CFRP layers could be approximated using the Voigt and Reuß theorem. For longitudinal layers the composite stiffness E_c was calculated using the fiber volume fraction v_f and the fiber stiffness E_f along with the matrix volume fraction v_m and matrix stiffness E_m.

$$E_{Voigt} = v_f * E_f + v_m * E_m \tag{2.1}$$

The stiffness is linearly superimposed and the assumption is valid for iso-strain states in fiber direction of an uni-directionally reinforced composite.

For iso-stress states and transverse layers the Reuß equation is used to calculate the stiffness.

$$E_{Reu} = \left(\frac{v_f}{E_f} + \frac{v_m}{E_m} \right)^{-1} \tag{2.2}$$

The CFRP layer can be calculated by using the Voigt equation for longitudinal and Reuß for transverse layers. The stiffness of the laminate can be calculated under an iso-strain assumption using the Voigt equation.
The strength of the laminate can be approximated using the CLT in the software *eLamX*^{2} by the University of Dresden. The CLT approximates the strength of the laminate with linear elastic behavior and planar stress states under perfect interfaces. The calculations using classical laminate theroy fit well with experimental results in tension tests performed by Vlot et al. [2].
Tensile tests showed uniform strain distributions over the cross section. The tests presented first failure in the fibers of the FRP constituent, because of the lower strain to failure [55]. The fiber orientation had a strong effect on the mechanical properties, as the load bearing capability could be increased by orienting the fibers in load direction [56].
With high fiber orientation, stiffness differences between the constituents can occur, which load the interface. Premature delamination can occur and reduce the stength of FML. Also can the specimen size induce edge effects, where delamination is aided. The edge delamination led to severly reduced strength of the laminate [57].
The compressive properties of FRP are lower than the tensile properties; therefore, the compressive properties of the laminate are lower than the tensile properties caused by microbuckling of the fibers. Schultheisz et al. showed microbuckling in different load scenarios in FML, where compression buckling is the most critical [58]. The compressive strength of the laminate can be reduced significantly by microbuckling, if delamination can also occur. Remmers et al. stated that delamination buckling occurs in compression, where delamination of the constituents with subsequent buckling of the delaminated sheet leads to reduced mechanical properties [59].

The delamination buckling is visualized in figure2.10, where the interfacial properties and the compressive properties of the FRP caused premature failure.

Flexural experiments, which combine shear stress in the core with compression and tension loads in the outer fibers, showed failure initiated from the compression side of the specimen [2]. If the failure mode in flexural experiments is compression failure in the outer fiber, it shows sufficient interfacial shear properties of the laminate, because the interfacial properties did not cause failure.
The flexural properties of GLARE can be optimized using steel sheets instead of aluminum. Steel was introduced in GLARE laminates and increased the flexural properties of the laminate. However, specific properties were not analyzed, therefore the effect of the high density and flexural properties of the steel cannot be evaluated [24].
Big stiffness differences between the constituents of the laminate can result in non uniform deformation and a more complex behavior. The constituents with lower stiffness deform due to shear loads, which causes the constituent layers with high stiffness to bend only relative to their own neutral fiber. Subsequently the increase in bending resistance due to the increase in axial moment of inertia is lost and results in lower bending stiffness of the laminate [60].

The interfacial properties can lead to premature failure of the laminate. Therefore, the properties are characterized by loading the interface in shear loading. The standard test method is the lap shear test, but bending effects and strain due to tension load of the constituents can impact the results. Therefore, the shear strength is often used when comparing interfacial propertis and the shear stiffness or shear deformation are neglected [61].
Biaxially oriented FRP showed shear failure in the lap shear test in transverse plies, due to the lower stiffness than the longitudinal plies.

The crack propagated close the the interface between the differently oriented FRP layers [62].
However, the interfacial properties are rarely assessed without loading the constituents and falsifying the result. The lap shear specimen has a length of 250 mm and two notches have to milled into the specimen with high accuracy to enable the shear load. Additional problems are bending effects in the specimen and high inaccuracies in strain measurement.
An alternative experimental method to the lap shear test is the peel test, which uses a different loading direction, which is rarely applicable for laminates, but can measure the interfacial properties better than the lap shear test [63].
A different alternative testing method is the edge shear test, which optimized the experimental setup to reduce specimen preparation and gain more accurate interfacial properties due to direct strain measurement at the specimen. The specimen length was reduced to 10 mm and bulk laminates could be tested. Only slight tilts could not be prevented in the experimental setup [64].

Additionally to mechanical loads there are environmental loads, which damage the laminate and reduce the properties. The polymer properties can be reduced due to increased temperature. Hagenbeek et al. showed the properties of laminates unter higher temperature are reduced, because the temperature dependent properties of the polymer result in lower properties [65]. In extreme situations the polymer can degrade to high temperatures. A temperature of 188 °C can start the decomposition of the epoxy. Although the full decomposition might not be reached below 500 °C, the start of decomposition could cause adhesive proplems and failure in the laminate [66].
The different coefficients of thermal expansion of the constituents of FMEL can cause thermally induced stress in the laminate's interface. The repair of GLARE can damage the laminate due to the thermal curing of the repair patches.

It was found that the curing temperature of 90 °C, which was applied to the repair patches, affected the surrounding GLARE structures. At 105 °C the surrounding structure showed buckling [67]. However, the thermal strains can be reduced using a thermal expansion clamp. The thermal strains were reduced by 39 %, which can significantly enhance the laminate [68].
The damage to a laminate by a single temperature spike was shown, but recurring thermal loads can be found in application, which can repeatedly challenge the material as defined by Beumler for GLARE [16]. To assess the properties of the laminate under recurring thermal loads peltier elements can be used to generate the temperatures. A thermal cycle from 0 °C to 60 °C was conducted in 62 s, showing the potential of peltier elements for thermal loading [69]. The thermal cycling reduces mechanical properties in CARALL, where a reduction of 4 % due to 6 weeks hygrothermal aging at 80 °C and 90 % relative humidity was found. The stiffness and strength were reduced identically [38]. The properties of GLARE remained constant throughout the same hygrothermal aging [70], showing the different properties of the laminates. Single GFRP layers showed reduced properties, but the aluminum layers in GLARE protected the GFRP from the environmental loads [70]. Subsequently it was found by da Costa, that laminates consisting of GFRP and aluminum adhesively bonded by a tape showed constant mechanical properties after 2000 thermal cycles from −50 °C to 80 °C [71].

Additionally to thermal loads, corrosive environments can damage the laminates. The constituents of FML can be prone to corrosion, which can be addressed at the materials selection. However, the combination of two materials can also cause galvanic corrosion in the interface between said materials. The combination of glass fibers and aluminum is not critical [5], while is the combination of carbon fibers with aluminum can cause corrosion, as the electrical potential between the constituents defines the danger of corrosion [72]. It was found that hygrothermal aging reduced the mechanical properties of CARALL due to corrosive damage [38]. .

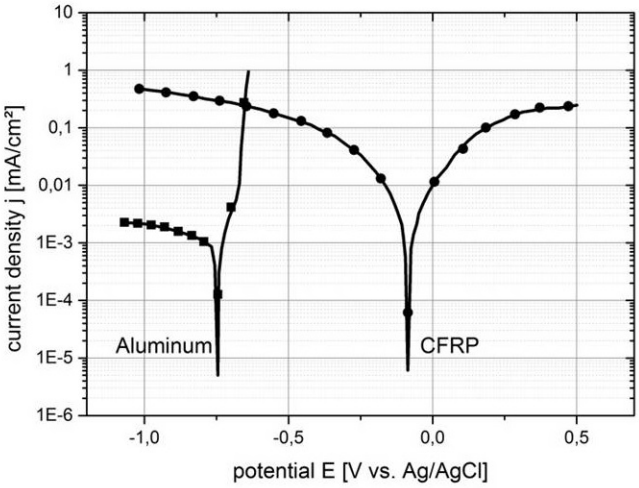

Figure 2.12: Electrical current density versus electrical potential curve of aluminum and CFRP against an Ag/AgCl electrode to visualize the corrosive potential of the combination [72]

Figure 2.12 shows the difference in electrical potential for aluminum and CFRP. Both materials are corrosion resistant, but the combination has an electrical potential of approximately 0.65 V [72]. Galvanic corrosion can occur, when a threshold of 0.1 V is exceeded and it will cause the less noble material to corrode [72].

The residual properties after corrosion proved GLARE as corrosion resistant [70], while CARALL was prone to galvanic corrosion [38]. Also interlayers can inhibit corrosion in laminates as presented by Wang et al. [12], who used a sol-gel coating to inhibit corrosion in a galvanic cell. Additionally, an elastomer interlayer between steel and GFRP subject to 85 °C and 85 % relative humidity retained the mechanical properties of the laminate [41].

2.8.2 Dynamic characterization

Puncture

The puncture properties represent the resistance of a material against an object penetrating the structure and are closely related to the impact properties. Puncture experiments penetrate the laminate, while impact experiments only damage the laminate without penetration.
The puncture properties of FML can surpass bulk materials due to the increased number of interfaces, while GLARE exhibited better propreties than ARALL [31]. The first generation of FML, ARALL, and the second generation, GLARE, were impacted with a 2080 g impactor and a speed of 10 m/s. High velocity impact tests were conducted using 24 g steel tips at a speed of 100 m/s. GLARE showed a 15 % higher low velocity minimum cracking energy than aluminum. The difference at high velocity reulted in an increase in resistance by the factor of 2 to 3.5. ARALL, however, showed lower energies at first failure for both velocities compared to bulk aluminum [30]. The failure initiation location of ARALL and GLARE was on the non impacted, the convex side. The residual fatigue properties of GLARE were higher than the properties of ARALL and bulk aluminum [31].
Aluminum 2024-T3 showed benefits because of ductility and stiffness, which could not be met by other aluminum alloys or different materials like magnesium or titanium. GLARE exhibited better properties than ARALL and CARALL due to the beneficial strain rate dependent properties of the fiber [73].
The absorbed energy measured in the experiments could be correlated by Caprino et al. with the damage, independent of the impactor velocity and mass. The mass was varied between 3.5 kg and 10.2 kg, achieving full penetration at the lowest energy level. The velocity was increased by 70 % and could not show the strain rate dependent behavior of the glass fiber [74].
The puncture properties of GLARE can be enhanced by increasing the GFRP percentage of the laminate.

The beneficial strain rate dependent behavior and an increase in GFRP consituent increased the puncture properties of the laminate. A high GFRP content was achieved by using thin aluminum sheets with thick GFRP layers. The minmum cracking energy was increased and the damaged zone decreased compared to the standard GLARE configuration [30].

Impact

Impact tests load the laminate with a certain energy to deliberately damage the laminate and examine the residual properties to account for the damage tolerance of the laminate. The primary result of this experiment is the damage of the impact at a certain energy level and the amount of elastically and plastically absorbed energy. After the impact the residual strength can measured either in tension, fatigue or compression experiments. The resudial tensile strength of ARALL was nearly constant for initial stresses below 200 MPa, which was below the yield stress. An increase in initial stress to 300 MPa resulted in a drastic decrease of 30 % or in complete failure [30]. At the same impact levels the damage to GLARE was significantly lower than the damage to ARALL. At an impact energy of 20 J full perforation was achieved in ARALL, while the damage in GLARE was barely visible [75]. Tension tests on GLARE showed that starting with an impact of 16.4 J a significant damage could be induced, which increased using 23.7 J, but did not increase further until perforation at 34.5 J. The perforated laminate had the same residual properties as the laminate impacted with 23.7 J.
De Freitas et al. found a linear relation between delaminated area and absorbed energy prior to compression after impact tests. Buckling occurred in the delaminated area, which defined the compression after impact properties. An increase of the impact energy from 4 to 13.2 J reduced the compressive strength from 110 kN to 69 kN [76].
Bagnoli et al. showed that the fatigue after impact properties decreased with increasing impact load.

The crack propagation rates of a specimen impacted with 30 J was higher than 10 J and higher than the unimpacted laminate [77]. However, Wu et al. found stable crack growth in fatigue after impact tests for the GLARE specimens, while the aluminum failed sudden and catastrophic [78].
In addition to Wu et al., the fatigue after impact analyzed by Laliberte et al. showed that after an impact event, GLARE did not present crack growth from the impact location, but from the shoulders of the specimen. Only in aluminum there was crack growth from the impact location. Also did the FML change the sudden aluminum crack to a damage tolerant failure [36].
The impact properties of GLARE could be simulated within an error of 5 % to predict the damage tolerance of the laminate [79]. The model used quasi-static properties of the constituents and for the GFRP a stain rate dependency was added. Although the error is small, the shape of the simulated curves matches the experimentally obtained curves insufficiently.
The impact damage and response can be predicted using the energy balance model [80]. The model states, that the difference of kinetic energy of the impactor is transferred to the laminate. This energy is equal to the sum of of the strain energies due to contact, membrane deformation, bending and transverse shear.
Changes in constituents from GLARE generally led to lower impact properties. Magnesium sheets, as well as a thermoplastix matrix, resulted in a reduced impact resistance. FML with magnesium showed comparable specific results to aluminum FML over a range of impact energies from 10 J to 10 J, although the specific first crack energy was lower [81]. An elastomer interlayer, however, could significantly enhance the energy absorption due to the increased damping. The area of damage was decreased by 50 % due to the integration of the elastomer interlayer [53].
The effect of impact damage in CFRP is more extensive in the high cycle fatigue region compared to lower cycles to failure. The low cycle fatigue showed comparable results, while a lifetime reduction of approximately 15 % was found in the high cycle fatigue area after an impact with 1.7 J [82].

Impact tests on CARALL showed no critical damage at 2.35 J, but fiber and matrix fractures and aluminum shear cracks at 9.40 J. The absorbed energy increased with increasing impactor energy as the energy dissipation mechanisms were mainly crack growth.
Contrary to the high mass, low velocity impact generally analyzed, small mass impact test can be used to simulate a small object hitting the laminate, which can be closer to the application in the automotive industry. A steel sphere with 250 g was accelerated onto the specimen surface with a defined energy, while the impactor velocity before and after impact was determined using a high speed camera and digital image correlation. The impact load could be calculated from the high speed images and correlated well with analytical models [83].

Compression after impact

Compression After Impact tests (CAI) are an instrument to measure the residual properties of a damaged structure. Compression is generally to most critical load scenario for a damaged laminate.
The type of FRP also influences the CAI performance, as NCF fabric has low CAI properties and woven sheets have high properties, because comparatively the woven fabrics had better impact performance with lower damage areas [84]. The CAI properties of woven CFRP are reduced with increasing impact energy, because the tendency to microbuckling was increased. The residual compressive strength was reduced by 50 % at an impact energy of 3 J [85]. Laminates can be engineered to have high trough-thickness properties and therefore better CAI performance. CFRP specimens with z-fiber pinning had up to 63.6 % smaller damage areas compared to CFRP specimens without the fiber pinning. The CAI performance of the pinned CFRP resulted in a 50 % increase compared to regular CFRP [86].

DCB

The double cantilever beam test is generally used to determine interfacial crack propagation rates in Mode I. Interfacial cracks can propagate significantly faster than through cracks depending on the adhesive properties.
In the research presented by Busch et al., the precrack between the metal and GFRP layer propagated further in the interface showing lower interfacial properties compared to the interlaminar properties of the GFRP. The peel load applied by the DCB experiment is critical for adhesive properties and can be used to describe the quality of the bond [87].
The interfacial properties between metal and FRP layers can be lower than the properties of the constituents and therefore allow higher crack propagation rates. To obtain a lower crack propagation rate, the interfacial properties need to be increased.

Charpy

Charpy experiments indicate the material response to dynamic crash loading. Laminates generally show a high energy absorption due to the numerous interfaces and high ductility of the metal layer [88]. CFRP has low charpy properties due to the low strain to failure of the fiber an the matrix. The charpy properties can be enhanced by the integration of more ductile materials, like a metal layer.
A metallic rear panel increased the charpy energy by approximately 30 % compared to pure CFRP due to the high ductility of the metal layer. The maximum force was lower with metal layer, but a high displacement increased the energy. A ductile face layer would increase the performance of the CFRP the most [89].

Fatigue

The dynamic loads on a structural component can be sudden, which is experimentally determined by charpy, puncture and impact tests. Also recurring loads, which are represented by fatigue experiments, appear during the lifetime of a structural component. Vibrations from engines, turbulences or inhomogeneous loads occur during the application and are resembled by fatigue experiments, where the fatigue endurance limit is a crucial mechanical property for mechanical design [16].
However, for FML solid specimens are often neglected in favor or notched specimens, as cracks are assumed to be in every aircraft fuselage, due to drilled holes or other geometrical restrictions [2]. Laminates generally have better fatigue crack properties than bulk aluminum because the interfaces act as a crack stopper and the effect can already occur in adhesively bonded aluminum without a FRP component. In partly cracked specimens, the lifetime of aluminum can be increased by the factor of ten with laminated aluminum sheets [35]. The crack initiation in GLARE occurs earlier than in aluminum, but the cycles to failure are tripled in GLARE compared to the bulk aluminum [34]. The crack propagation threshold in GLARE is defined by the aluminum layers and therefore the start of crack propagation solely depends on the metal [90]. Crack propagation in GLARE is accompanied with delamination growth. The energy dissipated increases the fatigue properties and the energy release rate can describe the interfacial properties of the laminate. The fiber orientation adjacent to the delamination is crucial for the energy release rate [91].
However, the experimental procedure can influence the properties due to the strain rate dependent properties of the glass fibers. The strength of aluminum decreases by 6 % when the strain rate is increased from quasi-static experiments to 100 $1/s$. The strength of GLARE increases by 16 % caused by the same strain rate variation [92].

Additionally, environmental impact has to be prevented, as the properties of GLARE can be reduced by moisture through reduction of the glass transition temperature of the polymer is reduced from 100 °C to 80 °C [93]. Additionally were slower crack propagation rates found at −40 °C compared to ambient temperature, which were caused by a smaller delaminated area around the crack [90].

Fatigue experiments on CARALL were conducted while monitoring of the crack growth using fiber bragg analysis. The strain assessed by fiber bragg analysis was backed by CT-scans, where good accordance was found [94]. The propagation rate could be predicted, if the crack length was known. The crack propagation properties of the constituents were used to simulate the fatigue crack properties of the laminate. For load levels of 80, 100 and 120 MPa the prediction fit the experiments well. Also was the result accurate for different numbers of layers. [95].

The fatigue crack propagation is important for aviation, where existing notches and cracks are assumed. However, in other industries like the automotive industries adhesively bonding is prioritised over riveting when FRP is used. Therefore, the fatigue properties of FML need to be evaluated without notch or crack to obtain fatigue characteristics. Solid specimen fatigue of FML is not widely conducted, however, the fatigue properties of the constituents are universally known.

The fatigue behavior of metals is well researched and the crack initiation, propagation and lifetime based on the stress or strain level are estabilised [96, 97]. The lifetime of metals can be predicted based on elastic strain or on plastic strain. In low cycle fatigue the plastic strain defines the lifetime of the material and a plastic strain based prediction can be conducted [98].

The high cycle fatigue failure depends on the elastic strain and the lifetime can be predicted using the elastic strain [99]. The stress level in the specimen defines which lifetime prediction is applicable. Fatigue experiments on solid FRP specimens are common using ISO 13003 [100].

The failure criterion in the standard is a stiffness decrease of 20 %, which can be caused by various effects in the FRP. The stiffness can be reduced by matrix cracks, fiber failure and delamination. It was found that delamination of constituents can reduce the stiffness of the laminate, because the shear load transfer through the interface is prevented [101]. Additionally it was shown that delamination starting from the edges of the specimens can cause delamination, which occurs earlier than failure in the specimen volume. Also cracking of the off-axis FRP layers was observed [102]. Garcea et al. found matrix cracks during fatigue loading in the longitudinal and transverse FRP plies combined with delamination using synchrotron radiation computed tomography and in situ loading to open the cracks which occurred in prior fatigue loading. The matrix cracking can also reduce the stiffness of the material [103]. Berthelot et al. measured the crack density in the transverse plies of bidirectional GFRP and CFRP and the resulting stiffness decrease. The cracks started from the edges and propagated instantaneously through the full specimen width [104]. The lifetime prediction stated by Ogin et al. [105] was used in good accordance with the experimental values for GFRP and CFRP.

The fatigue performance of FRP is generally examined against a stiffness decrease failure criterion and further described by the failure mechanisms. The size of the structure can change the fatigue performance, because free edges enable cracking of the specimens. An increase of the specimen size resulted in lower scattering as the crack initiation in GFRP was more reliable [106]. The laminate thickness can reduce the load bearing capability of the laminate. Laminates with thicknesses between 2 mm and 50 mm showed that with increasing thickness exothermal manufacturing processes can influence the mechanical properties. Also the temperature increase due to fatigue loading was increased linearly with the thickness. This effect reduced the mechanical properties in fatigue loading [107] and for comparable results the specimen size should be chosen according to the standard.

Fatigue experiments with specimens containing elastomer interlayers can suffer from high temperatures in the laminate due to the damping of the elastomer. The effect of the elasomer was investigated using 5 mm steel face sheets and a 15 mm elastomer core in cyclic compression and bending experiments. Large strains and high frequencies caused the highest temperature of 95 °C at 6 Hz and 18 % compressive strain [10].

Thermal mechanical fatigue

Thermal mechanical fatigue (TMF) experiments are used to determine the performance of the laminate under superimposed thermal and mechanical loads. TMF represents the laminate during application with a combination of mechanical load and environmental load. The recurring superimposed loads can show the behavior of the material under near application loads and indicate the applicability [108].
The mechanical properties of the polymer components vary with the thermal load. Lower mechanical properties at high temperatures and higher properties at low temperatures result in stress redistribution into the metal layer of the FML. The static tests at elevated temperature showed lower GLARE properties at 80 °C compared to ambient temperature. The reduction in tension and compression varied from 3 % to 10 % depending on the layup [65]. The interface can be loaded with stress due to the CTE-mismatch and the stiffness difference of the constituents, which changes dynamically throughout the experiment. Premature failure can occur due to low interfacial properties, while failure in the constituents indicates sufficient interfacial strength. TMF of FRP with viscoelastic materials results in heat generation at high frequencies. Experiments on GFRP with a thermoplastic matrix showed thermal fractures due to internal heat generation. The heat generation increased with higher strain rates, shown by higher loads at the same frequency as well as higher testing frequencies. The resulting S-N curve for 10 Hz showed lower lifetimes than the curve for 2 Hz [109].

Fatigue experiments at elevated temperature of monolithic and notched CFRP specimens between ambient temperature and 150 °C show a decrease in lifetime with increasing temperature. The decrease of mechanical properties was most significant close to the glass transition temperature of the PEEK matrix. Crack propagation is enhanced at elevated temperatures, which resulted in a higher sensitivity to temperature of the notched specimens compared to monolithic specimens [110].
The TMF behavior of aluminum is evaluated at far higher temperatures than the TMF of FRP specimens. The maximum temperature in FRP tests varies from 80 °C to 150 °C and shows significant results, while the high temperatures for aluminum are approximately 300 °C, while the low temperature is 150 °C. The properties of aluminum are reduced with high temperatures, caused by grain coarsening and crack propagation [111].

2.9 Lifetime prediction

Lifetime predictions generally calculate the cycles to failure for different materials [112]. Since the laminate consists of different constituents, a simple conventional prediction for the whole laminate cannot be conducted. For simulation of dynamic properties of FML, the quasi-static properties of constituents were used with the assumption of a perfect interface [79]. Lifetime predictions for every constituent can be conducted and combined with the assumption of a perfect interface to obtain a combined lifetime prediction accordingly.

2.9.1 Laminate

Rarely lifetime predictions for whole laminates exist [113] and the transferability is not given due to different constituents, failure criteria and loading. Chang et al. based the model for pre-cracked GFRP and aluminum on the classical laminate theory which also accounts for the stress history.

An iso-strain state is assumed in the specimen, which results in different stress levels in the constituents. The aluminum layer has a higher stiffness than the GFRP, resulting in a shorter fatigue life of the metal and the prediction overestimated the lifetime. The prediction was based on crack propagation of notched specimens and is therefore not applicable for monolithic specimens [113]. The approach of assessing the lifetime of a laminate by combining the predictions of the constituents with an iso-strain assumption could be used to generate a lifetime prediction for an FML based on well fitting constituent predictions.
The load bearing capability therefore needs to be recalculated for stiffness decreases in FRP and fractures in the metal layers, to account for damage throughout the experiment in order not to overestimate the lifetime of the FML. The stiffness decrease of the CFRP can be calculated for an arbitrary load level, which results in an increase of strain during the experiment. The recalculated strain increases the stress in the other constituents. The same procedure is used for the aluminum layer, which is assumed to not carry loads after fracture. Thus, the CFRP carries the entire load after aluminum fracture. The lifetime of the elastomer does not need a prediction, as the elastomer does not fracture during fatigue experiments. The fatigue bending experiments of [10] showed no fracture in the elastomer and neither in the interfaces, which would indicate the need for a lifetime prediction.

2.9.2 Prediction for aluminum

Lifetime predictions for aluminum can be separated concerning the fatigue endurance limit or low cycle fatigue. The low cycle fatigue is often approximated by the Coffin-Manson relation [98]. For the high cycle fatigue the Basquin relation is frequently used [99]. The prediction, which should be applied, can be approximated by the stress, which is anticipated in the aluminum constituent during fatigue loading.

$$\varepsilon_{a,pl} = \varepsilon_f (N_B)^c$$

The equation connects the plastic strain amplitude $\varepsilon_{a,pl}$ with the fatigue ductility coefficient ε_f, the cycles to failure N_B and the fatigue ductility exponent c. The relation is valid for fatigue experiments, where the plastic strain defines the lifetime of the material. For experiments, where the plastic strain is negligible, the Basquin relation is used as it connects the elastic strain amplitude $\varepsilon_{a,el}$ with the cycles to failure N_B using constants like the Young's modulus E, fatigue strength exponent b_s and the fatigue strength coefficient σ_f.

$$\varepsilon_{a,el} = \frac{\sigma_f}{E} (N_B)^{b_s}$$

2.9.3 Prediction for FRP

Fatigue predictions for FRP depend on the fiber type, length, orientation, matrix material and failure criterion. Hashin et al. presented a failure criterion for GFRP caused by fiber and matrix failure, where in fiber failure mode the fibers in load direction fail progressively, while in matrix failure mode the matrix cracks propagate through the transverse layer. The criterion is applicable for biaxial NCF laminates under tension-tension fatigue loading and specimens where fiber and matrix failure occur [114].
GFRP was found by Hwang et al. to have reuced stiffness due to fiber and matrix cracks. Therefore the failure criterion proposed by Hwang et al. was a stiffness reduction to account for the increase in strain during stress controlled fatigue experiments. The stiffness reduction was approximated with a power law function [115].
Jespersen et al. showed that the damage accumulation in FRP reduces stiffness of the material. Ex-situ time lapse CT-scans were used to correlate the damage in the GFRP specimens with stiffness reduction. The cracks found in the specimens were transverse cracks in the matrix [116].
The experiment itself can influence the results, such as the stress ratio of

maximum and minimum load [117]. It was shown, that tension or compression loads in CFRP with variable amplitudes could be approximated with the miner rule. If tension and compression loads are alternated, the damage cannot be superimposed, because microbuckling prior to tension loads can decrease the properties. The influence of the stress ratio on the mechanical properties can be approximated according to Gathercole et al. [118]. The compressive side of the adapted Haigh-Diagram was smaller than the tension side, because the CFRP is sensitive to fiber buckling. The experimentally obtained lifetimes cannot be transferred to a different material, as the constants for the curve were experimentally obtained and are material dependent. The prediction for a FRP specimen has to include the stress state and ratio to generate a precise prediction.

Often a fitting parameter is used to pair the experiment with a prediction. The Goodman diagram can be adapted with fitting parameters to account for the different behavior of CFRP and AFRP compared to metals [119]. Since the parameters have to be experimentally obtained for every material, the prediction cannot be applied to an arbitrary material. The predictions with empirical fitting parameters cannot be transferred, as the parameters are derived from experiment and specimen dependent circumstances.

A lifetime prediction against a stiffness reduction failure criterion of GFRP based on transverse matrix cracking was presented by Ogin et al [105]. It is assumed that the stiffness decrease per load cycle correlates linearly with the maximum stress divided by $1 - E/E_0$ on a double logarithmic scale.

$$-\frac{1}{E_0}\frac{dE}{dN} = A\left[\frac{\sigma_{max}^2}{E_0^2(1-E/E_0)}\right]^n$$

The coefficients A and n have to be experimentally obtained. The equation can plot the predicted stiffness decrease versus load cycle as well as the prediction for the S-N curve for a predefined stiffness reduction.

Berthelot et al. examined GFRP and CFRP with the method presented by Ogin et al. [105] and concluded that the mechanism is based on matrix cracking and can be applied for glass fibers as well as carbon fibers [104]. The prediction fit the experimental results well for either fiber type.

2.10 Summary of research on FML

Research conducted on FML can be divided by the constituent materials of the laminates to demonstrate the frequency of the constituent combination in the laminates. Table 2.1 presents the constituent materials of the literature and is extended by research conducted on FRP.

Table 2.1: Constituent materials of research presented in this work

Reference	FRP	Metal
[1], [2], [3], [4], [5], [6], [9], [15], [16], [17], [18], [19], [20], [24], [29], [30], [31], [33], [34], [36], [37], [39], [44], [45], [67], [69], [70], [71], [56], [59], [62], [65], [66], [120], [73], [74], [78][77], [75], [81], [79], [92], [93], [91], [90], [95], [101], [107], [113], [121], [122], [123], [124], [125]	GFRP	Aluminum
[9], [14], [21], [29], [126], [56], [75], [121], [124]	AFRP	Aluminum
[9], [12], [13], [37], [38], [49], [50], [51], [68], [94], [121], [124], [127], [128]	CFRP	Aluminum
[40], [41], [42], [52], [53], [87]	GFRP	Steel
[26]	FRP	Magnesium
[11], [23], [25]	FRP	Titianium
[8], [121]	FRP	Metal

The summary of the references shows that the research conducted on GFRP and aluminum, which was in large parts conducted on GLARE, is more extensive than any other combination.
The second group, ARALL, was the predecessor of GLARE, but could not find an application. However, the research was comparably extensive. CARALL was also researched due to the promising mechanical properties and known environmental problems, although only three laminates with interlayers were examined.
The combination of GFRP and steel used an elastomer interlayer in five laminates showing a promising interlayer for FML.
The following FML were examined for special applications, where a different metal layer was required. The research was conducted for specific combinations of FML, as GLARE was examined thoroughly compared to other combinations. The interlayers were extensively investigated with GFRP and steel laminates and in CARALL partly interlayers were applied.
The presented research shows, that fiber-metal-laminates consisting of carbon fiber reinforced polymers and aluminum with an elastomer interlayer can close a gap to increase the properties of CARALL and expand the research on interlayers.

3 Materials selection

3.1 Methods for the materials selection

The laminate and its constituents were selected to obtain a laminate with a high flexural stiffness and low density. The materials selection was carried out according to Ashby et al. [43], where flexural sheet bending was the applied load. The selection was assisted by the software CES EduPack and Hybrid Synthesizer from Granta Design Limited. Predetermined constraints for the selection were the constituent materials, which included FRP, metal and an elastomer interlayer. Additionally the structure had to be a laminate consisting of monolithic materials.

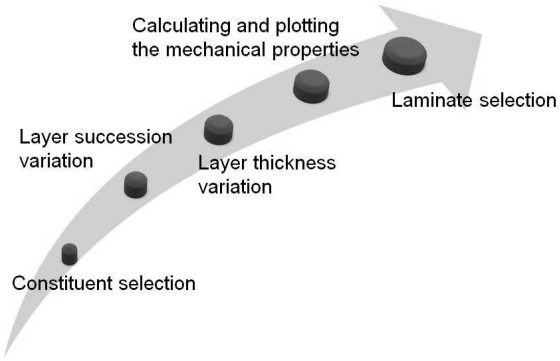

Figure 3.1: The materials selection procedure steps for the laminate

The chart in figure 3.1 shows the selection process for the laminate, which consists of multiple steps accounting for constituent selection and laminate optimization compared to conventional selections [43]. The constituents of the laminates were selected to subsequently vary the layer succession and to optimize the layer thickness in the last step. For every succession and thickness of the constituents, the mechanical properties are calculated and plotted in a stiffness-density diagram, which was used to compare the laminates. Lastly, the best laminate in the diagram was selected using the material index.

3.1.1 Constraints

The selection process was started with strict constraints. The constituent materials were partly predefined in order to obtain a FML. An elastomer interlayer had to be placed between every FRP and metal layer. Therefore, the laminate had to contain an FRP component as well as a metal layer. However, the fiber type, matrix and metal were still selectable.
Other constraints were used to define the appearance of the laminate. The total thickness was set to 2.5 mm and the layer succession was decided to be symmetric to inhibit warpage caused by different coefficients of thermal expansion. To achieve low warpage and high flexural stiffness the FRP was desired to be biaxial.
The elastomer interlayer was not expected to contribute significantly to the stiffness of the laminate. Therefore, the layer was selected with regard to good adhesive properties to the FRP and metal constituent. The benefit of the elastomer layer integration cannot be visualized in the materials selection; thus it was defined by a constraint.
The final constraint defined the need for the constituents o be manufactured in thin sheets. The laminate, a thin sheet itself, required all constituents to be commercially available in thin layers.

3.1.2 Constituents selection

The constituents were selected according to Ashby et al. [43] to define the materials of the layers of the laminate. All materials, which fit the mechanical restrictions, were used in the selection process.

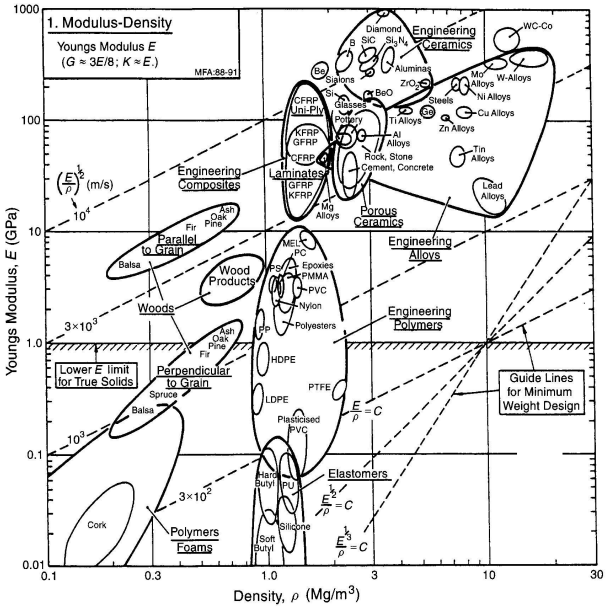

Figure 3.2: Young's Modulus vs. density diagram for a variety of materials [43]

The materials selection is generally conducted on a diagram like figure 3.2, where the desired material properties are portrayed on the axes. The diagram features predefined lines, which show the material index for light and stiff materials under tension $\left(\frac{E}{\rho} = C\right)$, bending $\left(\frac{E^{1/2}}{\rho} = C\right)$ and sheet bending $\left(\frac{E^{1/3}}{\rho} = C\right)$ loads. Based on the diagram and the material index the selection can be conducted.

A laminate has a low thickness compared to the dimensions in the other directions leading to sheet bending as the applicable load. The load on the constituent layer was sheet bending as well, which led to identical laminate and constituent material indices. The equations describing the load situations and objectives to define the material index are presented below.

$$m = \rho t l b \tag{3.1}$$

Equation 3.1 connects the mass m of the constituent with the density ρ, the thickness t, length l and width b. This equation was used to realize the objective to reduce weight. The constituent thickness was the free variable and could be eliminated.

$$S = \frac{F}{\delta} \geq \frac{CEI_y}{l^3} \quad using \quad I_y = \frac{bt^3}{12} \tag{3.2}$$

A stiffness criterion was used, meaning that the deflection of the sheet had to be lower than δ, when loaded with the load F. C is a constant depending on the loading constraints, E is the Young's Modulus of the material, I_y represents the axial moment of inertia and l the length. The axial moment of inertia I_y was stated more precisely by using the width b and thickness t. Equations 3.1 and 3.2 were combined and solved for the mass resulting in equation 3.3, presenting the connection of mass, stiffness and density.

$$m \geq \left(\frac{Sb^2}{C}\right)^{1/3} l^2 \left(\frac{\rho}{E^{1/3}}\right) \tag{3.3}$$

The latter part of the equation 3.3 containing the objectives, stiffness and density, defined the material index. The material index, $M = \frac{\rho}{E^{1/3}}$, is a straight line in figure 3.2, where it is already presented in the lower right corner. A high stiffness and low density is desired for the constituents, meaning the optimization vector is pointing in the upper left corner of the diagram.

This material index and optimization vector was applied to all materials meeting the constraints defined in section 3.1.1 to find the best laminate.

3.1.3 Laminate selection

A laminate with defined constituents can be optimized by finding the best layer succession and thickness for the maximum flexural stiffness. The possible successions and layer thicknesses were calculated using CES EduPack and Hybrid Synthesizer.

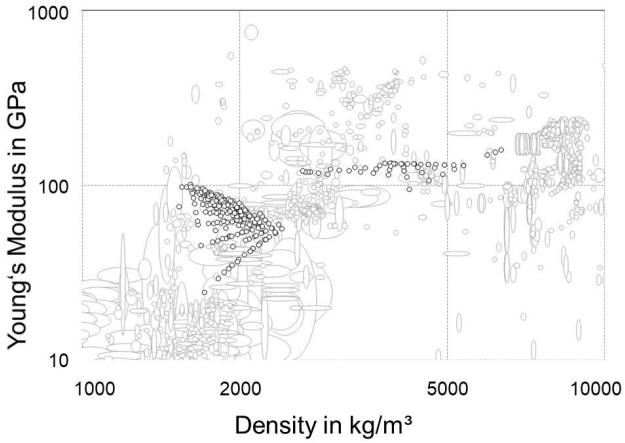

Figure 3.3: Materials selection chart with the data points for the laminates

Figure 3.3 shows the data obtained using CES EduPack with different constituent thicknesses and layer successions. Every combination of thickness and succession can be calculated and presented in a stiffness-density diagram to select the best possible laminate. Each data point in figure 3.3 resembles one possible laminate.

Layer succession

The position of a layer in the laminate impacts the axial moment of inertia. The stiffness difference of the constituents combined with the position in the laminate changes the stiffness of the laminate. The contribution of each layer to the laminate was calculated using the parallel axis theorem. All successions were calculated and visualized in the materials selection chart 3.3.

Layer thickness

The constituent layer thickness and therefore the constituent volume fraction in the laminate was used to optimize the flexural stiffness. The constituents had a minimum thickness caused by the manufacturing process of the single layers, which is presented in table 3.1.

Constituent	Minimum thickness
FRP	0.1 mm
Metal	0.3 mm
Elastomer	0.5 mm

Table 3.1: Minimum thickness of each constituent for the laminate

The thickness of the constituents could be varied within the overall laminate thickness of 2.5 mm to optimize the laminate.

3.2 Results of the materials selection

The materials selection was used to firstly select constituent materials according to the laminate's optimization goal. The subsequent step simultaneously defined the layer number, layer thickness and constituent succession. Restrictions like the elastomer interlayers and minimum layer thickness as presented in figure 3.1 of the selected materials was considered.

3.2.1 Results of the constituents selection

The material selection to define the constituents was conducted to achieve high flexural stiffness while preserving a low density. Equation 3.3 presented the material index $M = \rho/E^{1/3}$, which already indicated that a density reduction would be more effective than an increase in stiffness. The index is presented by a dashed line in figure 3.4. Every point on the line has the same material index and therefore an equal suitability for the application in the laminate. The optimum material can be found in the top left corner by parallel translation of the dashed line. The material that is crossed last by the line has the best material index and is suited best for the application. The elastomer cannot be found in the materials selection for the constituents, because it was included due to a restriction and lacked the high mechanical properties of the other constituents. Technical ceramics were excluded from the selection, because of unsuitable behavior under tension loads and high crack propagation rates.

The data and selection was conducted using the software CES EduPack by Granta Design Ltd. The red field shows the metals, the dark red field represents the composites and the yellow fields are ceramics. The dashed line shows the material index and suitable materials were labeled to show the selection possibilities. The metals are represented in black font and the FRP in grey font.

Figure 3.4 shows that the selection for the metal constituent chose magnesium followed by aluminum alloys. The material index of steel has a notable distance to the other two materials, showing the importance of density compared to the stiffness. Magnesium did not meet the constraints due to the strength-differential effect and the commercial unavailability in thin sheets and was eliminated from the group of possible constituents. The final metal layer selection ranked the aluminum ahead of steel sheets.

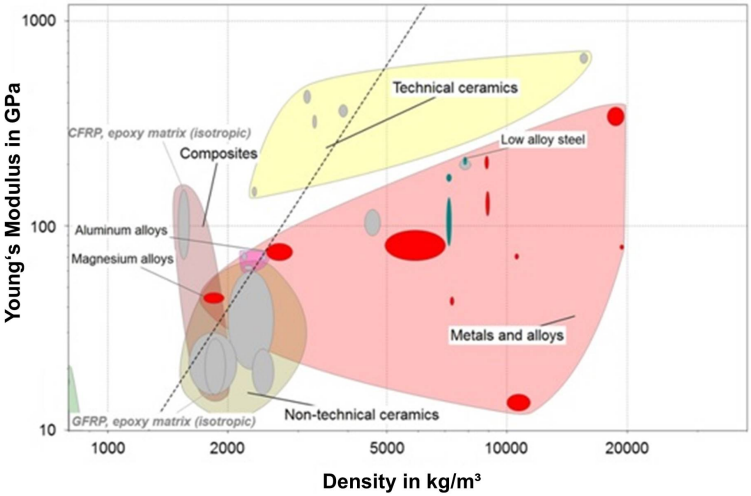

Figure 3.4: Materials selection chart for FMEL constituents with the index for high flexural stiffness and low density designed with CES EduPack [146]

The selection process also focused on the fiber reinforced polymer constituent. GFRP and CFRP are marked in the diagram as the two most prominent FRP material systems. The carbon fiber presented a higher lightweight potential compared to the glass fiber in figure 3.4. The comparison led to the result, that the carbon fiber, having a lower density and higher stiffness, was suited better for the application in the laminate. An epoxy matrix was selected because of beneficial production cycle times, availability and adhesion properties.

The constituent materials are presented in table 3.2. Two aluminum layers were pre-selected, as the selection process did not specify the alloy. Also a steel layer was pre-selected to show higher overall properties at a higher density. The selected elastomer interlayer SAA9579-52 possessed good adhesion to epoxy and aluminum and low curing cycle durations.

Table 3.2: Possible constituents selected by the materials selection

metal sheet	elastomer interlayer	FRP layer
Aluminum 2024-T3	Kraibon SAA9579-52	Hexcel CFRP prepreg
Aluminum 5754		
Steel TS275		

3.2.2 Results of the laminate selection

After the constituents were selected the optimal position of a constituent in the laminate was varied. The layer thickness of each layer was modified within the given restrictions to plot every possible laminate in a materials selection chart and select the best laminate.
The minimum constituent layer thickness only allowed five-layer laminates with a 2.5 mm overall thickness. The material with high stiffness was placed in the outer fiber to obtain a high overall stiffness, the highest values for flexural stress and axial moment of inertia are found in the outer fiber.
The different laminates had a variety of material indices and therefore a different suitability for the application in the laminate. Every possible laminate was visualized in figure 3.5.
Figure 3.5 shows a stiffness-density materials selection chart. Every colored point in figure 3.5 represents one laminate with a specific constituent succession and layer thickness. The laminates are color coded depending on the metal sheet to visualize the impact of the metal. The red and green data points, resembling Al 5754 and Al 2024-T3, were found in the same area, because the alloys possessed approximately the same stiffness and density. The yellow data points, marking the laminates featuring steel sheets, were found at higher stiffness and higher density.

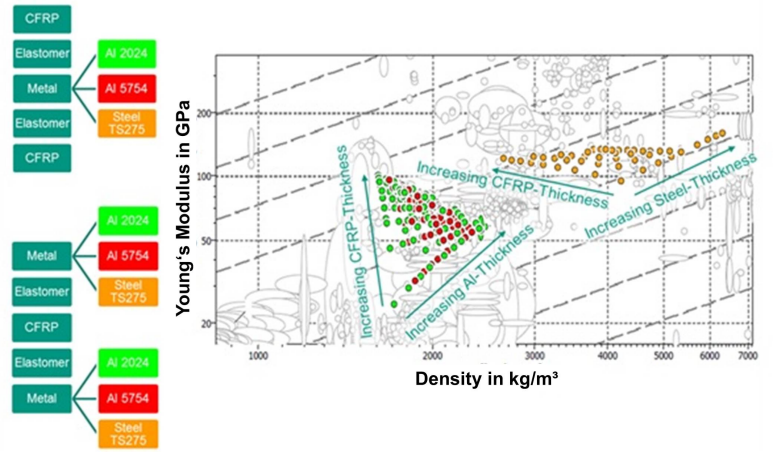

Figure 3.5: Materials selection chart for FMEL laminates with different successions and constituent thicknesses with the selection lines for high flexural stiffness and low density [146]

The possible layer successions are shown on the left side of figure 3.5. The succession with the CFRP in the face layer had higher properties than the configurations with metal face layers. The CFRP was the component with the highest stiffness and therefore was placed in the outer fiber. The layer thickness was indicated in figure 3.5 with arrows marking increasing constituent thickness of the metal and CFRP layer. Decreasing CFRP and metal layer thickness resulted in increased elastomer layer thickness, but caused a drop in stiffness.

An increase of metal thickness resulted in increased laminate stiffness. Thicker steel sheets increased the density and nullified the gain in stiffness. Thick aluminum layers increased the stiffness, but did not compensate the higher density.

An increase in CFRP thickness decreased the density and increased the stiffness, which suited both objectives. The CFRP layer thickness was maximized, while the other layer thicknesses were minimized.

The aluminum layers were selected over the steel sheets, while the aluminum alloy 2024-T3 was selected due to higher strength and better comparability to GLARE. The resulting position of the individual layers and the constituent thickness is presented in table 3.3.

Table 3.3: Constituents thickness and position in the laminate

constituent	position	thickness
Hexcel CFRP prepreg	face layer	0.6 mm
Kraibon SAA9579-52	interlayer	0.5 mm
Aluminum 2024-T3	core layer	0.3 mm

3.2.3 Discussion of the materials selection

The selection resulted in CFRP face sheets to improve the overall stiffness by maximizing the distance from the neutral fiber. The CFRP layer thickness, which had the highest stiffness, was maximized as it is presented in table 3.3. The elastomer interlayer was situated between each metal and CFRP layer to obtain objectives not covered by the materials selection. Due to the low contribution to the flexural stiffness, the thickness was kept minimal. The aluminum core layer thickness was also minimized due to higher density compared to the CFRP. The resulting laminate consisted of 0.6 mm CFRP face sheets, 0.5 mm elastomer interlayers and a 0.3 mm aluminum core layer.

The aluminum selected is already used in aviation in GLARE, which ensured good quality and comparability [16]. The CFRP was desired to cause higher mechanical properties of the laminate compared to GLARE [2].

The elastomer interlayer was selected using criteria outside of the materials selection, which were used to enable environmental stability, which was already indicated in hygrothermal conditioning [41].

The combination of the aluminum and the CFRP was not applicable without an interlayer solving interfacial problems, as galvanic corrosion was found between the carbon fibers and the aluminum constituent [12, 71].
The mechanical properties obtained from the calculation could be compared with GLARE. The stiffness, which had a maximum at 104 GPa using unidirectional CFRP in the laminate was higher than the maximum 69 GPa of GLARE. The density of the FMEL was lower at $1.5\,\mathrm{g/cm^3}$ compared to $2.4\,\mathrm{g/cm^3}$ of GLARE [20]. The elastomer interlayer did not carry a significant part of the load and therefore reduced the properties of the other constituents. Subsequently a laminate of CFRP and aluminum would result in higher properties and could easily surpass the stiffness to density ratio of FMEL and GLARE. A higher layer number resulting in more interfaces and a higher crack stopping effect could be obtained, if the elastomer layer was either thinner or omitted. However, the corrosion and CTE-mismatch could render a laminate consisting of CFRP and aluminum inapplicable and the interlayer was crucial for the constituent combination [12, 13].

4 Experimental

This chapter will present the materials used in the laminate and descriptions of the experimental procedures used to characterize the laminates. The utilized experimental setups will be shown, which were employed to measure the behavior of the specimens. The chapter will start with the materials, before presenting the experiments determining the manufacturing quality. The experiments to determine the interfacial properties will be visualized and subsequently tests to determine quasi-static and dynamic properties will be shown, before closing with fatigue and thermal mechanical fatigue experiments. The properties of FMEL were compared to FML to analyze the effect of the elastomer interlayer.

4.1 Materials investigated

The laminate consisted of an aluminum sheet, elastomer interlayers and CFRP layers as selected and optimized in chapter 3. The standard configuration had 0.6 mm CFRP face sheets, 0.5 mm elastomer interlayers and a 0.3 mm aluminum core resulting in a 2.5 mm thick five-layer laminate.

4.1.1 Carbon fiber reinforced polymer

The carbon fiber reinforced polymer used in this study was a prepreg by Hexcel named "HexPly M77/42%/UD90/CHS". It consisted of a fast curing epoxy matrix to enable short process cycle times and high strength carbon fibers.

The unidirectional orientation of the fibers ensured high mechanical properties. The matrix weight content was 42 %, which resulted in an approximate fiber volume content of 50 % in the cured layer. The resulting layer had a thickness of 0.1 mm, density of 1.5 g/cm^3 with a stiffness of 117 GPa and strength of 2250 MPa [129]. The unidirectional CFRP layers were stacked to obtain a bidirectional layer in the succession $[0°/90°/0°/0°/90°/0°]$.

4.1.2 Metal layer

The metal layer in the laminate was an aluminum alloy 2024-T3. The alloy was solution heat-treated, cold-worked and naturally aged to a substantially stable condition. It was used in many research FMLs and in GLARE, which ensured comparability.
The aluminum alloy had a density of 2.76 g/cm^3, a stiffness of 73 GPa and a tensile strength of 430 MPa [130].

4.1.3 Elastomer interlayer

The elastomer for the interlayer was provided by Kraiburg Holding GmbH & Co. KG and is commmercially called Kraibon. The elastomer compound SAA9579/52 was used because of enhanced adhesive properties to the epoxy matrix of the CFRP and the aluminum core layer. The elastomer layer was supplied in a pre-cured state and cured in the same process step as the CFRP.
The elastomer had a strain to failure of 200 %, a stiffness of 50 MPa with a maximum stress of 8.3 MPa. The density of the cured layer was 1.18 g/cm^3 and the electrical resistance through the layer was $3x10^{12}\ \Omega * cm$ [131].

4.2 Laminate manufacturing

The curing cycle for the laminate was conducted in a press for 300 s at 150 °C with a pressure of 23 bar, as the minimum pressure of 5 bar, which was specified by the manufacturers, resulted in emerging porosity [132]. The cycle time of 300 s was defined by the elastomer layer, as the CFRP was already fully cured after 120 s [133]. The laminate was manufactured as a sheet of 300 mm x 300 mm with a thickness of 2.5 mm. The FML, which lacked the elastomer interlayer, had a thickness of 1.5 mm and had the identical CFRP and aluminum layers as the FMEL.
The specimens for mechanical testing were cut out of the laminate using water jet cutting.

Table 4.1: Laminates investigated

	FMEL	FML	CFRP
Face layers	0.6 mm CFRP	0.6 mm CFRP $*$	0.6 mm CFRP $*$
Interlayers	0.5 mm elastomer	-	-
Core layer	0.3 mm aluminum	0.3 mm aluminum	-
Thickness	2.5 mm	1.5 mm	0.6 mm

The laminates investigated in this work are presented in table 4.1. The laminate thickness varied, because the layers were kept constant. However, when the axial moment of inertia of the specimens was important, the thickness of the layers marked with an asterisk were increased to form a 2.5 mm thick laminate.

4.3 Microstructure and interface characterization

4.3.1 X-ray imaging and CT-scans

Computed tomographic x-ray scans (CT-scans) were conducted to examine the manufactured laminates and detect pores. An Yxlon Y.CT Precision μCT-system computer tomograph was used with a detector resolution of 2048 pixels x 2048 pixels. The tube was operated at 230 kV acceleration voltage and 0.3 mA current. The detection of pores was carried out by X-ray imaging of the complete laminate structure using greyscale correlation. The imaging could be conducted for large structures to find inhomogeneous zones, however, the characteristics of the pores could not be visualized due to low resolution. The 300 mm x 300 mm x 2.5 mm laminate was examined with 4 images, each visualizing one quarter of the laminate. The subsequent pore characterization was conducted using CT-scans of the regions of interest detected by the X-ray imaging.

CT-scans were conducted on small specimens that indicated inhomogeneous structures in the X-ray images. The small samples enabled a higher resolution to further describe the pores and allow understanding the origin of the inhomogeneity. The CT specimens were round with a diameter of 20 mm and a thickness of 2.5 mm, which corresponds to the laminate thickness. The pore analysis was conducted using the software VGStudio MAX by Volume Graphics GmbH.

CT-scans were used to visualize damage in the laminate caused by the manufacturing process and to determine the quality of the laminate prior to mechanical testing.

4.3.2 Microstructural analysis

Cross-section polishes were executed to visualize the constituents and the interface of the laminate. The topography of the interface could be analyzed to correlate the interfacial properties to the results of mechanical testing.
For the polish 10 mm x 10 mm x 2.5 mm specimens were embedded into a particle reinforced polymer mass, grinded down and polished to obtain a smooth surface. Images were taken using a microscope to show the constituents and the interfaces.

4.3.3 Edge shear tests

The edge shear test [64] was used to determine the interfacial shear properties. It can evaluate the shear energy until failure additionally to the shear strength, which can be used to better describe ductile failure mechanisms. The shear energy is defined as the absorbed energy until failure.
The specimen size for the edge shear was 20 mm x 10 mm x 2.5 mm and the shorter side was put vertically into the experimental setup. The specimen dimensions were measured before testing using a micrometer screw.

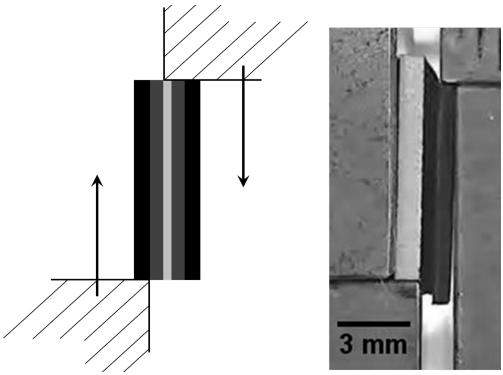

Figure 4.1: A schematic of an FMEL specimen in the edge shear test (left) and the specimen in the experiment (right)

Figure 4.1 shows on the left side the two edges, which move towards each other to induce shear stress into the specimen. The image on the right side shows an asymmetric FMEL specimen in the edge shear test. The guiding plates on either sides of the FMEL are adjustable to define the shear plane.
A ZwickRoell Zmart.PRO 100 kN universal testing machine was used with a 20 kN load cell. The experiment was carried out at 1 mm/min crosshead velocity. The displacement was measured using an inductive strain transducer.
The test started after a force of 10 N was reached and finished after the force decreased by 20 %. The software TestXpert II by Zwick was used to calculate the results. Ten specimens were used for each laminate.

4.4 Characterization of quasi-static properties

FML and FMEL were examined quasi-statically to compare and contrast the laminate performances and analyze the influence of the elastomer interlayer. The quasi-static experiments were conducted to evaluate, define and describe the mechanical behavior of the laminates under different loading conditions. The experiments included tensile, compressive and flexural experiments to define the load bearing capability. DCB and puncture tests defined the crack propagation, while corrosion and thermal cycling experiments characterized the fitness for application in critical environments.

4.4.1 Tensile tests

Tensile tests were conducted according to DIN EN ISO 527-5 [134] to obtain the stiffness, yield and tensile strength and the correlating strains for the laminates and their constituents. The stiffness was calculated by regression between 0.05 % and 0.25 % strain. The specimen size was 250 mm x 15 mm x 2.5 mm.

A ZwickRoell ZMART.PRO 200 kN universal testing machine with an integrated extensometer was used for the experiments. The measuring length of the extensometer was 100 mm. Hydraulic grippers were used for load introduction. The experiment was carried out nominally strain controlled at 1 %/min and the failure criterion was a decrease of 20 % in force. The force applied before testing was 20 N. The results were analyzed using the software TestXpert II by Zwick. Per laminate five valid specimens were tested.

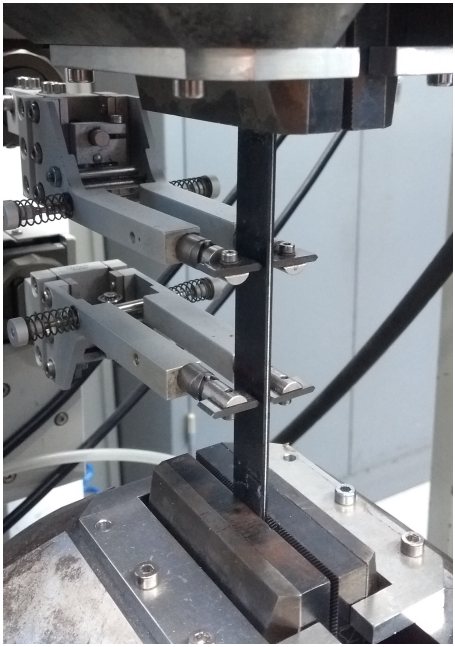

Figure 4.2: Experimental setup for tensile tests using hydraulic grippers and an extensometer

4.4.2 Compression tests

Compression tests were carried out according to DIN EN ISO 14126 [135].

The compression testing setup is visualized in figure 4.3, which shows the hydraulic gripping and the specimen with cap strips. Two mini MFA2 strain transducers by Mess- & Feinwerktechnik GmbH were used to obtain strain values and analyze the bending factor of the experiment. A Zwick-Roell ZMART.PRO 100kN universal testing machine with a testing speed of 1 %/min was used. The compressive modulus, compressive strength and strain were examined. The specimen size was 110 mm x 10 mm x 2.5 mm. 2 mm thick Aluminum cap strips were used in the gripping area, which defined the free length of 10 mm.

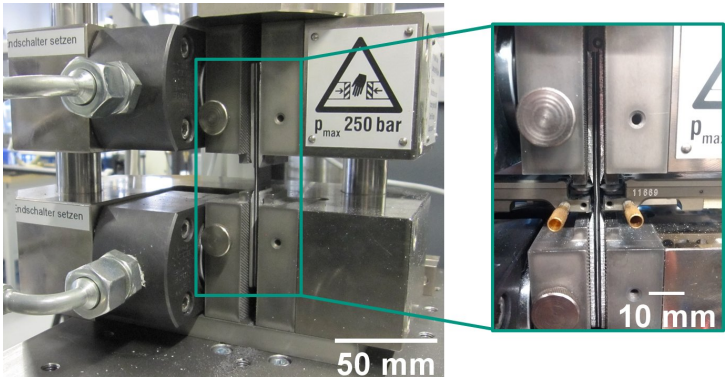

Figure 4.3: Image of the compression test setup (left) with an FMEL specimen and strain transducers (right)

A force of 10 N was applied before the experiment was started and a decrease of force by 20 % defined the end of the test. The software TestXpert II by Zwick was used for determination of stiffness, strength and strain values. Ten specimens were used per laminate to define the compressive properties.

4.4.3 Bending tests

Bending experiments were conducted to obtain the flexural stiffness and strength of the specimens.

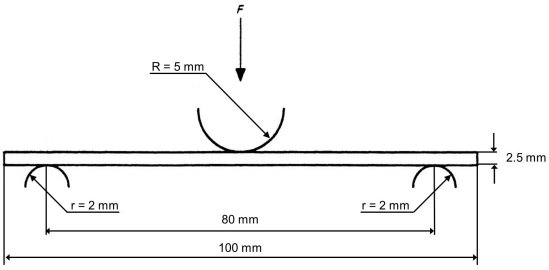

Figure 4.4: Schematic of the flexural testing setup with dimensions [136]

The experiment was carried out nominally strain controlled at 1 %/min. A universal testing machine from ZwickRoell with a 2.5 kN load cell was used. The strain was measured using an inductive strain transducer positioned opposite the upper support. The experiments were carried out according to DIN EN ISO 14125 [136].
The schematic in figure 4.4 shows the specimen in the experimental setup. The specimen size was 100 mm x 15 mm x 2.5 mm.

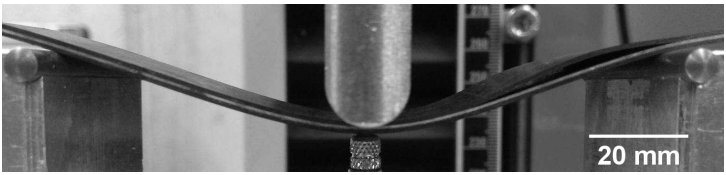

Figure 4.5: 3-point bending experiment on FMEL

Figure 4.5 shows the experimental setup for the bending experiments.Additionally to the mechanical properties, conclusions are drawn from the failure mechanisms, such as delamination, which represented premature failure.
The experiment was started after a force of 5 N was applied and finished after the force decreased by 20 %. The software used to obtain results was TestXpert II by ZwickRoell. Five specimens were used per laminate to define the bending properties.

4.4.4 Crack propagation tests

The double cantilever beam test (DCB) was carried out using a ZwickRoell universal testing machine with a 2.5 kN load cell. The experiment was conducted according to ASTM D5528 [137].
Teflon foil was used to prevent adhesion in the pre-crack and define the initial crack length of 50 mm. The specimens' dimensions were 250 mm x 25 mm x 2.5 mm.

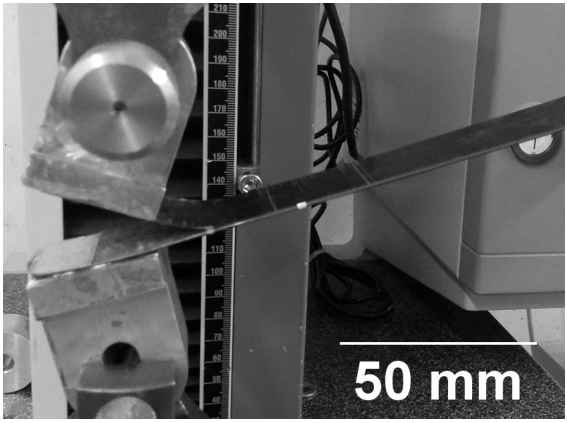

Figure 4.6: FMEL specimen with aluminum load introduction blocks in the double cantilever beam test

Figure 4.6 shows the load introduction in the loading blocks, which were adhesively bonded to the specimens by UHU Endfest 300 cured at ambient temperature for 24 h. The crack tip was observed optically and the traverse speed was 1 mm/min. The software used to analyze the data was TestXpert II by Zwick. Five valid specimens were tested.

4.4.5 Puncture tests

Puncture tests were conducted on a ZwickRoell ZMART.PRO 500 kN universal testing machine with a 20 kN load cell. The specimen diameter was 60 mm, the thickness 2.5 mm and the specimen was clamped between the supporting structures with a central hole with a diameter of 40 mm. The penetrator was an extended half sphere with a 10 mm diameter and the traverse speed was 1 mm/min. The experiment was filmed from below with a 3D digital image correlation (DIC) stereo camera system called ARAMIS 4M by GOM to monitor the failure mechanism and obtain the three-dimensional deformation. The experiments were conducted according to DIN EN ISO 6603 [138], but at a traverse speed of 1 mm/min to obtain the quasi-static experiment.

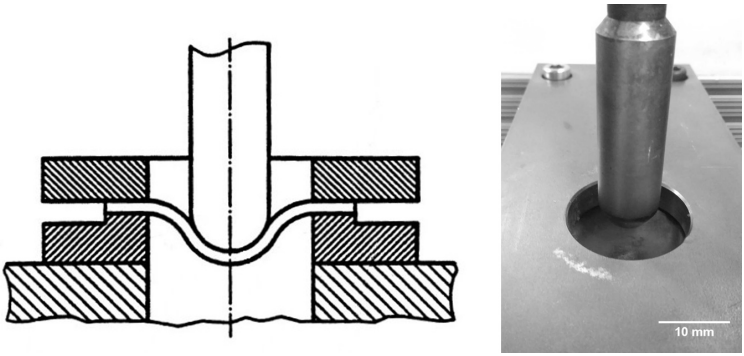

Figure 4.7: Enlarged specimen area of the puncture test [138] (left) and the experimental setup for puncture tests (right)

Figure 4.7 shows the puncture setup with the clamping of the specimen. This setup was used for quasi-static and dynamic puncture tests. Only the ex-situ puncture tests in the CT were conducted on a different setup as presented in figure 4.8.

To examine the laminates further and enable delamination detection, the puncture tests were also assisted by CT-scans. Ex-situ CT-scans were conducted, meaning that the laminate was loaded incrementally and scanned at each load level.

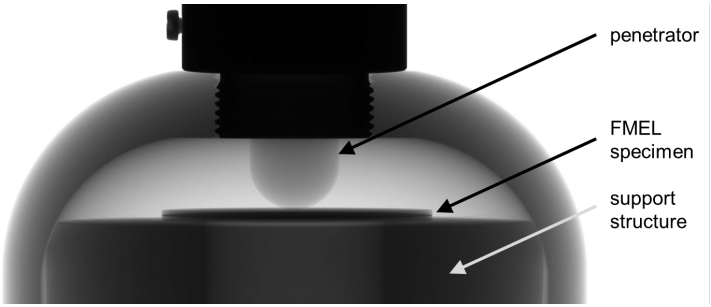

Figure 4.8: X-ray image of the puncture test setup in the CT

Figure 4.8 shows the FMEL laminate in the ex-situ CT puncture test setup. The laminate is situated in the center of the picture. The penetrator with the spherical tip is directly above the specimen and the laminate is positioned on a support structure with a central circular hole with 40 mm diameter. The outer support structure is used to close the load path so the puncture test setup could be transferred from the testing machine to the CT to visualize deformation and damage under load.

4.4.6 Environmental stress tests

Laminates combining two different materials often carry risks caused by environmental loads such as the aforementioned galvanic corrosion. Corrosion tests were conducted to determine the isolating effect of the elastomer interlayer. Also thermal cycling tests evaluated the damage by the CTE-mismatch to define the benefit of the elastomer interlayer.

Temperature cycling tests

To evaluate the laminate and its properties concerning the CTE-mismatch, the laminate was placed in a climatic chamber without external loads. The thermally cycled FMEL and FML were compared to non-exposed FMEL and FML to show the change of interfacial properties.
The thermal load was taken from the automobile industry, where the thermal range was defined to be within $-20\,^{\circ}\mathrm{C}$ and $80\,^{\circ}\mathrm{C}$ [71]. The cycle was carried out in a Vötsch VCL7010 climatic chamber for 90 min.
The residual properties after 100, 1000 and 10000 thermal cycles was measured to determine the amount of damage caused by the thermal stress. Residual properties were tested using edge shear experiments with ten specimens for each cycle number to examine the impact of the CTE-mismatch on the interfacial properties.

Corrosion tests

The corrosive properties of the laminates were examined in neutral salt spray tests. The experiments were carried out according to DIN EN ISO 9227 [139]. The specimens were placed in a salt spray chamber for 24 h, 48 h and 96 h. The specimens were situated at an angle of $20\,^{\circ}$ to prevent salt water drops from remaining on the surface and uncontrollably increasing corrosion.
The interface was expected to be influenced the most. The residual interfacial properties of FMEL and FML were examined using edge shear tests with ten specimens per laminate.

4.5 Characterization of dynamic properties

4.5.1 Charpy tests

Charpy tests were conducted according to DIN EN ISO 179 [140]. A Zwick-Roell HIT5.5P machine was used with a pendulum energy of 5 J to hit the specimen flatwise. Only the absorbed energy was monitored, after the influence of the friction was measured and excluded from the results.

Figure 4.9: FMEL specimen in the experimental setup for charpy testing

Figure 4.9 shows the charpy pendulum hitting the specimen. The specimen was hit in thickness direction, which is the most realistic direction for application. The specimen size was 32.5 mm x 15 mm x 2.5 mm with a support width of 20 mm. For every laminate ten specimens were tested.

4.5.2 Puncture tests

Puncture tests were conducted according to DIN EN ISO 6603 [138] on an Instron Dynatup 9250HV testing machine with a 22.241 kN (5000 lbs) load cell. The specimens were identical to quasi-static puncture tests and the same experimental setup, penetrator and support structure were used. The specimen had a diameter of 60 mm and a thickness of 2.5 mm.
The penetrator speed was set to 4.4 m/s. The force and displacement were measured in the experiment.

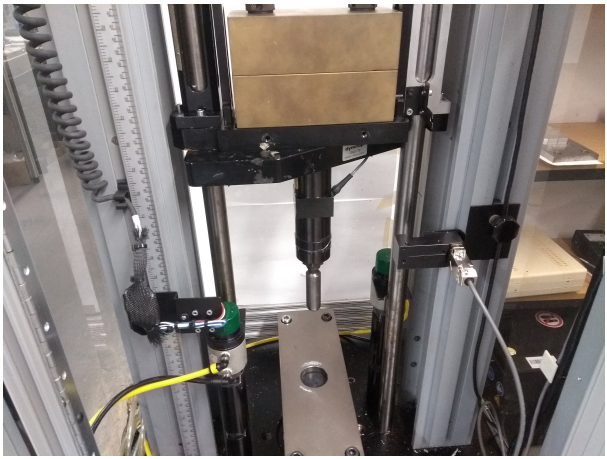

Figure 4.10: Experimental setup for puncture testing

Figure 4.10 shows the experimental setup, where the penetrator is pulled upwards and accelerated towards the specimen, which is clamped like in the quasi-static puncture tests. The number of specimens per laminate was set to 5.

4.5.3 Impact tests

Impact tests were conducted using an Instron Dynatup 9250HV testing machine. The specimen dimensions were 150 mm x 100 mm x 2.5 mm. A steel sphere was dropped with a defined energy onto the laminate to induce damage like presented by Dietrich et al. [83]. The experiment was filmed from the front using a high speed camera to determine the speed of the sphere. The damage to the laminate was monitored optically and the residual strength was measured to characterize the damage tolerance.
A MotionXtra NX4 high speed camera by Integrated Design Tools, Inc. was used to film the experiment in order to calculate the plastic and elastic energy absorbed by the laminate. The frame rate was set to 9 kHz with a resolution of 992 pixels x 336 pixels. The long side of the image was vertical to increase the measurement quality. The setup was illuminated by two synchronized LED lights. The high speed imaging was triggered by a motion sensor of the testing machine.

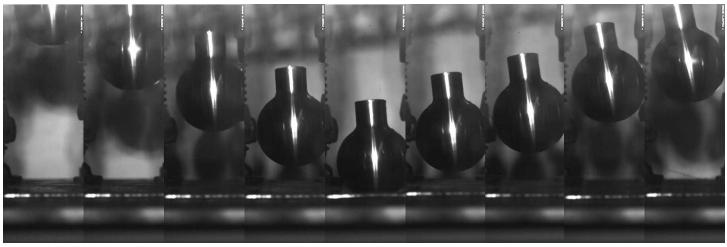

Figure 4.11: Frames of the impact experiment captured by high speed imaging

The image resolution resulted in a distance per pixel of 0.166 mm/pixel. Figure 4.11 shows the images over time during the experiment with a time step of approximately 0.0025 s between the images. The image stack was rotated by 90 ° to obtain an image stack with height and time on the axes.

Figure 4.12: Image of the impactor and central frame over time diagram in the impact experiment

Figure 4.12 shows on the front image one image of the high speed video of the falling impactor. The y axis over time image shows the impactor falling with a certain speed onto the laminate and ascending with a second, lower speed. The slope of the lines, defining the speed of the impactor, were obtained by tracking of the edges of the sphere. Figure 4.12 shows the impactor sphere over time during the experiment and figure 4.13 presents the identical relation of one cleared line representing the position over time. The images were analyzed using the software OriginPro by OriginLab through fitting straight lines to the slopes prior to the impact and after the impact. From the difference in impactor speed the energy absorbed by the laminate can be calculated, while neglecting the effect of gravity on the sphere. The assumption was executed due to the short distance monitored and the fact that measurements were conducted directly adjacent to the impact event.

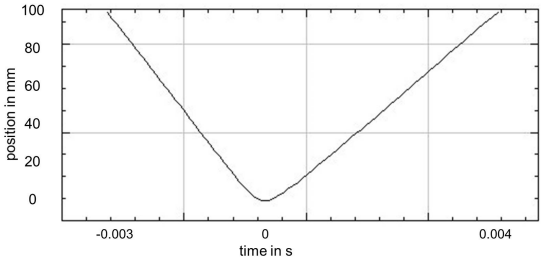

Figure 4.13: Position of the sphere over time during the impact test

Figure 4.13 shows the segmented line from figure 4.12. From this image the absorbed energy can directly be calculated. There were three specimens tested per laminate and impact energy.

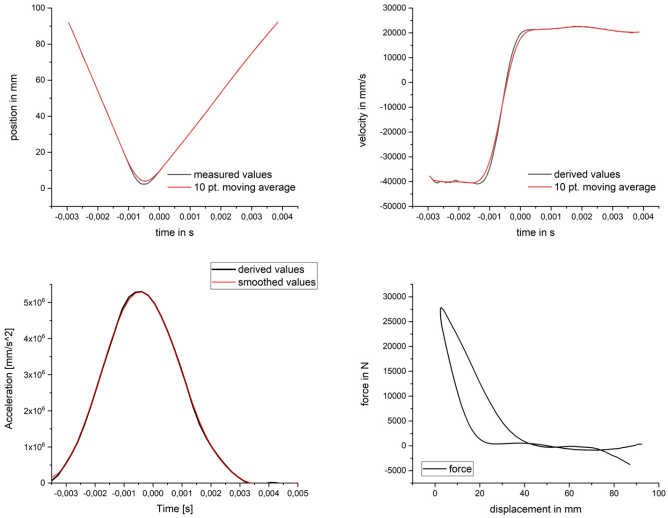

Figure 4.14: Exemplary impact analysis for FMEL at intermediate impact energy starting from position versus time diagram, over velocity to acceleration versus time to obtain a force displacement graph

The first image in figure 4.14 shows the position of the impactor tracked throughout the experiment. The graph shows a position versus time diagram of the sphere. Additionally a 10 point moving average was used to smoothen the curve and enable better results for the next graph which was obtained by differentiating the first graph by the time. The velocity over time graph was derived, which could be used to calculate the kinetic energies of the impactor before and after impact. This graph was smoothened by the moving average to ensure better differentiation. With another derivation step the acceleration is shown in the lower left image. The acceleration could be used to derive the force with respect to the experiment time. Since the time versus position diagram was known in the top left image, a force displacement diagram could be derived from the lower left graph and was visualized in the lower right image. From the area enveloped by the graph, the absorbed energy could be calculated. The graph can be validated by calculating the maximum force and absorbed energy using the velocity of the impactor of the upper right image to verify the calculations.

4.5.4 Compression after impact tests

To determine the residual strength of the laminate specimens after impact, compression after impact tests (CAI) were conducted according to DIN ISO 18352 [141] using a 100 kN ZwickRoell ZMART.PRO universal testing machine. The out-of-plane deformation was measured using an inductive strain transducer on the back of the impact zone. The in-plane deformation was measured by the crosshead position of the machine.

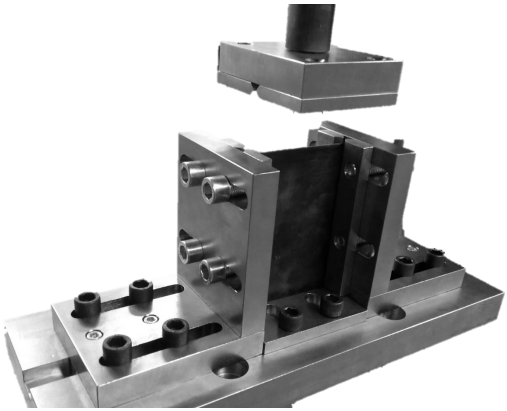

Figure 4.15: Testing setup of the compression after impact test

Figure 4.15 shows the testing setup for the compression after impact tests. The specimens were fixed at the edges from both sides to inhibit bending and buckling. The experimental speed was 1 mm/min and all laminates tested in the impact test were also tested in the compression after impact tests. Reference specimens without impact load were tested to define the damage done by the impact.

4.6 Fatigue experiments and lifetime prediction

Tension-tension fatigue experiments were conducted and compared with a lifetime prediction. Additionally thermal mechanical fatigue was carried out to superimpose fatigue loading with thermal cycling.

4.6.1 Fatigue tests

Tension-tension fatigue experiments were conducted with a failure criterion of 20 % stiffness decrease according to ISO 13003 [100].
The fatigue experiments were conducted on a servo-hydraulic universal testing machine by Schenck with a 100 kN load cell. R = 0.1 was used to characterize the behavior of the laminate.
Hydraulic grippers and a manipulation to prevent torsion loads were used. The testing frequency was 5 Hz and the temperature increase threshold was 5 °C, which when exceeded would render the experiment invalid. The specimens dimensions were 250 mm x 25 mm x 2.5 mm and the gauge length was set to 150 mm. No cap strips were necessary, except for the specimens used for CT-imaging, which were repeatedly mounted.
The cap strips had the dimensions 50 mm x 25 mm x 1 mm. The side facing the measuring length gradually decreased in thickness to inhibit a sharp stiffness drop. The experiments were carried out stress controlled and four specimens per load level were tested. The load level was set in percentiles of the ultimate tensile strength (UTS) as defined in the standard [100].

Load levels

The load levels in respect to the UTS were 25 %, 40 %, 55 % and 80 %. The ultimate tensile strength was the laminate strength, but using the strain rate of the fatigue experiment to account for strain rate dependent behavior.

Table 4.2: Stress levels and strain rates for the fatigue testing

percentile of UTS	mean stress	stress amplitude	strain rate
80 %	145 MPa	120 MPa	4.8 %/s
55 %	100.5 MPa	82.5 MPa	3.6 %/s
40 %	72 MPa	60 MPa	2.4 %/s
25 %	45 MPa	37.5 MPa	1.2 %/s

Table 4.2 shows that with different stress amplitudes and constant frequency the strain rate varied among load levels, which could result in variation of the temperature increase of the specimen.
The UTS of FML was higher than in FMEL by the factor 5/3 accounting for the lower cross section area due to the lack of the interlayers. The load levels for the laminate was set according to the UTS of FMEL to ensure comparability.

Damage detection

Polymers under cyclic loading show internal friction and increasing temperature. The temperature was monitored using a T420 infrared camera by FLIR. The specimen temperature increase during the experiment was compared to the 5 °C threshold stated by ISO 13003 [100].
CT-scans aided the damage detection during fatigue experiments, which were carried out according to the description in section 4.3.1. Specimens were mounted in the fatigue setup and loaded for 1000 cycles, dismounted and scanned in the CT before repeating the procedure. The specimens were reinforced in the gripping area with aluminum cap strips to prevent premature failure due to repeated mounting.

4.6.2 Lifetime prediction

A lifetime prediction for FMEL under tension-tension fatigue at R=0.1 was conducted. Since the laminate consisted of different constituents, a simple prediction for the whole laminate was not applicable. The approach was to superimpose lifetime predictions of the individual constituents to generate a prediction for the laminate.
The basis for the superposition was the assumption of an iso-strain state throughout the experiment. The stress in any given cycle was calculated for the constituents and factored into the lifetime prediction for the laminate. Therefore, stress redistributions due to damage within the fatigue experiment were accounted for.
The lifetime prediction was generally applicable for both laminates, because the load bearing layers were identical.

Prediction for the aluminum layers

The lifetime prediction for the aluminum constituent was conducted according to Coffin-Manson, because the initial stress level in the aluminum indicated low cycle fatigue failure. It was assumed that the load bearing capability of the aluminum in the laminate was reduced to zero, when the cycles to failure were met.
The dominating mechanism in low cycle fatigue is described by equation 4.1, which accounts for loads leading to plastic strain in the material.

$$\frac{\Delta\varepsilon_{pl}}{2} = \varepsilon_f^{'}(N_B)^c \tag{4.1}$$

The equation describes the relation of plastic strain ε_{pl} and the cycles to failure N_B using the fatigue ductility coefficient $\varepsilon_f^{'}$ and the fatigue ductility exponent c.
The cycles to failure were calculated for the aluminum sheet and compared to the experimentally obtained cycles to failure.

Prediction for Elastomer interlayers

A lifetime prediction for the elastomer interlayers was not conducted, as the strain at failure of the laminate was calculated to be below 2.5 %. This left the strain to failure of the laminate well below the strain to failure for the elastomer constituent, which was approximately 200 %. Therefore, it was estimated that the elastomer would not fracture during fatigue testing.

Prediction for the CFRP layers

The lifetime prediction for the CFRP constituent was conducted according to the approach postulated by Ogin et al. [105]. The prediction based on matrix cracking for GFRP was applied to CFRP by Berthelot et al. and showed good compliance with experiments [142].
The prediction was based on the stiffness decrease caused by matrix cracking of the 90 ° CFRP layers, which should cause a stiffness decrease over the experimental duration until failure. The change of stiffness was brought into relation with the maximum stress endured during the experiment by equation 4.2. Figure 4.16 shows the change of stiffness per cycle depending on the load level. The double logarithmic fit visualizes the prediction for an arbitrary load level.

$$-\frac{1}{E_0}\frac{dE}{dN} = A\left(\frac{\sigma_{max}^2}{E_0^2(1-E/E_0)}\right)^n \tag{4.2}$$

Equation 4.2 shows the relation presented in figure 4.16 and presents the double logarithmic linearity of the change in stiffness and the maximum stress squared. The constants of the equation, A and n needed to be determined for the CFRP. Subsequently the equation can be integrated to present a relation of the current stiffness in the experiment and the corresponding load cycle.

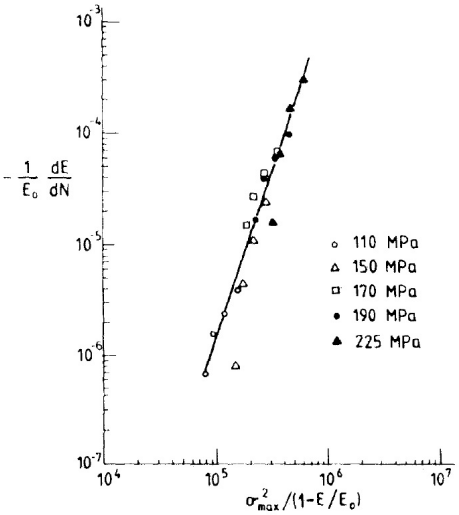

Figure 4.16: Diagram of the change of stiffness of GFRP during fatigue testing depending on the load level [105]

Prediction for the laminate

The lifetime prediction for the laminate was conducted by superposition of the predictions of the aluminum constituent and the CFRP layers. The interface was assumed to be intact throughout the whole fatigue testing, which was based on good quasi-static interfacial properties. In the fatigue experiments an iso-strain state was assumed in the specimens, which was used to calculate the stress in each constituent.

The aluminum was assumed to fracture at the predicted cycles to failure with no residual stiffness or strength, which required one recalculation step for the stress distribution in the laminate. The continuous stiffness decrease of the CFRP was factored constantly into the change in stress in the laminate. The projected changes in stress were factored into the lifetime predictions of the constituents.

The lifetime prediction for the laminate was calculated against a stiffness decrease of 20 %, which was projected to be met due to a combination of aluminum fracture and stiffness decrease of the CFRP. The resulting combined lifetime prediction then represented the whole laminate structure under the assumption of intact interfaces and elastomer interlayers.

4.6.3 Thermal mechanical fatigue tests

Thermal-Mechanical-Fatigue (TMF) is defined through superimposed synchronous cyclic thermal and mechanical loading. In this work in phase thermal and mechanical loads were investigated. The experiments were carried out strain controlled, where the first 10 cycles were used to determine the CTE of the specimen using a force controlled pretest, which actively controlled the force to 0 N. The following cycles took the strain caused by the CTE into account.

Mechanical cycling

The mechanical cycling of the TMF was carried out using an electric Zwick-Roell ZMART.Pro universal testing machine with a 100 kN load cell. Hydraulic grippers and 1 mm thick aluminum cap strips were used for the experiment. A triangular load scheme was applied as presented in figure 4.17 with the load ratio being $R = 0.1$. The strain was measured using a tactile capacitive strain transducer with a gauge length of 50 mm. The load levels were defined like the fatigue load levels at 80 %, 55 % and 40 % of UTS.
The mechanical cycling was generally conducted analogous to the tension-tension fatigue experiments. However, the mechanical cycling was conducted strain controlled, but the initial load levels were identical. The mechanical cycle was conducted over 188 s due to the thermal cycle instead of 0.2 s. Lastly, a triangular load scheme was used instead of a sinusoidal load to account for the thermal load, which was triangular.

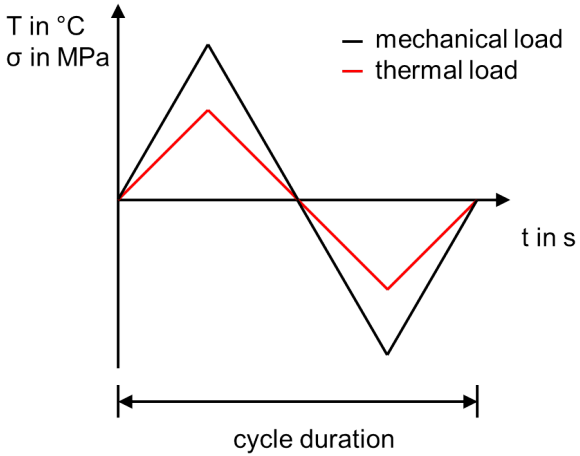

Figure 4.17: Mechanical and thermal load cycle of the TMF experiment

Thermal cycling

The thermal cycle to generate the climatic circumstances for the experiment was carried out from 10 °C to 80 °C. For this task a heating and cooling system was constructed using QuickCool QC-241-1.6-28.0 MM peltier elements. The temperature value for the thermal cycling was defined through the software of the universal testing machine, relayed through a logic controller and set the target value for the peltier elements.
A single peltier element had a surface of 50 mm x 50 mm, a maximum temperature difference of 66 °C and a maximum power of 430 W at a current of 28 A and a voltage of 27.7 V. The peltier elements were selected because of a high power density, which enabled a fast thermal cycle [143].
The climatic chamber, consisting of 4 peltier elements, enabled a testing area of 100 mm x 50 mm, resulting in a thermally loaded testing length of 100 mm of the specimens. The maximum heating and cooling power of the system was 1.720 W.

A separate power supply was used for every peltier element, but all power supplied were controlled by the same controller to ensure homogeneous temperatures without lag. The experiment was conducted for 1000 loadcycles, with a cycle duration of 188 s per cycle.

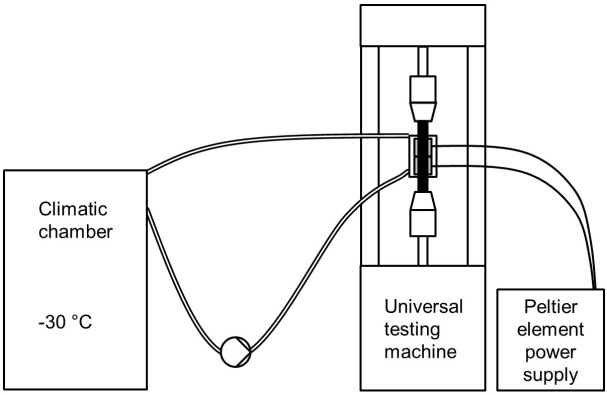

Figure 4.18: Schematic of the thermal cycling components for the TMF experiments containing a climatic chamber used for cooling the fluid, a pump for transferring the fluid and the housing of the peltier elements

Figure 4.18 shows a schematic of the thermal cycling setup. The peltier elements needed an active cooling to enable low temperatures at the specimen. The active cooling unit included a Vötsch VCL7010 climatic chamber and a cooling agent. The fluid was pumped into both sides of the aluminum housing of the peltier elements using a Grundfos Alpha 2 pump, which had a good pumping power while inducing only minimum heat into the fluid. The cooling medium was a mixture of Antifrogen N and water to enable cooling at the approximately constant temperature of $-30\,^{\circ}\mathrm{C}$.
The climatic chamber was positioned on the half-traverse, which ensured the thermally loaded region to remain in the climatic chamber and prevented relative movement through mechanical strain.

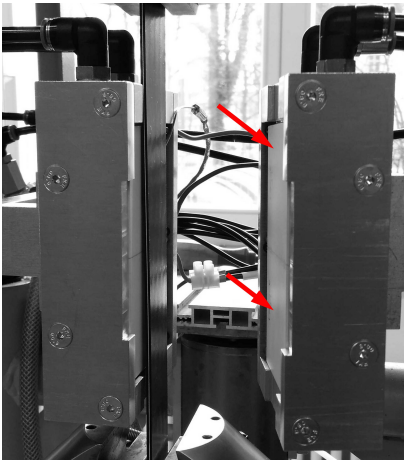

Figure 4.19: FMEL TMF specimen in the open peltier temperature chamber and arrows indicating the peltier element surfaces

Figure 4.19 shows the FMEL specimen in the temperature chamber, where the white ceramic surfaces of the peltier elements are visible. The peltier elements of the right side of the climatic chamber were indicated with arrows. The cooling medium connections to cool the backside of the elements are visible on top of the chamber while a thermocouple measured the specimen temperature.

The thermal cycling using peltier elements resulted in a thermal cycle from 10 °C to 80 °C. Lower minimum temperatures were desired, however, the excess heat produced by the peltier elements resulted in a temperature increase at the peltier backside.

The thermal cycle duration was increased from the minimum cycle time to generate a homogeneous temperature distribution in the specimens. Three specimens were tested for every TMF load level.

5 Results

5.1 Influence of process parameters on the laminate properties

The manufacturing process for the FMEL and FML was optimized at the Institute for Production Science (wbk), where the pressure, temperature and curing cycle duration were varied to determine the optimum process route for the FMEL as described in section 4.2. The influence of the process parameters on the laminate was examined optically and by analysis of the mechanical properties.

5.1.1 Process influence on the inner structure

Process induced flaws such as pores in the laminate can occur, which could be detected by X-ray imaging. The pressure of 5 bar was insufficient for defect-free laminates. The X-ray images were adapted using ImageJ [144] software to color the greyscale images for clearer visual confirmation of the pores as presented in the middle of figure 5.1.
Subsequently, to correlate the inhomogeneities in the X-ray images with pores, the laminate was delaminated to gain visual confirmation of the inner structure. The resulting fracture surface shows the aluminum layer with residual elastomer, where the adhesion was good on the right side of figure 5.1. The pores were found in the laminate manufactured at 5 bar.

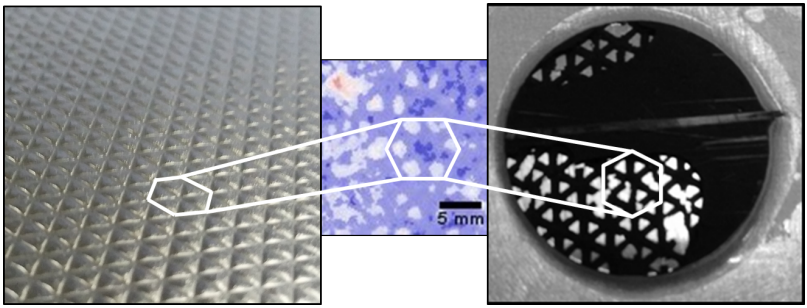

Figure 5.1: Surface of the elastomer layer (left), pores after the manufacturing process with 5 bar in an x-ray image (middle) and after delamination on the specimen (right)

Figure 5.1 presents on the left the surface structure of the uncured elastomer layer as received. The elastomer has as surface structure with triangles oriented in a hexagonal structure originating from the calendering process of the manufacturer. The X-ray image also exhibited a hexagonal pattern, which is shown in the middle image and a hexagon is highlighted. After the delamination, residual elastomer adhered to the aluminum. The locations, where the constituents were separated presented a hexagonal pattern on the aluminum.
The specimen presented in figure 5.1 was also scanned in the CT to gather three-dimensional information about the pores. The pore analysis and three-dimensional images were obtained with the software VGStudio MAX. The specimen with a three layer layup is presented in figure 5.2.

The specimen contained three layers, CFRP was the top layer, aluminum the bottom layer and an elastomer interlayer in between. Pores could be detected on the right side in the elastomer interlayer. The dimensions, form and exact position within the laminate could be determined using the pore analysis in figure 5.3.

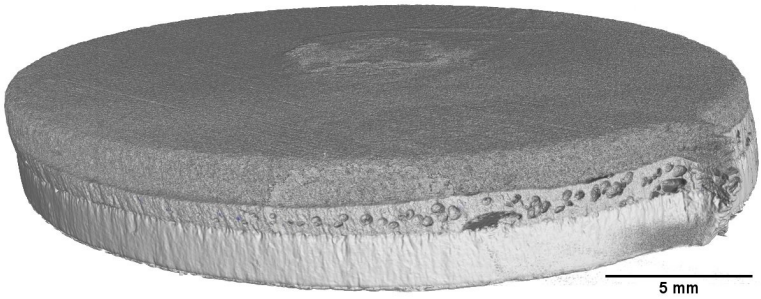

Figure 5.2: 3D CT specimen with a CFRP top layer, elastomer interlayer and aluminum bottom layer manufactured at 5 bar

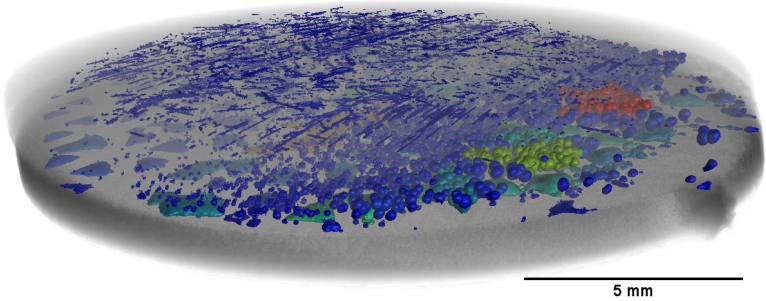

Figure 5.3: Colored pores after the manufacturing process with 5 bar in a 3D CT-scan image

Figure 5.3 shows the identical specimen and orientation as figure 5.2, but with faded out constituents and colored pores. The color of the pores was dependent on the volume indicating small defects in blue and large pores red. Long, thin pores within the top CFRP layer were visible in longitudinal and transversal direction. The long and thin pores were confined to the CFRP. Additional pores were found in the elastomer interlayer, which were globular and also confined to the layer.

Lastly, flat pores were found in the interface between the elastomer and aluminum layer, which had a flat triangular shape and were oriented in a hexagon. The edges of figure 5.3 seem defect free, but pores connected to the surface could not be visualized. The majority of pores seemed to be situated in the center of the specimen, however, the hexagonal and CFRP pores were homogeneously distributed. The pores within the elastomer layer were selected and presented in figure 5.4.

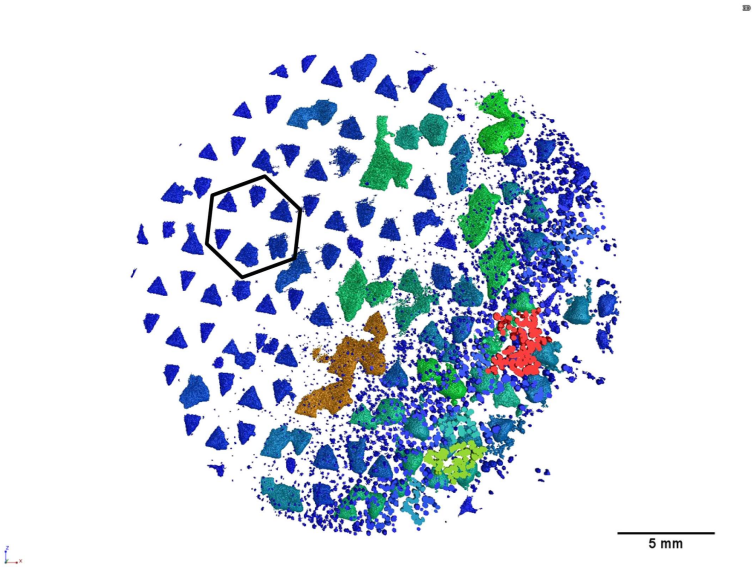

Figure 5.4: Colored pores after the manufacturing process with 5 bar in a CT-scan image with a marked hexagon

Figure 5.4 presents the globular and triangular pores in the elastomer layer, which were oriented in the hexagonal shape exemplary marked in the image. The globular pores exist in the lower right section of the image. The whole specimen shows the hexagonal structure made from triangles, which was already seen on the elastomer surface in image 5.1.

Additionally to the pore analysis, laminates without pores manufactured using different process parameters were visualized using cross-section polishes to show the topology of the interfaces. The five-layer laminate presented in figure 5.5 shows an interface between the CFRP constituent and the elastomer layer with a high roughness. The surface of the aluminum caused a flat interface to the elastomer. The layers were homogeneous in thickness over the specimen, even the unidirectional CFRP layers showed only minor variation within the biaxial CFRP layer.

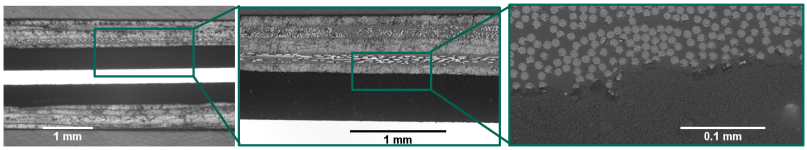

Figure 5.5: Cross-section polish of FMEL to visualize the interfaces

5.1.2 Process influence on the mechanical properties

The process variation conducted at the Institute for Production Science (wbk) varied the curing temperature and pressure. The influence of these variations on the mechanical performance of the laminate was analyzed using edge shear and bending tests accompanied with thickness measurements.

Figure 5.6 shows the results of the edge shear test, which was used to examine the quality of the interface depending on the process parameters. The specimen name contains QI, which represents the quasi-isotropic CFRP layup, followed by the manufacturing pressure and temperature. The variation of the manufacturing temperature from 130 °C to 140 °C increased the interfacial properties of the laminate in shear strength and shear energy. A higher temperature of 150 °C resulted in further enhanced interfacial properties. The highest temperature was beneficial for the interfacial properties.

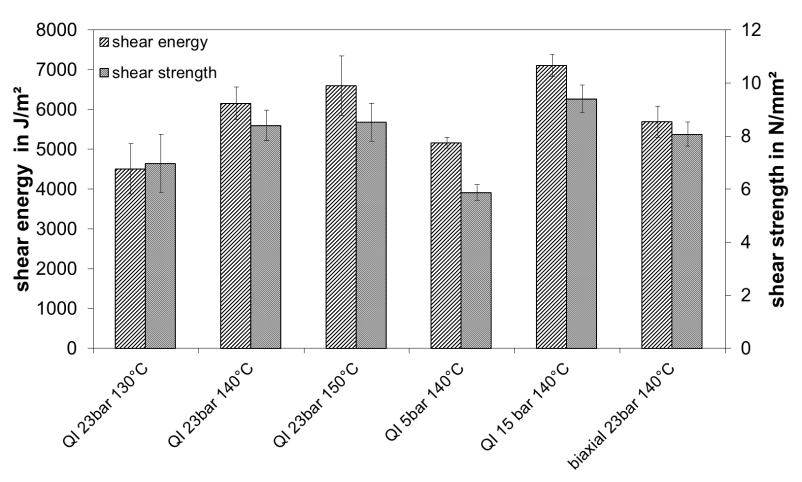

Figure 5.6: Edge shear properties of FMEL manufactured using different curing temperatures and pressures for a quasi-isotropic layup (QI) and a biaxial layup at 23 bar and 140 °C

The process pressure of 5 bar resulted in lower properties compared to the 23 bar, while 15 bar resulted in slightly higher properties. The minimum manufacturing pressure of 5 bar defined by the manufacturers' data sheets [132, 133] was found insufficient for good interfacial properties. The intermediate 15 bar pressure resulted in good interfacial properties.
The biaxial layup of the CFRP resulted in a minor decrease of interfacial properties. Additionally to the interfacial characterization the flexural properties were analyzed to determine the quality of the curing in the CFRP.

The flexural properties of the laminates presented in figure 5.7 show little variation of the strength depending on the process parameters. However, there was a tendency showing decreasing properties with increasing manufacturing temperature. The pressure of 5 bar continued the decreasing trend, but the 15 bar pressure resulted in nearly identical properties as the 23 bar specimens. The biaxial layup, which had a higher orientation, resulted in

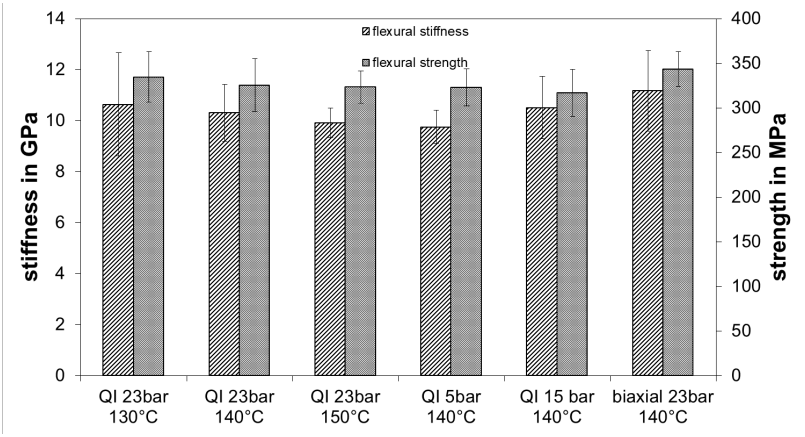

Figure 5.7: Flexural properties of FMEL using different process parameters

minor increase in properties. The high mechanical properties of the CFRP face layers resulted in comparable results for all laminates, which reduced the impact of the manufacturing process.

5.1.3 Validation of the cycle time optimization

The commercial process route for fiber-metal-laminates used hand lay-up and infiltration by autoclave, which resulted in high process cycle times of more than 3 h [121]. The comparably fast curing cycle of the laminate resulted in a duration of 300 s caused by the vulcanization of the elastomer [132]. This curing cycle was reduced further by the steps visualized in figure 5.8.

The process cycle time was reduced by partly curing the FMEL in the machine press under a pressure of 23 bar at 150 °C, but only for a certain percentile of the 300 s process cycle time. The laminates were then demolded and subsequently cured at elevated temperature without pressure to obtain the full 300 s curing cycle duration.

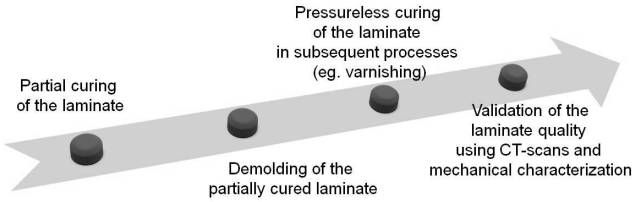

Figure 5.8: Procedure for reducing the curing cycle time for FMEL

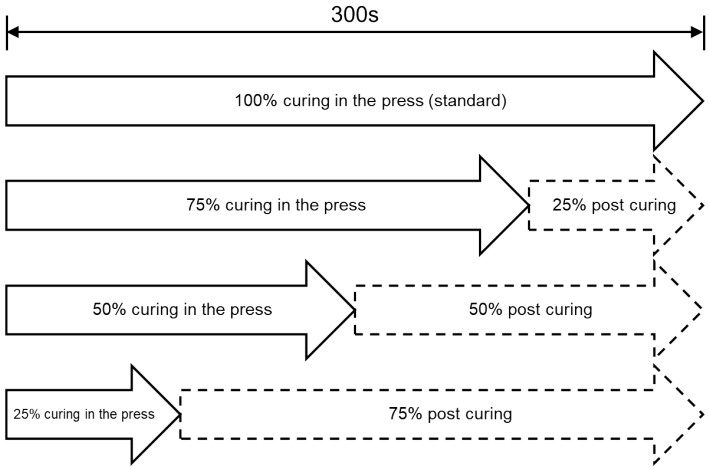

Figure 5.9: The process cycles for the laminates divided by curing in the press and post curing in an oven

The variations of the curing process are visualized in figure 5.9, where the standard process on the top cured the laminate for 300 s in the press to obtain the laminate. The first cycle time reduction led to curing in the press for 225 s and post curing without pressure at 150 °C for 75 s meeting the total cycle time duration of 300 s. Additionally, the curing time in the press was reduced to 150 s and 75 s, while the post curing time increased to fulfill the total curing cycle.

The post curing allowed the second part of the manufacturing process to be conducted within a different environment. When exemplary manufacturing an automobile, the FMEL could be cured in the press for 150 s and added to the body in white. Subsequent manufacturing steps of the automobile process may require elevated temperatures like the cataphoretic painting. The post-curing of the FMEL could be integrated in to the existing process, therefore, only the press curing cycle time would count towards the process cycle time.

Figure 5.10: FMEL after 25 % correlating with 75 s of the curing cycle in the press

Figure 5.10 presents the laminate after 25 % of the curing cycle in the press and 75 % post curing. The mechanical properties of the laminate could not be examined, because the structural integrity of the laminate was not achieved. The laminates manufactured for 150 s and 225 s in the press with subsequent post curing did not show external flaws like visualized in figure 5.10 and were tested in bending experiments to define the manufacturing quality especially of the CFRP.

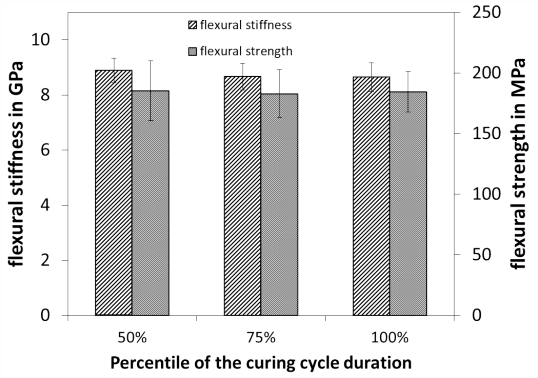

Figure 5.11: Mechanical properties of the FMEL with reduced curing cycle times

The mechanical properties of the laminates presented in figure 5.11, which were cured for 150 s or 50 % of the curing cycle in the machine press, did not vary from the properties of the fully cured laminates. The laminates manufactured for 225 s or 75 % in the press also showed identical performance compared to the conventionally manufactured laminates. The scattering increased with decreasing curing cycle time in the press.

5.1.4 Discussion of the process dependent properties

Process influence on the inner structure The manufacturing process with unsuitable parameters, in this case a low pressure of 5 bar, introduced pores into the laminates. The pores, which were detected in x-ray images as presented in figure 5.1 could be linked to the pattern of the pre-cured elastomer. The pattern was found on the aluminum layer after delamination in figure 5.1 indicating the connection. Figure 5.4 shows the pores in the specimen had clearly the identical pattern as the uncured elastomer layer. The pores caused by stacking of the layers could not be collapsed at 5 bar and remained in the laminate resulting in insufficient laminate quality.

The interfacial properties of the laminate produced at 5 bar was low caused by the pores in the laminate, while the flexural properties were comparably good due to the intact CFRP layer and the fiber dominated behavior. The flexural properties were high, as the interface did not fail prematurely, and the fibers in the outer layers carried the majority of the load. The interfacial properties, however, were lower especially in shear energy. The pores in the interface caused premature failure resulting in lower mechanical properties. The interface, being the weak link in laminates, is generally a critical point and reductions of the interfacial properties need to be prevented.
The interfacial properties of the elastomer CFRP interface was assessed with cross-section polishes. It was defined through a high roughness, whereas the interface between the elastomer and aluminum layer was smooth. A high roughness increased the mechanical properties of interfaces as it was stated for different constituents by Lucchetta et al. [27]. The high roughness resulted in mechanical interlocking, which increased the shear strength by 33 % when the areal roughness was increased from 2 μm to 6 μm. Also showed the Kraibon elastomer examined by Sarlin et al. high interfacial properties with GFRP and steel, where the laminate presented cohesive failure indicating very good adhesive properties [40].

Process influence on the mechanical properties The influence of the process on the interfacial properties was clearly detectable. The interfacial properties of the laminate increased with increasing temperature. The shear strength was increased by 22 % and the shear energy was 46 % higher. The highest temperature of 150 °C caused the lowest viscosity of the polymers and therefore the best coating of the neighbor constituent. The high interfacial roughness presented by the cross-section images and the research by Lucchetta et al. [27], which showed that the polymer had to fully coat the surface, resulted in beneficial properties due to low viscosity. The highest process temperature was correlated with the shortest cycle times, which enabled high productivity with the lowest estimated production costs.

A reduction of curing pressure to 5 bar led to pores, which was already discussed. The weakened interface was unacceptable and the process parameters had to be adapted accordingly. The intermediate pressure of 15 bar led to satisfactory interfacial properties without pores. However, to ensure reproducibility and a stable process, a safety factor of 1.5 was applied setting the manufacturing pressure to 23 bar assuring the high quality.
The quasi-isotropic layup of the laminate guarantees homogeneous properties in the layer also including the CTE. A homogeneous stiffness and CTE reduced the stresses after cooling from process temperatures. However, high mechanical properties benefit from the biaxial layup and are generally used in GLARE [20]. The interfacial properties, although reduced, were sufficient to select the biaxial CFRP layer. The mechanical performance of the laminate could be increased using a higher orientation in the CFRP layers as presented by Kawai et al. abiding the possibilities within the rule of mixtures [122]. The flexural properties of the laminates did not show process dependent variations. The carbon fibers in the face layers carried the majority of the load and therefore overshadowed the process dependent properties of the elastomer and epoxy. However, a slight increase of 6 % in strength and 20 % in stiffness was shown for the biaxial laminate. The effect was caused by the fiber orientation and not by the manufacturing process. The process parameters were defined by the interfacial properties, which showed a stronger dependency on the parameters. The interfacial strength was increased by 22 % and the energy by 46 % through the increase of manufacturing temperature from 130 °C to 150 °C.

Validation of the cycle time optimization The manufacturing of the hybrid laminates in this study was different from commercial and other research laminates. The manufacturing process using hot pressing enabled a fast curing resin, but limited the structure size compared to the large GLARE structures, which can be 34 m long. The curing cycle time was reduced and could be farther optimized by partly curing the laminate with subsequent

tempering without pressure. The process in the press was favorable, because low cycle times could guarantee high component quantities.
The co-curing of the elastomer interlayer and the matrix of the FRP component in the press already reduced the process cycle time by 140 s compared to individually curing the components. The CFRP curing was integrated in the vulcanization step of the elastomer, thus saving the process cycle time of the CFRP layers. The use of fast curing components led to a low cycle time compared to the autoclave process. The process cycle for FMEL was conducted in 300 s, which is significantly lower compared to the GLARE cycle time of over 3 hours [121]. The high conventional curing cycle time is largely affected by long heating and cooling cycles of the autoclave [17].
The cycle time was reduced further by partly curing the laminate with subsequent pressureless tempering. The subsequent process could be integrated in process steps neccessary for the application of FMEL, which would generally be conducted at high temperatures like varnishing. The laminate manufactured in the press for 25 % of the cycle time resulted in non-consolidated CFRP. According to the data sheet, the CFRP should be fully cured after 120 s [133], so the cycle time of 75 s expectedly did not fully cure the epoxy. A full consolidation could not have been achieved by 75 s, but a high viscosity would have had sufficed for the subsequent post-curing step. However, the results showed insufficient viscosity for demolding.
The higher cycle time percentiles of 50 % and 75 %, which corresponded with cycle times in the press of 150 s and 225 s, resulted in consolidated FMEL. The resulting flexural properties of the laminates were identical to the FMEL manufactured fully in the press, while the scattering slightly increased with shorter cycle times in the press. The laminate was cured in the press sufficiently to collapse pores and obtain a high viscosity of the laminate to keep the structural integrity throughout the demolding and handling process to generate a laminate with good mechanical properties. Therefore the cycle time of FMEL could be reduced by 50 % to 150 s, which reduced the manufacturing costs and increased production quantity.

5.2 Interface characterization

As aforementioned, the interface of the laminate can be the weak link of the structure. A thorough characterization is necessary to describe the interfacial behavior and prevent premature failure. FML and FMEL specimens were compared to evaluate the interfacial properties and understand the influence of the elastomer interlayer.

5.2.1 Mechanical characterization of the interface

The mechanical properties of the interface were characterized using the shear edge test. The characteristic values were the shear strength, the maximum shear load applicable to the laminate and the shear energy, the energy absorbed until failure, which did not only amount to the maximum load, but also the ductility of the interface.

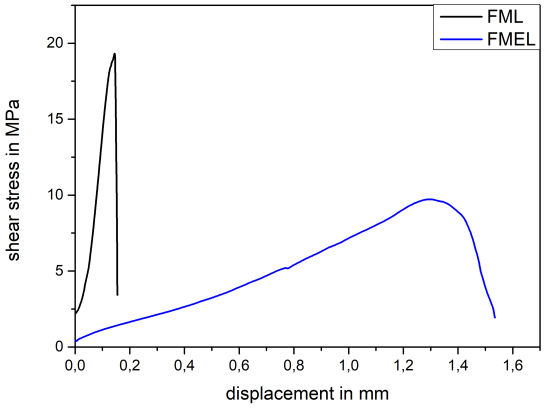

Figure 5.12: Stress-displacement curves of FML and FMEL in the edge shear test [147]

The stress-displacement curves of the edge shear test presented in figure 5.12 show different behavior of the laminates. The FML visualized in black showed high shear strengths and low displacement values in figure 5.12. The FMEL presented by the blue line in figure 5.12 did not exhibit the high strength of the FML, but higher displacement values. The interfacial stiffness of the FMEL was also significantly lower. The FML showed brittle fracture as represented by a sharp stress decrease, while the FMEL showed ductile fracture shown by the gradual stress decrease after reaching the shear strength. The shear energy, which is represented by the area under the stress-strain curve, was calculated and used to compare the laminates' performance apart from the shear strength.

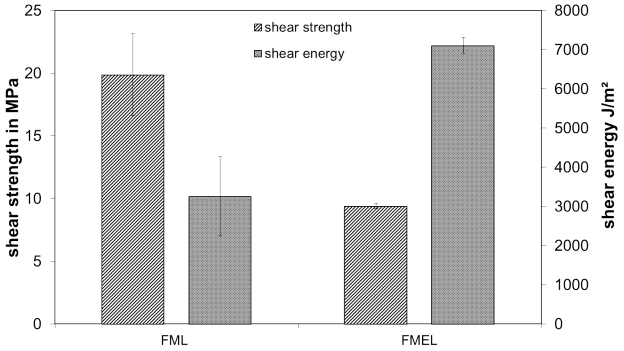

Figure 5.13: Interfacial properties of FML and FMEL [147]

Figure 5.13 shows the interfacial properties of FML in comparison to the FMEL. The FML shows high shear strength and a low shear energy. The elastomer interlayer in the FMEL reduced the strength, but increased the shear energy. The scattering of the FML was also significantly reduced by the elastomer interlayer.

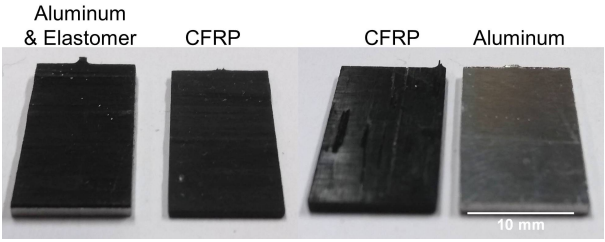

Figure 5.14: Fractured interfaces of FMEL (left) and FML (right) after the edge shear test

The fracture of the FMEL specimens in the edge shear test was in the elastomer-CFRP interface as presented in figure 5.14 on the left side. The crack propagated in the interface separating the constituents and indicating the aluminum elastomer interface to have a higher strength. The failure was purely adhesive in the CFRP elastomer interface and no cohesive failure could be detected. The FML shown in figure 5.14 on the right exhibited interfacial failure between the aluminum and CFRP layer. The blank aluminum surface clearly shows the adhesive failure of the laminate. Both specimens were separated through the interfaces, separating the CFRP from the elastomer in the FMEL and the CFRP from the aluminum in the FML, and no residual constituent adhered to the other side.

5.2.2 Discussion of interface properties

The interfacial properties of FMEL and FML were assessed to describe the impact of the elastomer interlayer as well as the properties of both laminates to detect and prevent premature failure. The elastomer interlayer altered the interface by changing the failure from brittle separation to ductile fracture and interfacial crack propagation instead of spontaneous delamination. The displacement between the shear strength and failure in figure 5.12 visualizes the crack propagation through the interface.

This accounts for a beneficial failure mode of the FMEL. After the strength, the laminate still had structural integrity and decreasing load bearing capability. The FML exhibited brittle and sudden failure at high strengths doubling the value of FMEL, but a critical failure mechanism. The interfacial stiffness of the FML was significantly higher, which benefited the load bearing capability but hindered large deformations. The over 600 % higher displacement of the FMEL was beneficial in strain induced failure, but resulted in lower strength.

The shear energy of the FML was low due to the low displacement and sudden failure. The high scatter in strength of 16 % led to a high scatter in energy of 31 %. The brittle interface of the FML did not absorb as much energy as the ductile FMEL interface, which was $3260\,\mathrm{J/m^2}$ compared to $7108\,\mathrm{J/m^2}$. The 1.55 mm displacement of the FMEL specimens resulted in high shear energies compared to the 0.18 mm displacement of the FML. The gradual fracture increased the high energy absorption further. Interfacial properties of FML obtained with ILSS showed 38 MPa shear strength of FML, but may have included a bending component, which led to an overestimation of the interfacial properties [37].

The crack in the FMEL propagated in the interface of the CFRP and elastomer layer, which was found to be the more critical interface of the laminate. The failure did not occur spontaneous, but the crack propagated along the interface, as figure 5.12 already indicated. The FML also showed adhesive failure. The interface therefore presented lower mechanical properties compared to the interlaminar CFRP properties, because the crack did not propagate through the CFRP. Additionally was the cohesive strength of the elastomer not exceeded in the FMEL. Sarlin et al. [52] found cohesive failure in Kraibon, a failure mechanism, which indicated better interfacial properties in the laminate, where the elastomer was paired with steel and GFRP. In FMEL and FML the interface presented itself as the weak link, because the mechanical properties of the constituents did not define failure.

5.3 Characterization of quasi-static properties

Materials are mostly compared using quasi-static properties, like Young's Modulus, yield or tensile strength. The quasi static mechanical properties were used to compare the laminate with bulk materials. The laminate stiffness and strength could be predicted using the Voigt and Reuß theorem as well as the classical laminate theory to validate the theoretical results with experiments. The data fed into the models was taken from the manufacturers' data sheets for the single constituents [129, 130, 131].

5.3.1 Tensile properties

The tensile properties of the laminates and constituents are presented in figure 5.15. The laminate properties were dominated by the CFRP behavior and resulted in a brittle behavior of the laminate. The behavior of the constituents in the laminate is also depicted in figure 5.15, where the longitudinal and transversal properties of the single CFRP layers were examined.

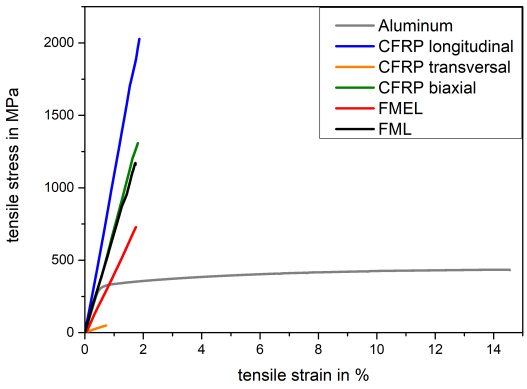

Figure 5.15: Stress-strain curves of the constituents of FML

The only ductile behavior was presented by the aluminum layer with 14.5 % strain to failure. The biaxial CFRP had 1.8 % strain to failure, which was nearly identical with FMEL, FML and longitudinal CFRP. Only the transversal CFRP exhibited a more brittle behavior at 0.7 % strain. The strain to failure of the laminates correlated with the biaxial CFRP, which therefore defined the failure criterion in tension and the ductility of the aluminum was overshadowed.

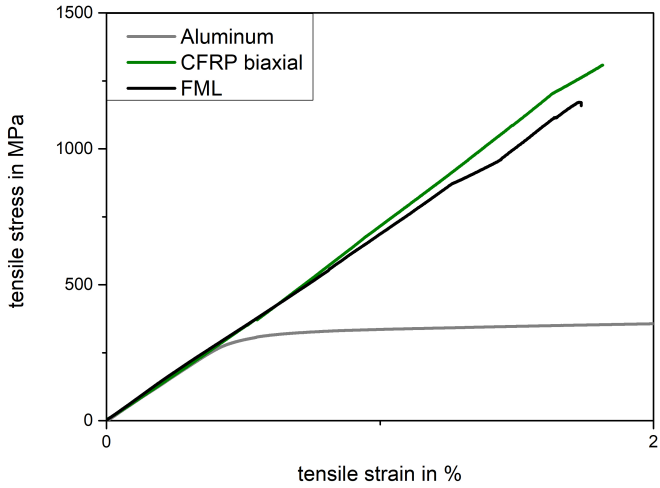

Figure 5.16: Stress-strain curves for aluminum, biaxial CFRP and FML

The aluminum, biaxial CFRP and FML possessed a similar stiffness as presented in figure 5.16. The CFRP stiffness was deduced from the unidirectional layers. The longitudinal CFRP layer had a very high stiffness of 99.5 GPa ±4.0 GPa, due to the fiber orientation. The transversal layer had the lowest stiffness of 6.6 GPa ±0.5 GPa, resulting in an intermediate stiffness for the biaxial layer at 69.6 GPa ±3.5 GPa.

The FML, consisting of biaxial CFRP and aluminum, had the nearly identical stiffness of 68.8 GPa ±2.4 GPa compared to both constituents.
The FMEL had a reduced stiffness of 43.8 GPa ±2.1 GPa caused by the low stiffness of the elastomer. The strength of the aluminum layer was at 433 MPa ±6 MPa significantly lower than the biaxial CFRP strength of approximately 1300 MPa ±87 MPa. The unidirectional CFRP layers had the extreme strength values at 2000 MPa ±130 MPa and 51 MPa ±18 MPa dependent on the fiber direction, while the FML with 1107 MPa ±103 MPa and FMEL with 712 MPa ±33 MPa only surpassed aluminum in strength.
The elastomer interlayer was not presented in figure 5.15 due to drastically different mechanical properties. The stress-strain curve for the elastomer is shown in figure 5.17.

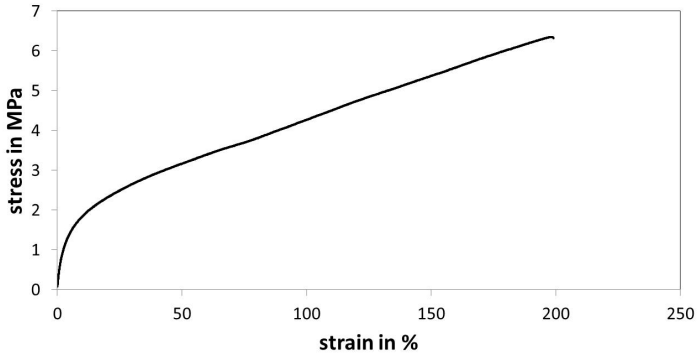

Figure 5.17: Tension stress-strain curve for elastomer layer

The elastomer layer has a comparably low Young's Modulus with 50 MPa. The strength was 7.8 MPa ±1.4 MPa and the strain to failure 200 % ±2.1 %. The elastomer exhibited a very ductile behavior without high stress levels. The elastomer was, compared to the CFRP and aluminum, a very soft material with an extremely high strain to failure.

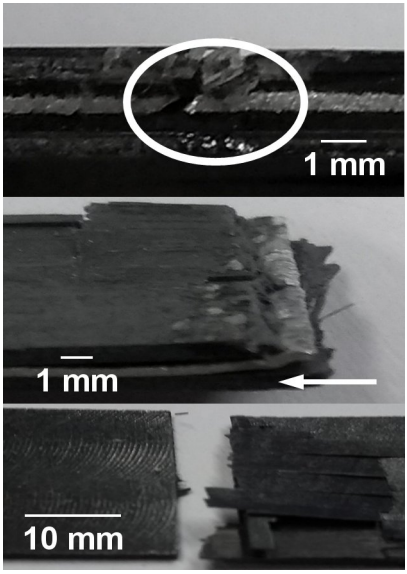

Figure 5.18: Fractured FMEL (left), FML (middle) and CFRP (right) after tensile tests

The failure in FMEL in figure 5.18 on the top shows fracture in the CFRP and aluminum constituents, but the intact elastomer layer and interfaces prevented specimen separation. The FML in the central image showed also CFRP and aluminum fracture, but was separated into two segments. Additionally, there was delamination between the constituents, which is marked with an arrow in the image. The CFRP layer on the bottom showed delamination and specimen separation. The ductile aluminum properties were not exhibited by the laminates, as the laminates showed brittle failure caused by the CFRP layer.

The properties of the single CFRP layers in longitudinal and transversal direction, the biaxial CFRP layer as well as both laminates are presented in table 5.1. The theoretical values for the stiffness were calculated using the Voigt and Reuß theorem according to equation 2.1 and 2.2.

The transversal layer was calculated using the Reuß equation with the material properties from the CFRP data sheet [129]. The longitudinal properties were calculated using the Voigt equation. The subsequent biaxial, FML and FMEL properties were also calculated using the Voigt equation. The calculation for the biaxial layer used the results of the transverse and longitudinal layer. The input data for the FMEL was the result of the biaxial layer as well as elastomer and aluminum data sheet properties [130, 131].
The theoretical strength was calculated using the classical laminate theory in the software *eLamX*^{2}. The data used for the calculations was taken from the data sheets to form a model which was paired with the failure criterion by Puck [54]. All models in the software were built using the mechanical properties of the single constituent layers taken from the data sheets [129, 130, 131].

Table 5.1: Theoretical and experimental tensile CFRP and laminate properties

Orientation	theoretical stiffness	experimental stiffness	theoretical strength	experimental strength
longitudinal CFRP	116.7 GPa	99.5 GPa ±4.0 GPa	2250 MPa	2000 MPa ±130 MPa
transversal CFRP	7 GPa	6.6 GPa ±0.5 GPa	90 MPa	51 MPa ±18 MPa
biaxial CFRP	80 GPa	69.6 GPa ±3.5 GPa	1500 MPa	1300 MPa ±87 MPa
FML	79.1 GPa	68.8 GPa ±2.4 GPa	1287 MPa	1107 MPa ±103 MPa
FMEL	47.6 GPa	43.8 GPa ±2.1 GPa	720 MPa	712 MPa ±33 MPa

The theoretically calculated stiffness and strength values were not reached in the experiment by any of the materials. The variation from the experiments was acceptable and could represent the mechanical properties of all laminates. The longitudinal and transversal properties of the CFRP to form the biaxial CFRP are visualized in the table 5.1. The theoretical and experimental stiffness of the biaxial CFRP was nearly identical with the 73 GPa of the aluminum resulting in a nearly identical stiffness of the FML. The FML had a higher stiffness than the FMEL caused by the low load bearing capability of the elastomer.

5.3.2 Compressive properties

The compressive properties of the laminate were examined to analyze whether the CFRP would exhibit micro-buckling of the fibers resulting in premature failure. Additionally, the layers itself were comparably thin bearing the danger of buckling.

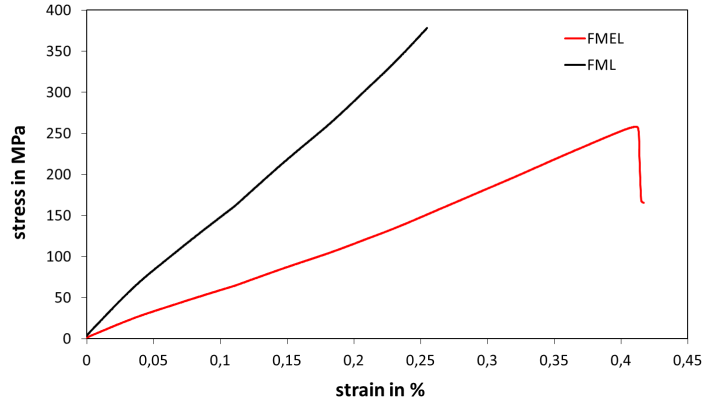

Figure 5.19: Compressive properties of FMEL

The results presented in figure 5.19 show compressive properties of FML and FMEL. The compressive properties of FMEL were 247 MPa ±34 MPa in strength, while the strength of FML was higher at 367 MPa ±76 MPa. The strain to failure of FMEL was 0.41 % and the FML had 0.26 %. Both laminates showed brittle fractures with sharp stress drops after the strength was met.

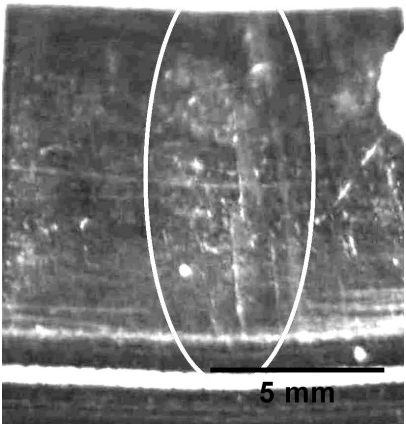

Figure 5.20: Compressive failure of FMEL with macro-buckling and CFRP buckling (encircled)

Figure 5.20 presents the failed FMEL specimen. The aluminum cap strips are visible on the CFRP layer. The image shows buckling of the whole specimen and compression failure of the CFRP top layer. The failure of the FML was identical and no delamination was found in either laminate.

5.3.3 Flexural properties

The flexural properties of the laminate were of importance, because bending was the expected near-service load for the laminates and the laminates were selected concerning optimum flexural properties in chapter 3.

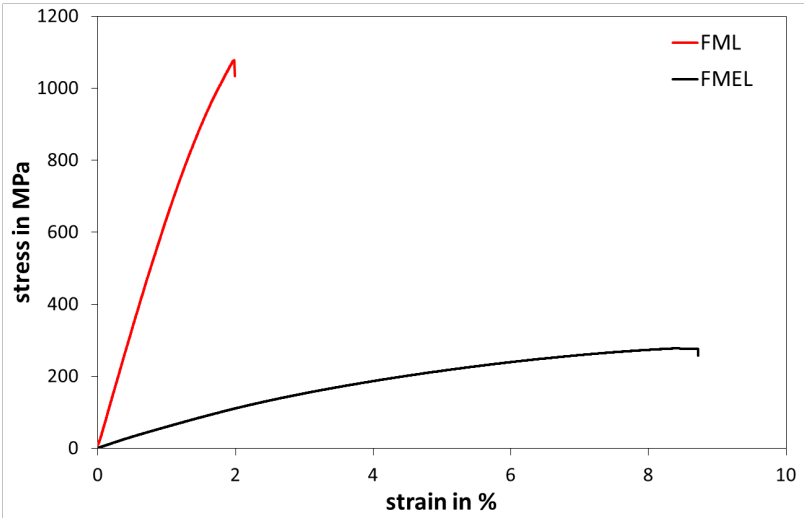

Figure 5.21: Flexural stress strain curve for FMEL and FML

Figure 5.21 shows a stress strain curve for an FML and FMEL in a flexural experiment. The FML exhibited a high stiffness of 46.6 GPa ±18 GPa and strength of 802 MPa ±240 MPa, but with 2.31 % ±0.38 % a low strain to failure. The FMEL showed a lower stiffness of 21.0 GPa ±1.0 GPa and strength of 308 MPa ±14 MPa, but with 9.1 % ±0.35 % higher strains to failure. The FML presented brittle behavior, while the behavior of FMEL had high strains but also exhibited a sharp stress drop after the strength was met. However, the failure mechanism of the laminates showed significant differences.

The FML specimen failed due to delamination of the constituents as shown on the left side of figure 5.22. Bending loaded the interface in shear, which caused the specimens to delaminate and fail spontaneously. The FMEL failure mechanism was tension failure in the outer fiber. The failed specimen is depicted in figure 5.22 on the right side.

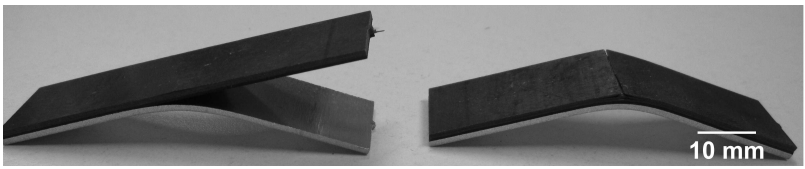

Figure 5.22: Delamination in FML (left) and tension failure in FMEL (right) caused by bending loads

5.3.4 Crack propagation properties

The crack propagation behavior was experimentally obtained by double cantilever beam (DCB) tests. Cracks can generally propagate in different directions; however, the interfacial crack propagation rate was determined as the most crucial. The interface can be the weak link in laminates, which can increase crack propagation rates and result in premature failure. The interfacial properties were assessed through the energy release rate.

Figure 5.23 shows the force-displacement relation of cracks in FMEL and FML propagating in the interface. The maximum force for the interfacial crack in FMEL to propagate was approximately 35 N and declined with increasing crack length. The maximum force for FML was approximately 25 N remaining nearly constant throughout the experiment. While the curve was obtained, the crack length was measured to obtain G_{Ic}.
FMEL: $G_{Ic} = 296.9 \pm 50.1 \quad J/m^2$
FML: $G_{Ic} = 204.8 \pm 53.9 \quad J/m^2$

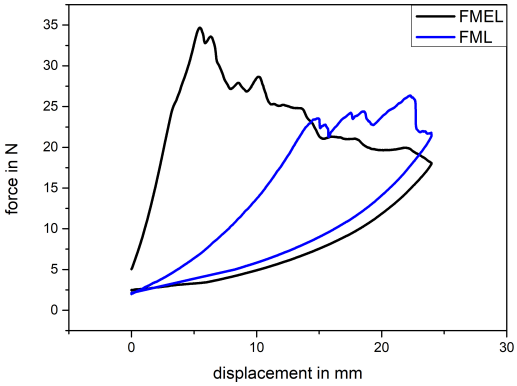

Figure 5.23: Force-displacement curves of FMEL and FML in double cantilever beam experiments

The energy release rate for the FMEL was higher compared to the FML caused by higher forces during the experiment.

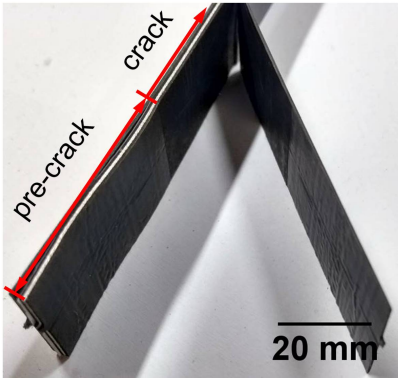

Figure 5.24: FMEL DCB specimen with a pre-crack of 50 mm and a failed CFRP elastomer interface

Figure 5.24 presents the failed FMEL specimen, where the pre-crack left glossy surfaces on the elastomer and CFRP. The subsequent crack in the DCB experiment resulted in dull surfaces of the constituents. The crack propagated in the elastomer CFRP interface of the specimen and generated a fully adhesive failure. The FML specimen, however, showed different behavior in the DCB test.

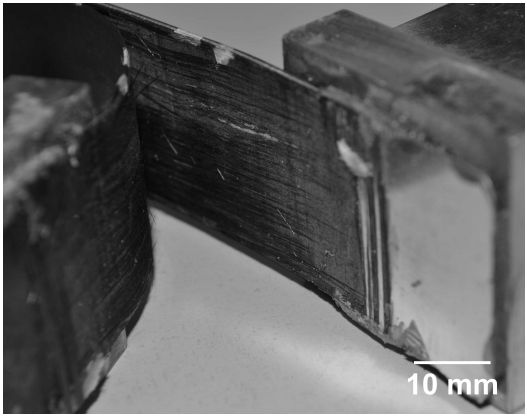

Figure 5.25: FML DCB specimen with a pre-crack of 50 mm and a crack propagating through the CFRP layer

Figure 5.25 visualizes the crack growth of the FML DCB specimen. The pre-crack is visible through smooth surfaces with bare aluminum on the right and pure CFRP on the left. The crack propagation did not occur in the interface, but in the CFRP layer and propagated between the uni-directional CFRP layers. The crack through the CFRP is visualized by the CFRP on the aluminum layer on the right side of figure 5.25. The crack led to cohesive failure in the CFRP laminate.

5.3.5 Puncture properties

Puncture properties of the laminates were examined to describe the laminate and constituent behavior under near-service loads. Compared to the high speed puncture experiments resembling fast impacts, the slow impact reconstructed crash situations with low relative velocities. The quasi static tests were also used to gain information about the failure mechanisms and the strain distribution, which could not be visualized and analyzed in the dynamic puncture test.

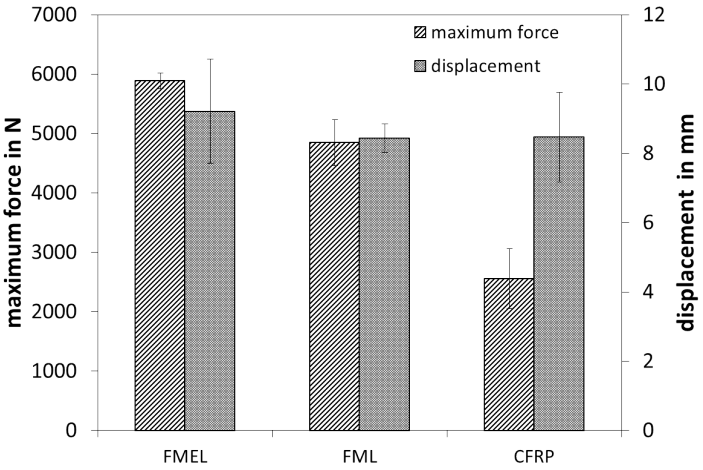

Figure 5.26: Mechanical properties of FMEL, FML and biaxial CFRP under puncture loads

Figure 5.26 shows the mechanical performance of FMEL compared to FML and biaxial CFRP. The FMEL failed with 5886 N $\pm$136 N at higher forces compared to the 4851 N $\pm$387 N of the FML. The CFRP showed lower mechanical properties of 2555 N $\pm$504 N. The scatter in penetration force was lower for the FMEL compared to the CFRP and FML.

The FML showed low displacement at 8.47 mm ±0.41 mm compared to the FMEL at 9.21 mm ±1.50 mm. The CFRP had the identical value as the FML with 8.47 mm ±1.3 mm, but higher scatter. The scatter of FMEL and CFRP were nearly identical, but the FML had lower scatter in displacement. The strain distribution in the puncture tests were analyzed using stereo DIC to measure out of plane displacement. The strain distribution of the laminates was inhomogeneous due to the difference in stiffness depending on the fiber orientation in the CFRP layer. The influence of the CFRP layer on the laminate's strain distribution was visible for the FMEL and FML specimens in figure 5.27 and 5.28.

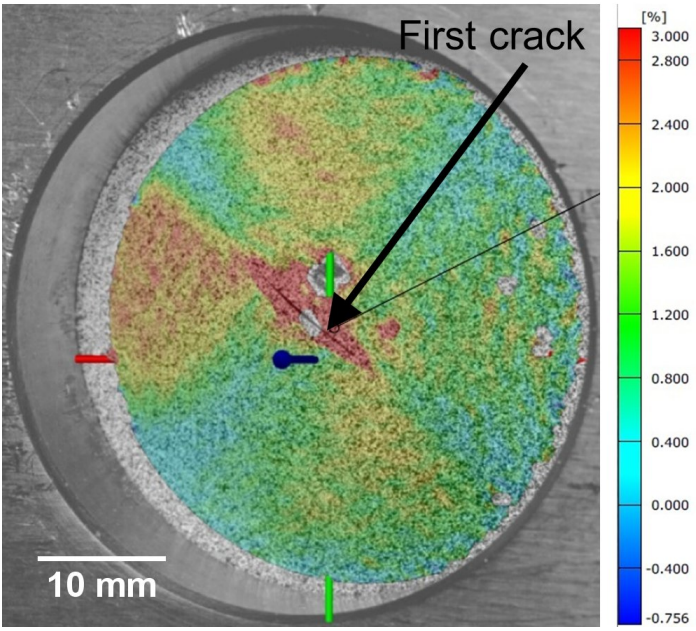

Figure 5.27: Strain distribution of CFRP in a puncture test shortly before failure

Figure 5.27 shows a characteristic strain distribution for a biaxial CFRP sheet. The strain in fiber direction, which was diagonally oriented and shown in light blue, was low due to the high fiber stiffness. The stiffness of the layer decreased with increasing angle from the fiber orientation due to the lower matrix stiffness. Therefore, the light blue indication of strains below 0.6 % increased to orange, which resembled approximately 2.3 % strain. The first crack directly opposite the penetrator was marked with an arrow and is situated in 90 ° to the fiber of the outer CFRP layer.
The pattern shown in figure 5.27 could also be found in figure 5.28, proving that the CFRP properties had a significant influence on the laminate strain distribution.

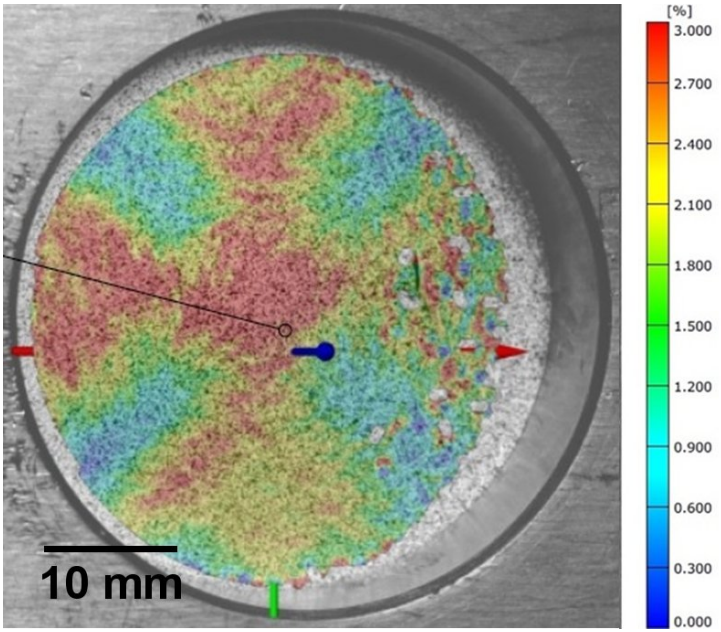

Figure 5.28: Puncture test on FMEL with DIC strain measurements

Figure 5.28 shows the strain distribution for an FMEL specimen, which has the same characteristic pattern as the CFRP specimen in figure 5.27. The FMEL and FML specimens had the identical behavior in the strain distribution. For the FMEL the highest strain values of 2.95 % were higher compared to the 2.2 % of the CFRP specimen. The fracture initiation was also perpendicular to the fiber direction in the face sheet for all laminates. An analysis, whether delamination occurred during the experiment, could not be conducted within the quasi-static penetration tests due to the specimen clamping in the experimental setup.
Hence, ex-situ CT-scan puncture test were used to detect delamination in the laminate and determine deflection exemplary in figure 5.31, which correlated with the strain distribution of the quasi-static puncture tests.

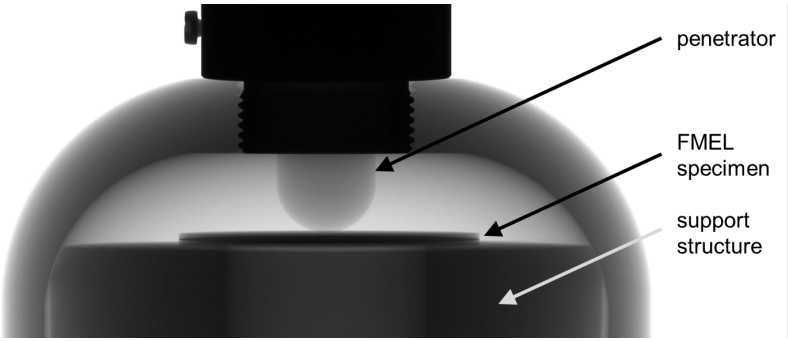

Figure 5.29: X-ray image of the CT puncture test setup with an FMEL specimen

Figure 5.29 shows the experimental setup for the ex-situ CT puncture tests, with marked penetrator and FMEL specimen. The surrounding structure was virtually removed to obtain the visual data of the specimen presented in figure 5.30.

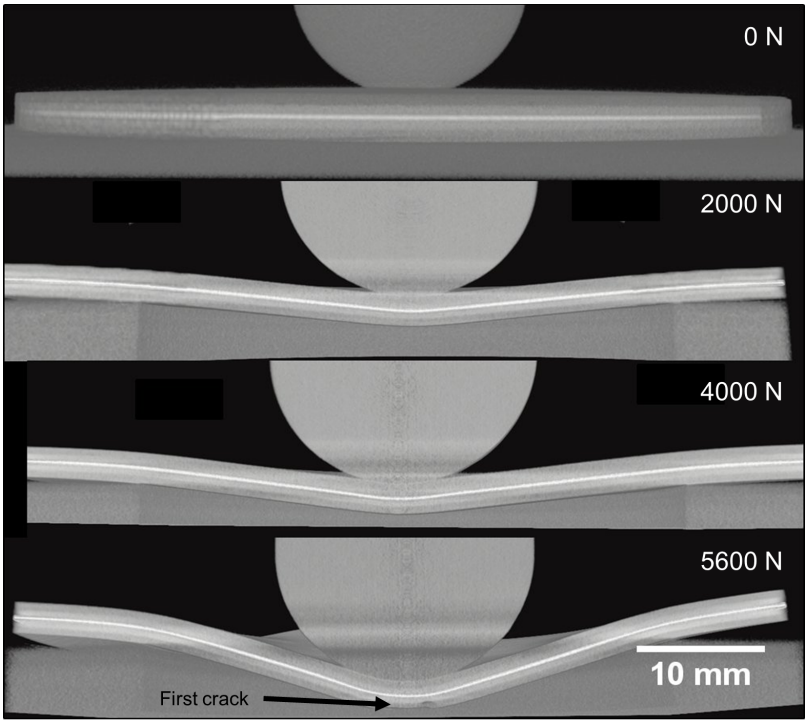

Figure 5.30: X-ray puncture image of an FMEL specimen at 0 N, 2000 N, 4000 N and 5600 N

Figure 5.30 presents a FMEL specimen in the in-situ CT penetration test at 0 N, 2000 N, 4000 N and 5600 N. The load increased from the top image over the central images to the bottom image. The penetrator, support structure and specimen were virtually cut to show the central deformation line of the laminate. The difference between the metal, CFRP and elastomer is visible in the CT image. The specimen shows elastic deformation under the load without indication of delamination. The first load level of 2000 N causes deformation in the second image. The second load level already exhibited a sharp bend opposite the penetrator at 4000 N in the third image and the laminate was only supported on the edge of the support structure. The fourth image shows cracking at 5600 N opposite the penetrator, marked with an arrow in the image, and the specimen showed upward deflection at the edges. The crack was better visualized in figure 5.32.

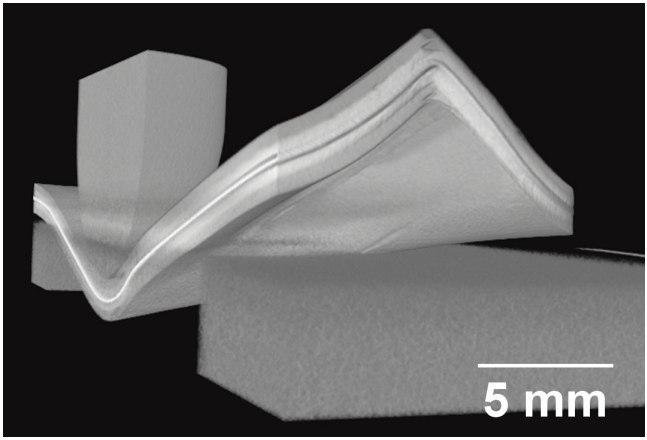

Figure 5.31: X-ray image of the CT puncture test setup with a wrinkled FMEL specimen

Figure 5.31 presents the deflection of the edge of the specimen, where the specimen was not clamped to the support structure. Also wrinkling was exhibited by the FMEL and the wrinkles of the specimen were identical to the fiber direction in the CFRP and could be detected four times per specimen. The strain distribution was highly asymmetric, as already seen in the DIC measurements.

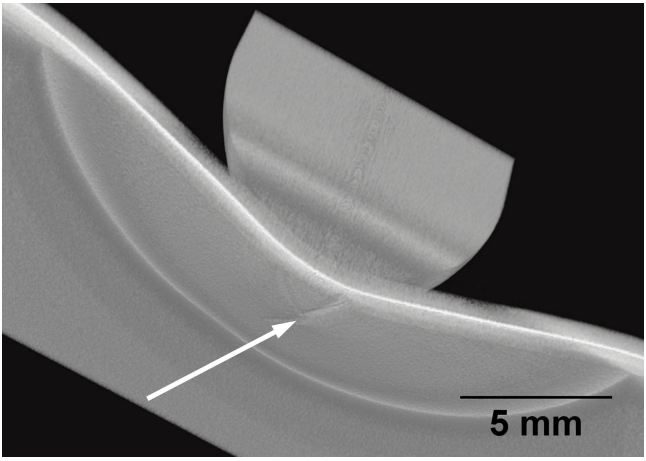

Figure 5.32: X-ray image of the CT puncture test setup with a cracked FMEL specimen

Figure 5.32 shows the laminate opposite the penetrator, where the first crack occurred. The crack, oriented perpendicular to the outer fiber orientation of the CFRP, existed only in the first unidirectional CFRP layer. The remaining layers of the laminate were still intact, although first failure was initiated at 95 % of the strength of the specimen. The failure was spontaneous after the strength was reached. Delamination could not be detected within the FMEL specimen.

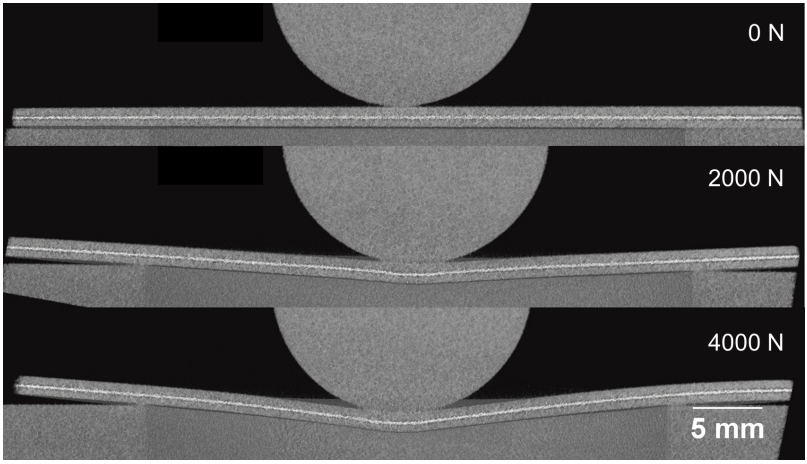

Figure 5.33: X-ray puncture image of an FML specimen at 0 N, 2000 N and 4000 N

Figure 5.33 presents the FML specimen in the CT penetration test. The unloaded specimen is shown in the top image, where the CFRP can be clearly distinguished from the aluminum layer. The central image shows the loaded FML specimen at 2000 N with an already sharp bend opposite the penetrator and upward deflection of the edges. The lowest image shows larger deflections of the laminate at 4000 N shortly before spontaneous failure occurred. The deflection was comparably low before failure, but the strain was high, which was indicated by the sharp bend opposite the penetrator. The FML failed at lower forces compared to the FMEL, therefore, the highest load presented in figure 5.30 could not be achieved. The high stiffness and low applied force resulted in low deflections in the FML presented in the CT images. Delamination could not be detected in the laminate. However, the FML did not wrinkle like the FMEL.

5.3.6 Environmental resistance

Materials are subject to environmental stress additionally to the mechanical loads in application. Changes in temperature or corrosive environments can cause damage to structures. The environmental stress tests were viewed as crucial experiments to determine the applicability of the laminate. The FML properties were expected to deteriorate from the CTE-mismatch and corrosive properties, whereas the elastomer interlayer was desired to solve these problems.
The damage to the laminate was evaluated by assessing the residual interfacial properties with the edge shear test, because the environmental stress was expected to directly affect the interface. The environmental conditions were simulated by thermal cycling, testing at elevated temperatures and neutral salt spray tests.

Interface properties after thermal cycling

The thermal cycling was carried out from $-40\,^{\circ}\mathrm{C}$ to $80\,^{\circ}\mathrm{C}$ to induce shear stress into the interface, which resulted from the CTE-mismatch. The stress could cause damage and even delamination. The residual properties after thermal loading were examined to define the damage to the laminate.

Figure 5.34 presents the curves for the edge shear experiments on FMEL and FML after thermal loads compared with virgin specimens. All FML had higher interfacial stiffness values than the FMEL specimens. However, the virgin black FML curve showed 26 % lower strength and strain values after 100 thermal cycles (blue). 1000 thermal cycles reduced the interfacial properties by 69 %, which is visualized by the lower red curve compared to the blue curve.
The FMEL exhibited the characteristic 9.4 MPa strength and $7108\,\mathrm{J/m^2}$ energy, which remained constant with virgin specimens (black), after 100 (blue) and 1000 (red) thermal cycles. The high energy was retained as well as the interfacial strength.

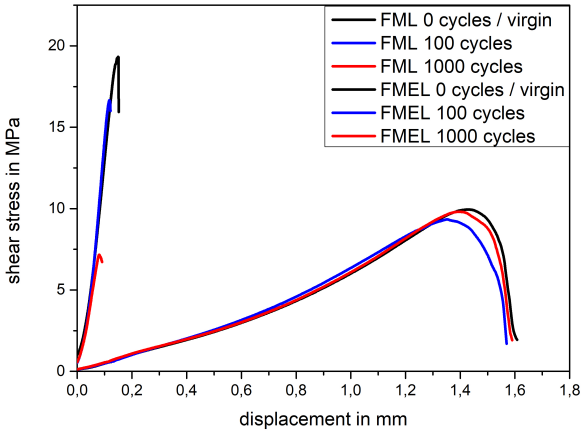

Figure 5.34: Virgin versus thermally cycled FML and FMEL edge shear curves

The stiffness of both laminates remained constant invariant of the environmental load prior to testing. The aforementioned high shear energy of the FMEL and high strength of the FML are visible in the virgin properties. The scattering of the FML properties was higher compared to the FMEL.
The results of the residual interfacial properties of FMEL after 100 and 1000 thermal cycles in figure 5.35 on the left side showed that with the integration of an elastomer interlayer the CTE-mismatch was fully absorbed and the mechanical properties remained constant throughout the thermal loads. Figure 5.35 showed on the right side the interfacial properties of FML after thermal cycling. The shear strength and shear energy were reduced due to the thermal cycling and did decrease further with increasing thermal cycles. The scattering relative to the average properties increased with increasing environmental load duration. The thermal cycles caused interfacial strength and energy decrease, which was prevented by the elastomer.

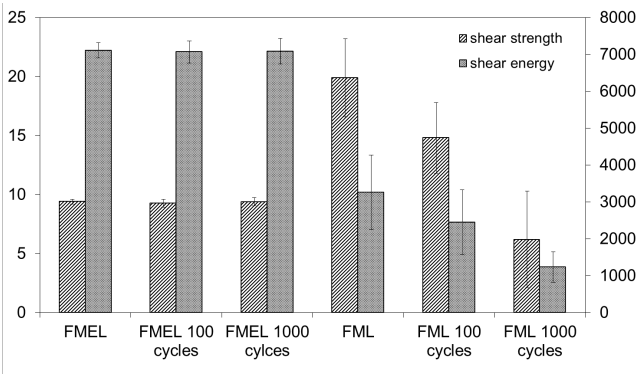

Figure 5.35: Interfacial properties of FMEL (left) and FML (right) after thermal cycling [148]

Interface properties after corrosion

The corrosion tests were carried out in a neutral salt spray environment. The effect of the electrolyte closing the electrical circuit would result in galvanic corrosion directly in the interface. The mechanical properties of the laminates after the salt spray were examined with edge shear experiments.

Figure 5.36 shows the curves obtained during the edge shear tests after different corrosive loads and compares them to virgin specimens. The FML possessed higher stiffness and strength in the virgin state. The strength was reduced drastically due to the corrosive load of 48 h, which is resembled by the blue curve compared to the black curve. The shear energy, the area under the curve was reduced accordingly. Figure 5.36 does not include a curve for the FML specimen after 96 h, because the specimens delaminated in the salt spray chamber without external force setting the residual properties to zero.

The FMEL specimens had characteristic high strain and shear energy values. The form of the curves did not change due to the corrosive load. There was no significant interfacial damage to the FMEL.

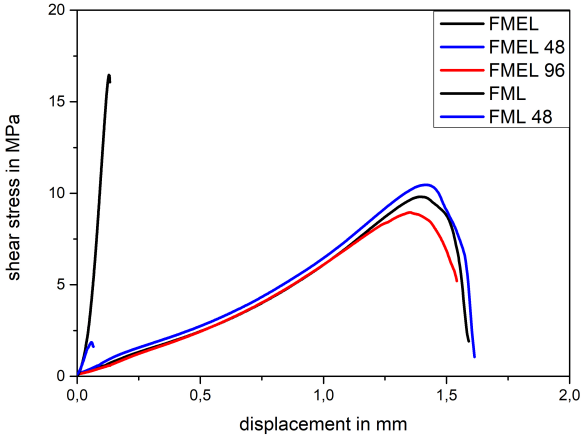

Figure 5.36: Force displacement curves of FML and FMEL after different salt spray durations

In figure 5.37 it is shown, that the FMEL properties were not affected by the neutral salt spray. The properties of the laminates remained nearly constant throughout the 48 h and 96 h exposure. The values of the shorter salt spray duration led to a minor increase in properties. The 96 h corrosive load caused a minor decrease in interfacial properties. The energy and strength had a lower average value with higher scattering. All specimens were intact after the salt spray test and did not show signs of damage due to galvanic corrosion.

The interfacial properties of the FML decreased drastically during the first 48 h of the corrosion test. The specimens in the salt spray for 96 h could not be tested, because failure due to delamination occurred in all specimens without any external force.

The FML specimens showed signs of corrosion after the neutral salt spray test, which are presented in figure 5.38.

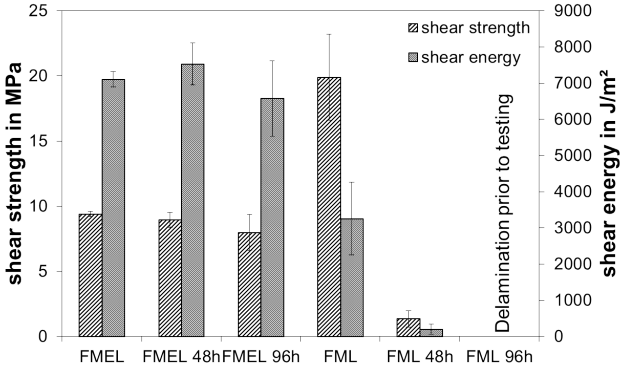

Figure 5.37: Interfacial properties of FMEL and FML after corrosive loads

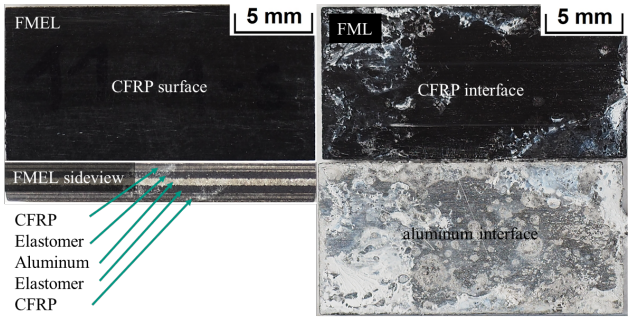

Figure 5.38: Corrosive damage to FMEL in top view and side view(left) and to FML, where the delaminated interface is shown (right) [149]

Figure 5.38 shows the laminates after a neutral salt spray test duration of 48 h. On the left side, there is an FMEL specimen, which shows no signs of interfacial corrosion. Little signs of corrosion can be seen in the side view, where white corrosive product is visible on the aluminum. On the right side the interface of the FML is shown, after the specimen was delaminated using the edge shear test. Clear signs of corrosion are visible on the interface, where corrosive product is situated on the CFRP and aluminum side.

Temperature influence on the mechanical properties

The mechanical properties of the polymer components in the constituents were temperature dependent. The interfacial properties of the FMEL and FML were examined at 80 °C to determine the behavior of the laminate at elevated temperatures compared to ambient conditions.

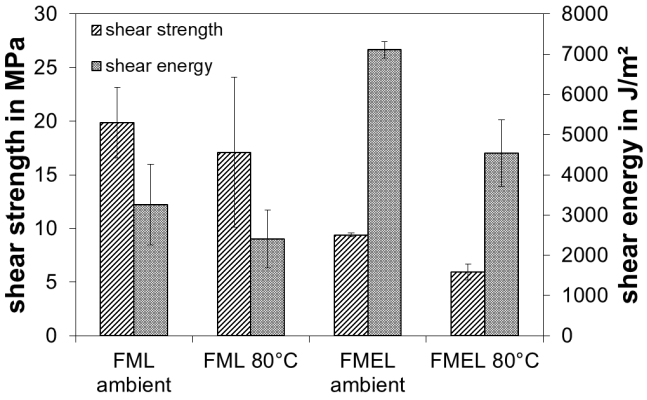

Figure 5.39: Edge shear tests of FMEL and FML at ambient temperature and 80 °C

The interfacial properties of the FMEL and FML visualized in figure 5.39 show the established mechanical properties at ambient temperature. The laminate performance at elevated temperatures was decreased in shear strength and shear energy for both laminates. Also did the scatter increase with the elevated temperature for both laminates. Figure 5.40 presents the curves for the laminates at ambient temperature and at elevated temperature. The FML and FMEL at ambient temperature are presented in black and show the already described characteristics. The FML at elevated temperature (red) showed lower stiffness and shear strength. The shear energy was reduced and the curves had different characteristics.

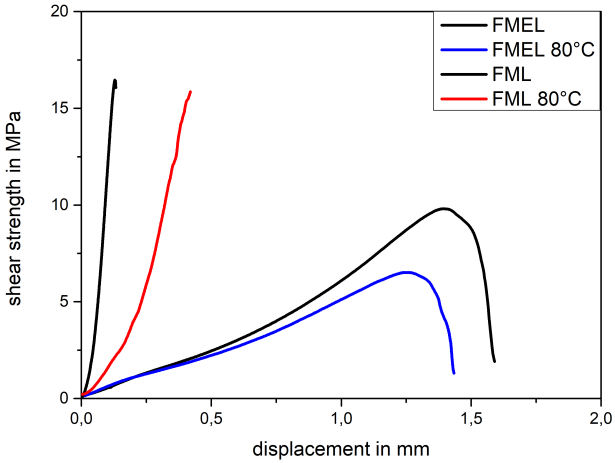

Figure 5.40: Graphs of the edge shear tests of FMEL and FML at ambient temperature and 80 °C

The FMEL (blue) showed 36 % lower shear strength and 37 % lower energy at higher temperatures. The initial stiffness was similar, but after 0.25 mm displacement, the curves diverted and the FMEL showed lower stress values at 80 °C at identical strains compared to the specimens at ambient temperature.

5.3.7 Discussion of the quasi static properties

Tension The tensile properties of FMEL were considerably lower compared to FML, which was caused by the arguably high volume fraction of elastomer in the laminate, which did not carry a significant amount of the load. The biaxial CFRP layer had comparable stiffness to the aluminum layer, but higher strength due to the high strength carbon fibers.
The high ductility of the aluminum did not affect the laminate, as the laminates failed at the same strain to failure as the CFRP layer indicating a CFRP dominated behavior. The beneficial ductile properties of the elastomer interlayer and aluminum were not visible in the FMEL, because the load carried by these constituents was negligible compared to the contribution of the CFRP. Therefore, the CFRP layer defined the failure of the whole laminate. However, the fracture of the FMEL showed the benefit of the elastomer interlayer, as the specimens did not separate due to an intact interlayer and interfaces. Although the specimens failed, the elastomer interlayer prevented constituents separating from the FMEL, which could be important in crash loading. The FML and CFRP showed delamination and specimen separation, which represented a critical failure mechanism.
The properties of the CFRP layers were predicted using the rule of mixtures by Voigt and Reuß, which predicted higher properties than measured in the experiment. The error was within 20 % for all stiffness values of the CFRP and the laminates, which was acceptable as a variation between stiffness prediction and experimental values. The iso-strain assumption for the prediction of the laminates was valid, because the specimens were clamped and differences in strain were prevented.
The strength prediction using classical laminate theory (CLT) showed values with a maximum error of 15 %, except for the transversal strength, which differed strongly. The CLT showed agreeable predictions for the laminates. The FMEL strength was predicted with little error. The strength and stiffness of the FMEL were lower than the FML and CFRP properties.

The resulting strength of the FML was higher than the values for ARALL presented by Vlot et al., which achieved strengths of 850 MPa [31]. The average GLARE strength presented by Vlot et al. of 650 MPa [31] could also be surpassed by FMEL and FML. The elastomer interlayer reduced the strength of FML of 1107 MPa to 712 MPa. Although the FMEL surpassed the average strength of GLARE, the load bearing capability was reduced.
The stiffness of FML was 68.8 GPa and FMEL reached 43.8 GPa, while the stiffness of ARALL ranged from 35 GPa to 42 GPa. The stiffness of GLARE, highly dependent on and increasing with aluminum content, ranged from 40 GPa to 66 GPa depending on the fiber orientation and aluminum content [20]. The aluminum content generally increased the laminate stiffness of GLARE and ARALL, while decreasing the strength. Thus, high stiffness and strength could not be obtained as the GFRP increased the strength and the aluminum enhanced the stiffness. The impact of the constituent content was more extensive in GLARE than in ARALL, because AFRP had properties, which were more similar to aluminum.

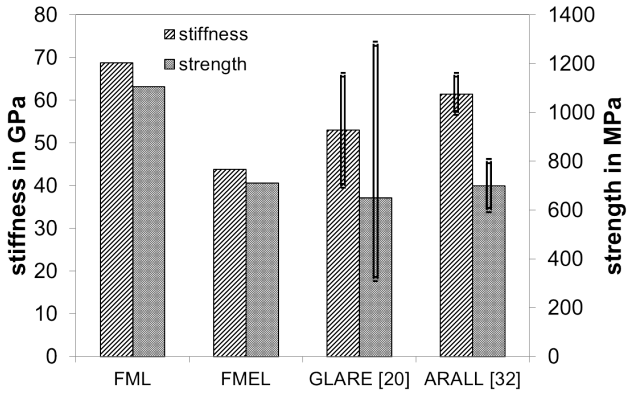

Figure 5.41: Tensile properties of different laminates with the indicators presenting the achievable properties using different layups [20, 31]

Figure 5.41 presents the properties of the laminates in tension. The indicators on the bars do not mark an error, but the achievable properties by variation of the fiber orientation and the aluminum content. These variables were not changed in the FMEL and FML in this work; therefore there is no indicator for different properties. The high properties caused by the stiff and strong carbon fiber in FML are reduced by the elastomer interlayer, resulting in lower FMEL properties. GLARE had higher average stiffness, but lower strength compared to the FMEL in the diagram. However, the high stiffness values for GLARE originated from a high aluminum content, which would reduce the strength. The strength values itself depended greatly on the fiber orientation. High values in strength caused low values in traverse direction combined with low stiffness values. Therefore, the average strength of FMEL was higher than GLARE and nearly identical to ARALL.
The properties of ARALL were higher in average stiffness and strength compared to GLARE, but achievable properties were more restricted. The properties of ARALL generally behaved like GLARE properties concerning aluminum content and fiber orientation. However, since the aramid had a higher stiffness than the glass fiber, the AFRP had a stiffness closer to aluminum.
The mechanical properties of ARALL and GLARE were higher in stiffness, but the average strength was nearly identical to FMEL. The FML presented higher stiffness and strength compared to the other laminates and the best overall values, when only focusing on tensile properties.

Compression The compressive properties of the laminates were dominated by the CFRP constituent. The CFRP failed due to micro-buckling in the carbon fibers, which led to a lower compressive than tensile strength. The tensile strength of the FMEL of 712 MPa was reduced to 308 MPa and the FML was reduced from 1107 MPa to 367 MPa. The significant drop in strength shows the low load bearing capacity of the laminate in compression in comparison to tension.

The compression loads are extremely critical for FRP components, as GLARE also showed a reduction from 650 MPa to 342 MPa. GLARE showed a lower reduction in strength due to the change in loading direction. The FMEL and FML specimens showed macroscopical buckling after the first compressive failure, while the GLARE specimens were thicker, which could have affected the strength. However, the FML surpassed the average GLARE properties, while GLARE presented a higher compressive strength compared to FMEL.

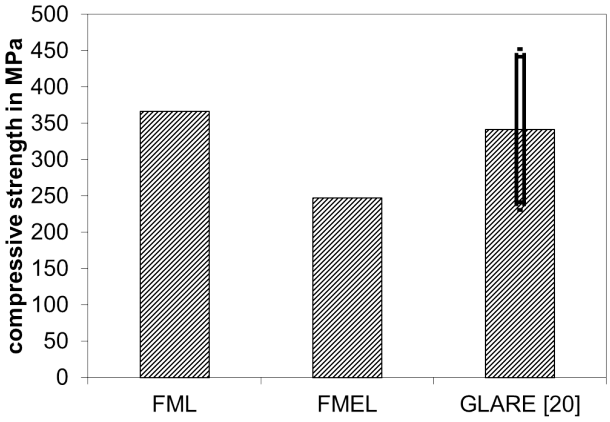

Figure 5.42: Compressive properties of different laminates with the indicator presenting the achievable properties using different layups [20]

Figure 5.42 presents the compressive strength of the laminates and presents the achievable properties using an indicator. The FML showed higher properties compared to the FMEL, which was comparable to the lowest properties of GLARE. The compressive strength of GLARE increased with high aluminum fractions, because the micro-buckling of the GFRP reduced the properties [20]. High compressive strength resulted in low tensile strength of GLARE, because the glass fibers increased tensile while reducing compressive strength.

Bending The flexural properties of FMEL were greatly influenced by the elastomer interlayer. The bending stiffness of the FML was significantly higher than for the FMEL. The reduction in stiffness was caused by the low shear stiffness of the elastomer interlayer. The FML also possessed high strength of 802 MPa ±240 MPa compared to the 308 MPa ±14 MPa of the FMEL, which had higher strains to failure of 8.6 % compared to 2.0 %. The elastomer interlayer moved the CFRP farther away from the neutral fiber, which should have increased the axial moment of inertia and therefore stiffness and strength of the laminate. However, due to the shear soft elastomer the CFRP and aluminum layers deformed in bending relative to their neutral fiber, but did not deform like a monolithic beam. The effective axial moment of inertia was reduced compared to a monolithic specimen with the identical dimensions, which led to lower mechanical properties of the FMEL.
The FML specimens failed due to delamination in the interface, presenting premature failure due to insufficient adhesion, which was presented in figure 5.22. Although the failure was premature, the mechanical properties of the laminate exceeded 1000 MPa in some specimens. The scatter was influenced by the failure, as the premature and sudden failure resulted in a scatter of 480 MPa, which made predictions for the FML difficult. The integration of the elastomer interlayer reduced the mechanical properties; however, the elastomer changed the failure from delamination to tension and compression in the outer fibers, which was more gradual than the FML failure.
The scatter of the results was also minor compared to the FML. The failure of FMEL was less critical compared to the delamination of the FML, which lost structural integrity of the laminate at failure and was difficult to anticipate due to high scatter.

DCB The crack propagation properties of FMEL were examined for interfacial cracks, compared to the cracks in ARALL and GLARE, which were generally in thickness direction [21, 34].

The interfacial cracks were more crucial, because of the higher crack propagation rate, caused by lower interfacial strength. The interfacial properties in the edge shear test showed adhesive failure, which indicated an interfacial crack to propagate. The fiber-bridging and crack stopping mechanisms did not affect the interface, as it was shown by Busch et al. with steel and GFRP laminates [87]. The energy release rate for FMEL was $296.9\,\mathrm{J/m^2}$ $\pm 50.1\,\mathrm{J/m^2}$, while the FML had $204.8\,\mathrm{J/m^2}$ $\pm 53.9\,\mathrm{J/m^2}$. Interlaminar energy release rates for FML with untreated steel and GFRP resulted in G_{Ic} values of $410\,\mathrm{J/m^2}$, which was not reached by both laminates [87].

However, the experiments on the steel-GFRP laminates reported by Busch et al. were conducted at $3\,\mathrm{mm/min}$ compared to $1\,\mathrm{mm/min}$ in this work, which could have resulted in strain dependent behavior.

The interfacial crack in the FMEL propagated in the CFRP-elastomer interface, which was the interface causing failure in the edge shear test and was found to be the weaker interface. The crack propagation of the FMEL was visualized in figure 5.24, where the crack only propagated in the interface proving the interfacial properties to be lower than the CFRP properties. The crack in figure 5.25 propagated into the CFRP layer directly after the pre-crack showing higher properties of the hybrid interface compared to the interlaminar shear strength of the CFRP layer. The hybrid interface enabled the full load bearing capability of the constituents.

The interfacial shear strength of the FML was higher than the FMEL. The DCB experiment was only sensible to strength, but not to strain, therefore, the FML presented the better interfacial properties. The interface was the failure location of the FMEL, although the energy release rate was higher and the shear energy was superior to FML. The DCB experiment evaluated the crack propagation under Mode I loading, which was beneficial for the FMEL, while the edge shear test assessed the Mode II behavior, where the higher strength was exhibited by the FML specimens.

Puncture The integration of the aluminum layer, the step from CFRP to FML, increased the maximum force and retained the displacement of the CFRP. The ductile and isotropic aluminum added load bearing capability and plastic deformation to the CFRP layer. The subsequent integration of an elastomer layer increased the force further and slightly increased the displacement. Relative strain between CFRP and aluminum was possible due to the elastomer layer as discussed in bending. The shear deformation of the elastomer allowed relative strain between the constituents and resulted in 9.2 mm $\pm$1.5 mm deformation compared to 8.4 mm $\pm$0.4 mm of the FML and 8.5 mm $\pm$1.3 mm of the CFRP.

The penetration setup clamped the specimens, which prevented delamination to reduce mechanical properties. Therefore, premature failure was prevented by design of the experiment. The experimental procedure was repeated using ex-situ CT penetration experiments to detect delamination and describe the deformation. The specimens did not delaminate during the penetration experiment, which qualified the interfacial properties of both laminates. The deformation of the free specimen showed the asymmetrical stiffness of the laminate. The wrinkling presented by figure 5.31 was caused by the fiber direction which had high stiffness in radial direction but low stiffness in circumference direction. Therefore wrinkling was possible with a non-clamped specimen. The crack presented by figure 5.32 showed the crack initiation in the outer layer perpendicular to the fiber direction. The crack only penetrated the face layer. The FML showed lower deformation in the CT-scans, with sharper bending radii under the penetrator before failure. The lack of the shear soft elastomer caused the sharper radius in the laminate, which could cause earlier failure in the outer layer, thus explaining the higher scatter in force of the FML.

The mechanical properties obtained in the quasi-static experiment could not be compared to dynamic penetration properties, because of the strain rate dependence, but could visualize the asymmetric behavior of the laminate.

CTE-mismatch The thermal cycling without external load resulted in interfacial stress caused by the CTE-mismatch. The coefficient of thermal expansion of the CFRP was 1.1 μstrain/K, while the aluminum had 23.5 μstrain/K. The elastomer interlayer was able to balance the CTE-mismatch because the shear strength and energy was retained throughout any thermal cycle number. Therefore it was concluded, that the elastomer interlayer was able to balance any stresses originating from the CTE-mismatch of the laminate.

The FML specimens were tested to prove that the CTE-mismatch would cause interfacial damage. The FML specimens showed decreasing properties after 100 cycles and the reduction continued with 1000 cycles. The interfacial properties were reduced by roughly one fourth after 100 cycles and resulted in approximately one third of the original value after 1000 cycles. The extensive damage to the laminate was only observed with the brittle interface, as the load was strain controlled and the FMEL could balance the strain, while the FML had low strains before damage occurred.

The stress-strain curves of the edge shear tests showed that the FMEL had nearly identical behavior at all thermal cycles. The FML presented the same stiffness, but lower strength after thermal cycling. The strength was reduced by 26 % after 100 cycles and by 69 % after 1000 cycles. Thus, the shear energy reduction of 25 % and 62 % respectively was due to the lower strength of the laminate, because the stiffness of all laminates remained constant throughout all thermal cycles. The general characteristics of the interfaces were preserved, only the load bearing capability of the FML was reduced.

The reduction of mechanical properties was found in FML by Botelho et al., but only with a reduction of 4 % due to hygrothermal aging was monitored. The hygrothermal aging did not load the interface as extensively as the thermal cycling and laminate properties were examined instead of the directly reduced interfacial properties. Therefore, the lower reduction in laminate properties agreed with the high decrease of interfacial properties [38].

Corrosion The corrosion resistance properties of the laminates against neutral salt spray were analyzed by measuring the residual interfacial properties using the edge shear test. The FMEL specimens tested in the edge shear test after being in corrosive environment for 48 h and 96 h had some variation around the values presented by the virgin FMEL, but the properties were generally retained throughout the corrosion. The 96 h specimens showed a 15 % reduction of strength and 7.5 % reduction in energy. The elastomer had isolating properties according to the data sheet [131], but at long durations a very slow corrosive reaction could happen as shown at the edges in figure 5.38. However, the properties of the laminate were nearly constant after extensive corrosion loads qualifying the elastomer layer as a decoupling layer. The scattering of the FMEL specimens increased with increasing corrosion duration, which may be caused by the aluminum showing slight corrosive product on the edges. Although the specimens were not significantly impacted by corrosion, the laminate was not impervious to corrosive loads.

The FML interfacial properties of virgin specimens were reduced by 93 % after 48 h in the corrosive environment. The residual strength and energy were at 7 % of the initial value proving a very strong effect of the corrosion on the interface. The specimens loaded by the salt spray for 96 h delaminated without external force and could not be tested. The interface of the FML reacted to the corrosive load showing the need for electrical decoupling, which could be achieved exemplarily by the sol-gel coating used by Wang et al. [12] to prevent corrosion. It was found, that FML without coating was subject to severe corrosion, while the coating could reduce the corrosion, but the laminate was still damaged. The elastomer layer had a bigger impact on the corrosive properties of FML compared to the sol-gel coating, showing the benefit of the elastomer layer.

The elastomer interlayer was exhibited by Sarlin et al. to hot, moist and hot and moist environments, where the elastomer by Kraiburg showed reduced mechanical properties after hot, moist and hygrothermal treatment. The interface to GFRP did not degrade due to the environment. However, the peel force of the elastomer layer on steel was reduced from 268 N to 55 N due to hot as well as moist exposure [41]. This effect could not be found in the FMEL, as firstly the elastomer CFRP interface was the critical interface and a weakening of the metal elastomer interface was not detected after thermal cycling or corrosion. Secondly did the shear strength and energy of the FMEL not decrease after moisture in this study.
The specimens after corrosive loads showed minor signs of corrosion. The FMEL had corrosive product on the edges only, showing that the corrosion was retained to the surface of the specimen and could not penetrate the laminate. In contrast to the FMEL, the FML, which was in the chamber for 48 h showed corrosive product in the interface of the specimens. The entire interface was covered in the product correlating with low interfacial properties.

Elevated temperature The properties of the laminate at elevated temperature were determined using shear edge tests at 80 °C. The shear strength and energy of FMEL and FML was reduced compared to ambient temperature. Since the displacement was also reduced, but the form of the curve was identical to the ambient temperature FMEL, the high temperature had an effect on the elastomer interlayer. The FML showed lower stiffness values combined with reduced strength values. The temperature had also an impact on the FML interface, weakening the matrix in the interface and therefore reducing interfacial properties.

5.4 Dynamic characterization of the laminate

Many applications are subject to dynamic loads, which are either recurring or crash related events resulting in different mechanical properties and therefore the materials need to be examined concerning the dynamic resistances.
The dynamic properties concerning crash and impact properties were examined using charpy, puncture and impact experiments. The damage tolerance of the laminates was determined using the compression after impact test.

5.4.1 Charpy properties

The charpy tests were conducted on both laminates and CFRP to determine the different dynamic properties. The absorbed energy was measured to determine the performance of the laminates.

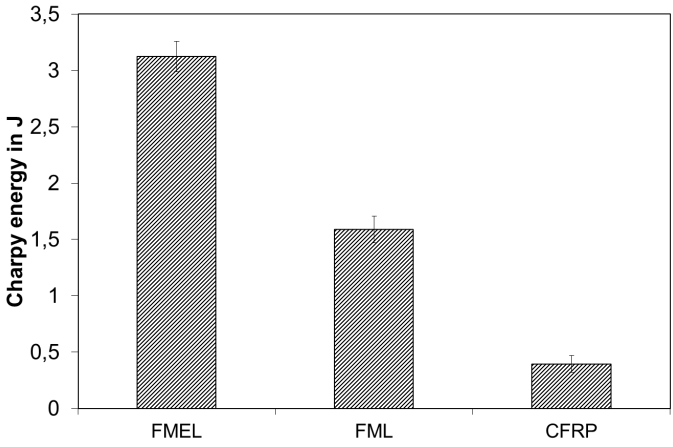

Figure 5.43: Charpy energies of FMEL, FML and CFRP

The charpy energies for FMEL, FML and CFRP are visualized in 5.43. The absorbed energy of the FMEL was significantly higher compared to the FML and CFRP. The brittle CFRP showed the lowest energy to failure, which could be increased by the integration of an aluminum layer and the corresponding interfaces. The highest energy absorption was achieved by adding the very ductile elastomer to the FML and again increasing the number of interfaces.

Figure 5.44: Fractured FMEL (left), FML (middle) and CFRP (right) after charpy tests

Figure 5.44 presents the fractured specimens after charpy testing. The FMEL specimen on the left had tension and compression failure in the CFRP, but the inner four layers of the CFRP were still intact. The FML specimen in the center shows tension and compression failure through the whole CFRP layer, thus, more CFRP layers failed compared to the FMEL. The crack propagated to the aluminum layer, which did not allow further crack propagation. The biaxial CFRP specimen had a crack through the center of the specimen, where the transverse layers showed matrix fractures and the longitudinal layers had fractured fibers and still intact fibers preventing specimen separation.

5.4.2 Puncture properties

The FML and FMEL were examined under dynamic puncture loads to determine the benefit of the elastomer. The puncture properties defined the laminates' resistance against a small object penetrating the structure.
The absorbed energy and specific absorbed energy accounting for the density were used to compare the properties of the laminates and are visualized in figure 5.45.

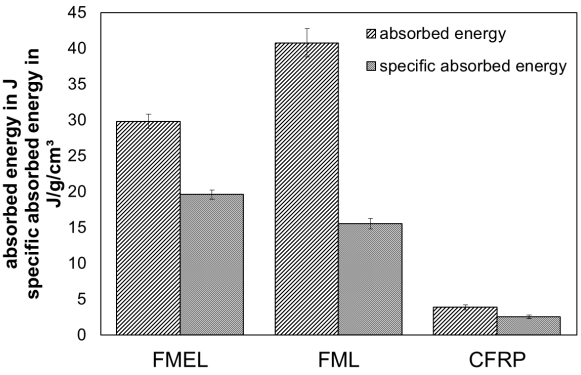

Figure 5.45: Absolute and specific absorbed energy by FMEL, FML and CFRP in the dynamic puncture test

Figure 5.45 shows the absorbed energies and also the specific absorbed energies of the laminates and CFRP to account for lightweight potential. FMEL had a lower absolute absorbed energy compared to FML. The specific absorbed energy, however, was slightly higher. The higher density of the FML led to slightly lower specific properties compared to the FMEL, as the low density of the elastomer layers caused a lower laminate density. The CFRP had the lowest mechanical properties in both absorbed and specific absorbed energy. The CFRP, consisting of two brittle components, carbon fibers and epoxy matrix, showed little deformation before failure in figure 5.46.

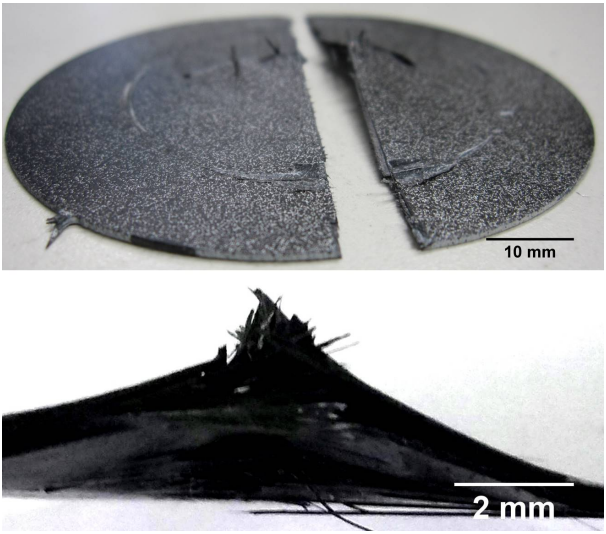

Figure 5.46: CFRP puncture specimen after the experiment

It shows the CFRP specimen after a puncture test with the fracture perpendicular to the fiber direction of the outer layer. Plastic deformation was low, but delamination between the CFRP layers was observed in the center.

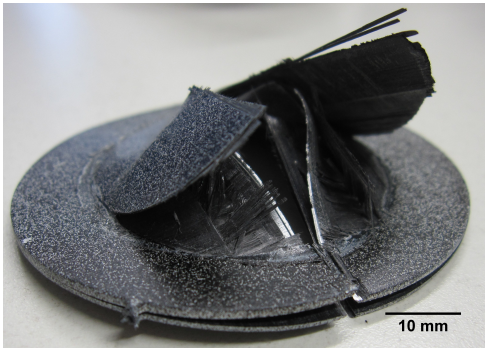

Figure 5.47: FML specimen after the puncture test

Figure 5.47 shows a FML puncture specimen after the experiment. In comparison to figure 5.46, the integration of the aluminum layer resulted in higher plastic deformation. The failure mechanisms of the laminate were delamination, plastic deformation and failure through fiber and matrix fracture. Delamination was found between the CFRP layers in the center of the specimen, while the delamination between aluminum and CFRP could also be detected in the front as well as in the center. The aluminum layer showed high deformation, while the fracture was oriented in 90 ° to the outer CFRP fiber layer.

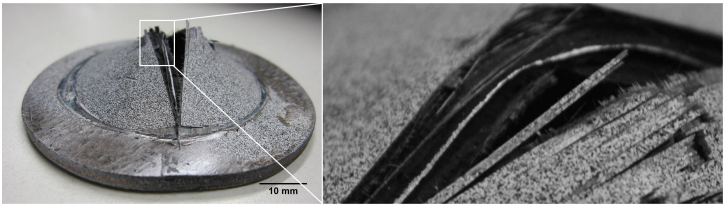

Figure 5.48: FMEL specimen after the puncture test with an enlarged fracture area

Figure 5.48 shows high deformations of 10.9 mm without large delamination caused by the penetration test compared to 2.3 mm deformation of the CFRP specimen. The integration of the elastomer interlayer resulted in the prevention of delamination between the constituents, because the hybrid interface in figure 5.48 is still intact. Delamination between the CFRP layers could be found in the fractured area. Also a surface crack was found in the mounting area on the left side of the specimen, which did not cause failure. Compared to the laminate in figure 5.47, the structural integrity of the FMEL was significantly better due to reduced delamination. The FMEL did not show specimen separation compared to FML and CFRP.

5.4.3 Impact properties

The damage tolerance of the laminates was determined using impact experiments. The impact experiments resembled a small object with a defined energy hitting the laminate and measuring the laminate resistance. The damage to the laminate was quantified in subsequent residual strength measurements. The residual mechanical properties were determined using the compression after impact (CAI) test.
The impact tests were aided by high speed imaging and digital image correlation (DIC) with ImageJ and OriginPro to determine the velocity of the impactor before and after the impact to calculate the absorbed energy. The laminates tested in these experiments had the same thickness to prevent different moments of inertia. However, this meant a big difference in stiffness of the laminates, as the FML had CFRP layers which were thicker compared to the FMEL CFRP layers.

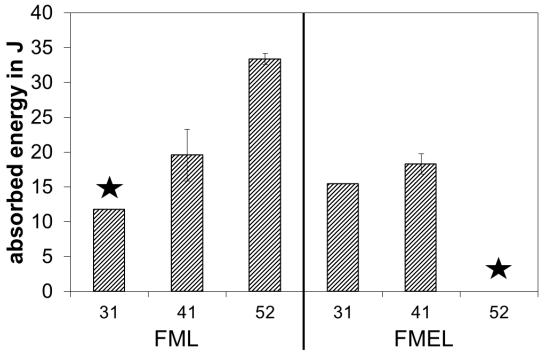

Figure 5.49: Absorbed energy values of FML and FMEL at different impact energies and asterisks marking unsuccessful measurements

In this work the absorbed energy calculated through the kinetic energy and the force displacement diagram had a maximum variation of 1.8 %.

The laminates were damaged with impact loads of 31 J, 41 J and 52 J. The absorbed energy of the laminates is presented in figure 5.49.
The absorbed energy in figure 5.49 was calculated using the difference in impactor velocity before and after the impact. The absorbed energies marked with an asterisk were not measurable due to movement of the sphere out of the filmed area. The FML specimens showed increasing energy absorption with increasing impact energy. The asterisk at 31 J represents an invalid absorbed energy measurement, which was not obtainable with DIC and therefore only one valid measurement could be presented for 31 J. The specimens, which did not have an absorbed energy value were discarded for the impact analysis, but could be used for the CAI experiments. One FML specimen was discarded for the 31 J energy and three FMEL specimens could not be measured at 52 J.
The increasing impact energy resulted in a large absorbed energy increase for the FML. The FMEL values increased from 31 J to 41 J impact energy, but the difference was smaller compared to the FML. The energy absorption at 31 J was exactly identical for all specimens, thus, explaining the missing error indicator. The 52 J impact energy resulted in invalid DIC measurements for all specimens, should however have showed slightly higher absorbed energy values than the 41 J load level. The FMEL showed higher absorbed energy at the lowest impact energy level, but lower values than FML at 41 J.
The damage to the laminate could not be derived from the absorbed energy; therefore, the specimens were inspected optically to determine the extent of the damage. FML at 31 J and 41 J as well as FMEL at 31 J did not show any visual damage.
The damage description in table 5.2 is consistent within the laminates and impact energies. The FMEL was damaged more extensively compared to the FML at identical impact energies.

Table 5.2: Impact damage of FMEL and FML

laminate	damage
FML 31J-1	no visual damage
FML 31J-2	no visual damage
FML 41J-1	no visual damage
FML 41J-2	no visual damage
FML 41J-3	no visual damage
FML 52J-1	slight plastic deformation, small surface crack
FML 52J-2	slight plastic deformation, small surface crack
FMEL 31J-1	no visual damage
FMEL 31J-2	no visual damage
FMEL 31J-3	no visual damage
FMEL 31J-4	plastic deformation, surface crack
FMEL 41J-1	plastic deformation, surface crack
FMEL 41J-2	plastic deformation, surface crack
FMEL 41J-3	plastic deformation, surface crack
FMEL 41J-4	plastic deformation, surface crack
FMEL 52J-1	extensive plastic deformation, large CFRP crack
FMEL 52J-2	extensive plastic deformation, large CFRP crack
FMEL 52J-3	extensive plastic deformation, large CFRP crack

The FMEL specimen in figure 5.50 at 41 J impact energy showed a crack on the tension side opposite the impacted area after the impact. The crack was in the center of the specimen did not reach the edge. Plastic deformation caused by the impact event was also visible. The crack existed in multiple unidirectional CFRP layers, but did not penetrate the full biaxial CFRP layer. Therefore, it was confined within the CFRP.

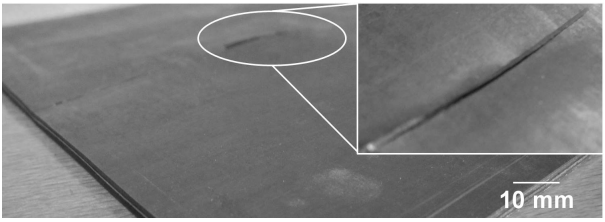

Figure 5.50: 41 J FMEL specimen after the impact

Figure 5.51: 52 J FMEL specimen after the impact

The 52 J impact energy led to damage in the tension side of the FMEL specimen visualized in figure 5.51. The aluminum is deformed and the CFRP exhibits significant damage. The crack from the impact propagated to the edge of the specimen and there is delamination visible around the crack. The crack reached the aluminum, thus, fully separating the CFRP layer. However, the crack only existed from the impact location to one edge of the specimen and did not propagate to the other edge.

The FML only showed visible damage at the highest energy level of 52 J, which is presented in figure 5.52. The plastic deformation was lower compared to the FMEL specimens and a comparably small matrix crack appeared. The crack existed in the top two CFRP layers and did not reach the edges of the specimen.

Figure 5.52: 52 J FML specimen after the impact

Validation of the impact prediction

The deflection of the laminates was predicted according the energy balance model presented by Shivakumar et al. [80]. The energy of the impactor was transferred to the laminate, which resulted in contact, membrane and shear deformation. Equation 5.1 by Shivakumar et al., was used to calculate the deflection w. The mass m of the impactor and the initial impactor velocity v calculated the energy transferred to the laminate. The effective stiffness against bending and shear K_{bs} and against membrane deformation K_m is used with the contact stiffness parameter n_s and the deflection w to predict the laminate response in the impact event. The material properties from the data sheets were used to calculate the laminate response [129, 130, 131].

$$m * v^2 = K_{bs} * w^2 + \frac{K_m * w^4}{2} + 4/5 \left[\frac{(K_{bs} * w + K_m * w^3)^5}{n_s^2} \right]^{1/3} \tag{5.1}$$

The deflections were calculated using the solver tool in Microsoft Excel since the deflection w could not be isolated in the equation and solved analytically. The resulting deflections were calculated and compared to measurements obtained by high speed imaging. Both values are presented in table 5.3.

Table 5.3: Impact deflection prediction and experimental results

laminate	predicted deflection	measured deflection	difference
FML 31J-1	7.028 mm	7.138 mm	1.5 %
FML 41J-1	8.335 mm	7.304 mm	14.1 %
FML 41J-2	8.336 mm	8.300 mm	0.4 %
FML 41J-3	8.339 mm	7.802 mm	6.9 %
FML 52J-1	9.525 mm	8.798 mm	8.3 %
FML 52J-2	9.525 mm	8.466 mm	12.5 %
FMEL 31J-1	8.631 mm	8.632 mm	0.01 %
FMEL 31J-2	8.627 mm	11.122 mm	22.4 %
FMEL 31J-3	8.626 mm	11.288 mm	23.6 %
FMEL 31J-4	8.627 mm	10.624 mm	18.8 %
FMEL 41J-1	10.248 mm	13.612 mm	24.7 %
FMEL 41J-2	10.247 mm	12.118 mm	15.4 %
FMEL 41J-3	10.246 mm	13.446 mm	23.8 %
FMEL 41J-4	10.247 mm	12.284 mm	16.6 %

The results in table 5.3 show that the deflections calculated for the FML could predict the results of the experiment well, as the difference between prediction and experiment was below 15 %.
The FMEL, however, except for one specimen, showed larger discrepancies of 15 % to 24 % between prediction and result, which originated from the shear soft elastomer. The low shear stiffness of the elastomer led to an underestimation of the effective bending and shear stiffness K_{bs}, which led to a higher predicted deflection of the laminate.

5.4.4 Compression after impact properties

The compression after impact tests were conducted to define how the damage to the structure caused by the impact affected the residual mechanical properties of the laminates. The FML had lower damage to the structure in the impact test at the same energy compared to the FMEL as previously described. The values for the laminates were compared to specimens without impact damage to determine the damage tolerance of the laminate. The damage mechanisms were analyzed to describe the failure of the laminate with respect to the impact event.

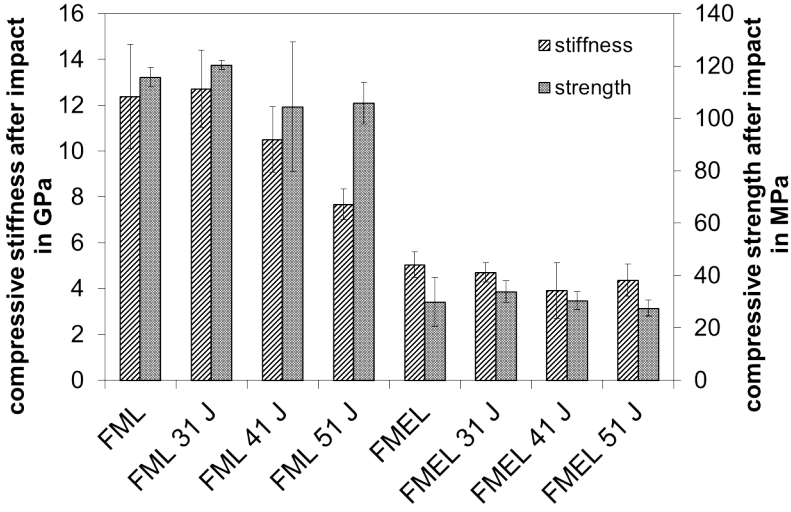

Figure 5.53: Compression after impact properties of FML and FMEL

Figure 5.53 shows the compression after impact properties of FML and FMEL specimens. The virgin FML specimens showed 12.4 GPa of stiffness and 115.7 MPa of strength. The lowest impact energy of 31 J did not damage the laminate sufficiently to decrease the mechanical properties.

The intermediate impact at 41 J showed a minor decrease of strength to 104.4 MPa and stiffness to 10.5 GPa combined with higher scattering in strength. The high impact energy resulted in a large decrease in stiffness to 7.7 GPa; however, the 105.8 MPa strength of the laminate remained nearly identical to the 41 J specimens with 104.4 MPa.
The virgin FMEL specimens showed lower stiffness and strength of 5.1 GPa and 29.9 MPa respectively. The specimens impacted with 31 J showed minor decreases in stiffness to 4.7 GPa and increases in strength to 33.7 MPa. The trend of a stiffness decrease continued to the 41 J specimens with 3.9 GPa, which a strength of 30.5 MPa, which was comparable to the virgin specimens. The highest impact energy of 52 J slightly increased the stiffness to 4.4 GPa compared to 41 J, while a minor decrease in strength to 27.6 MPa was visible. The change in mechanical properties of the FMEL was comparably low in respect to the extensive damage detected after the impact.
The CAI results generally show that the stiffness was affected more by the impact damage compared to the strength.
The CAI experiments showed two kinds of failure in the laminates. Virgin specimens and laminates with no visual damage showed compression failure, while the more extensive damage led to compression failure originating from the impact location.

Figure 5.54: FMEL after CAI test and failure by compression

Figure 5.54 shows the compression failure of FMEL in the marked area. Virgin specimens and specimens at low impact energies, which meant 31 J for the FMEL and 31 J and 41 J for the FML, showed this failure mechanism.

The FML failing due to compression also exhibited delamination presented in figure 5.55.

Figure 5.55: Fractured FML in CAI test with the failure and delamination starting from the edge

The FML in figure 5.55 shows compression failure in the marked area combined with delamination marked by the arrow. The delamination was visible after the experiment, because the experimental setup prevented the detection in the experiment through clamping.

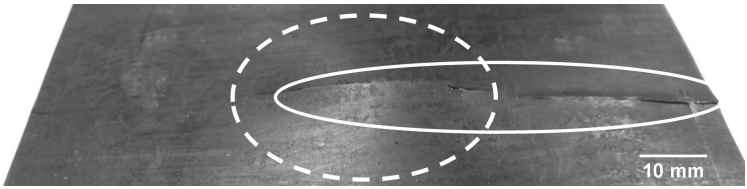

Figure 5.56: Fractured FMEL in CAI test with the failure originating from the impacted area marked with a dashed line

In specimens with extensive damage, which was 41 J and 52 J for FMEL and 52 J for FML, the failure initiation was at the impact area. The impact area is marked in figure 5.56 by the dashed line. The failure propagated outward from the previously damaged zone, reaching the edge and resulting in macroscopical buckling. The crack by the impact was within the dashed line and grew in the CAI experiment starting from the initial damage.

5.4.5 Discussion of the dynamic properties

The dynamic properties of the FMEL and FML were dominated by the interfacial performance of the laminates, because crack stopping effects or delamination influenced the mechanical properties.

Charpy The brittle CFRP specimens had the lowest Charpy energies, because plastic deformation did not occur. The FML specimens, which had an additional aluminum layer and the corresponding interfaces compared to the CFRP, presented higher Charpy energies. The failure in the CFRP, which showed brittle behavior, was changed due to the aluminum layer. Although the CFRP layers in the FML presented brittle failure, the interface and aluminum layer were intact, while the aluminum layer showed large plastic deformation. The cracks in the CFRP face layers could not penetrate the aluminum layer through the interface, which showed the crack-stopping effect. The crack was stopped at the interface and the adjacent material was not subject to crack growth, but could exhibit high mechanical properties for the laminate.

The FMEL, which benefited from the integration of two elastomer layers and the corresponding interfaces, exhibited even larger Charpy energies. With the elastomer a second ductile material was included in the laminate, which also allowed relative deformation of the constituents caused by shear deformation in the elastomer. The effect of the elastomer, already mentioned in the flexural properties, allowed higher deformation of the laminate before failure. Therefore the specimen after Charpy testing still had intact inner CFRP layers and less plastic deformation in the aluminum.

The interfaces of both laminates remained intact in the Charpy experiments. In the FML the interface was crucial to prevent specimen separation and critical failure. The interface was already found by Schijve et al. [35] to reduce the crack propagation speed, although the experiments were fatigue and not Charpy experiments.

The laminates consisting of aluminum and polymer reduced crack propagation rates, presenting the influence of the interface. However, it was observed that the crack could not easily propagate through the interface into the adjacent material, which either deflected the crack or increased the energy necessary for the crack to propagate further. A comparable effect was seen in the FML, where the crack was stopped at the CFRP-aluminum interface and the aluminum showed plastic deformation instead of crack growth. The FMEL did not show crack stopping effects, as the crack did not propagate through the entire CFRP layer, because the ductility of the elastomer allowed large deflections and therefore reduced stress in the CFRP, while increasing the absorbed energy of the laminate.

Puncture The puncture properties of the laminates surpassed the CFRP properties as in the Charpy experiments. The brittle CFRP properties could be enhanced by the integration of ductile layers.
The brittle nature of the CFRP led to low absorbed energies in the experiment and the specimen did not present large plastic deformation after fracture. Additionally, the fracture of the CFRP led to specimen separation although it was clamped in the experiment, presenting low resistance to crack propagation under puncture loads.
The integration of an aluminum layer into the CFRP with the corresponding interfaces increased the energy absorption drastically. The absorbed energy was increased from 3.9 J by 660 % to 40.8 J due to the aluminum interlayer. The failure of the FML showed large delamination of the constituents and within the CFRP. The hybrid interface delaminated on a large scale and the CFRP layers also delaminated throughout the free specimen area. The specimen was separated after the experiment and delamination of the hybrid interface in the clamped area was also detected. Although the laminate exhibited high mechanical properties, the failure was critical due to large delamination within the CFRP and the hybrid interface but also specimen separation.

The specimen separation showed that the crack also propagated through the clamped zone of the specimen. Tsartsaris et al. [123] showed on GFRP-aluminum laminates that delamination and cracks in the brittle matrix occurred due to the impact event and therefore damaged the structure, where delamination could occur.
The FMEL showed 25 % lower properties at 29.9 J than the FML, which was in strong contrast to the Charpy results. However, the specimens were clamped in the penetration test, which did not allow relative movement of the layers. Therefore, a large benefit of the elastomer layer presented in the Charpy experiments may not have had an impact on the penetration properties.
The FMEL had a lower density compared to the FML and the specific absorbed energy used to compare aircraft materials was higher than in FML. The failure in FMEL showed delamination in the CFRP constituent, which was minor compared to the FML. The specimen was still structurally intact and large plastic deformation like in the FML was visible after the experiments.
The puncture energy for GLARE at comparable thickness was 49 J for GLARE 5/4, which was higher than the properties of FML and FMEL. The specific absorbed energy was $21.3\,\mathrm{J/(g/cm^3)}$, which was slightly higher than the FMEL properties at $19.6\,\mathrm{J/(cm^3)}$ and higher than the FML values of $15.6\,\mathrm{J/(cm^3)}$. However, the GLARE laminates were tested with a wider support structure, allowing a larger bending and membrane stress. Therefore, the shear stress in the laminate was reduced, which caused the delamination of the CFRP constituent and could have reduced the properties of FML and FMEL [1]. Experiments by Vlot et al. with similar dimensions reduced the absorbed energy of GLARE 3 to 33 J, which resulted in a specific absorbed energy of $14.4\,\mathrm{J/(g/cm^3)}$, showing the benefit of the low density of the FMEL and FML. The puncture energy for ARALL was below 10 J due to delamination and therefore lower than FMEL and FML [124].

Impact The impact properties of the laminates showed significantly different results for the FMEL and FML specimens. The constant thickness of FML and FMEL resulted in a very thick CFRP layer in the FML, which had 1.1 mm CFRP face sheets on the aluminum core. Thus, the CFRP layers were nearly twice as thick as the FMEL CFRP layers. The increased stiffness of the FML resulted in lower damage compared to the FMEL specimens at the same impact energy. The constant thickness was essential to prevent different properties due to the variation in the axial moment of inertia, but resulted in different levels of damage in the laminates.

The impact experiments did not show any detectable damage at the lowest energy level in either laminate. The intermediate energy resulted in damage in the FMEL and the highest energy caused damage in FML and FMEL specimens. The damage increased with increasing impactor energies.

The absorbed energy of the FML specimens constantly grew with the increased impact energy, which showed that the damage done at the lower and intermediate level was comparably low. The energy absorption was highest at the highest level and the damage was visible at 52 J.

The FMEL had higher energy absorption properties at the low impact energy level compared to the FML, which was accounted to the elastomer interlayer. The scattering was extremely low within the four specimens at that load level, which was caused by the stress distribution of the elastomer interlayer. The intermediate and high energy levels damaged the laminate more extensively as described in the optical analysis. The energy absorption did not increase largely as with the FML specimens, when the impact energy was increased from 31 J to 41 J. The 41 J energy level caused crack propagation, which showed the threshold for this damage mechanism was shortly above the 31 J. The damage at the 52 J level was drastic, because the threshold for crack propagation was largely exceeded.

The impact properties were analyzed analogous to Dietrich et al. [83], using a high speed imaging technique, but a bigger and heavier impactor.

The research presented by Song et al. [127] showed higher force values of 4.5 kN at 9.4 J impact energy when impacting FML consisting of CFRP and aluminum, however, aluminum face sheets were used. The experimental support differed and therefore differences in properties were found, as he maximum force at 31 J impact energy was 2.3 kN for FMEL and FML.
FML specimens with aluminum face sheets were used, which showed the damage well, because cracks and plastic deformation could be detected at 9.4 J, where in FML and FMEL damage was not visible.
Vlot et al [124] used thinner GLARE 3 laminates, but visualized the benefit of the metal layer in the laminate, which increased the properties of the GFRP by a factor of ten. The impact properties determined in literature, at low velocities and high weights, are attributed to accidents in the airport and not during operation.
The small mass, high velocity impact [83] resembles a small mass accelerated and hitting the structure, which can be compared to stone-chipping on a highway. Even at the identical energy the results of small and high masses can vary, as strain rate dependencies could affect the results. Therefore, the results of the research are not generally transferable. However, the research conducted by Vlot [124] and Song [127] generally showed that the integration of an aluminum interlayer is beneficial for the FRP constituent and that the impact resulted in delamination and matrix cracks. The research corresponded well with the results for FML and FMEL.
The impact properties were predicted using the energy balance model according to Shivakumar et al. [80] to define the deflection of the laminates based on quasi-statically obtained mechanical properties. The prediction fit the experiment for the FML very well, but the FMEL prediction and experiment showed a variation. The FML had a good estimation for the experiment, because the stiffness of the constituents was high and no relative displacement between the constituents was possible. The FMEL had a shear soft interlayer, which resulted in lower stiffness, lower shear modulus and higher deflection.

The FMEL allowed the constituents to have relative deformation due to the shear deformation of the elastomer interlayer. This deformation of the laminate could not be accounted for in the prediction, and therefore the error in predicted deflection rose. The error of the FMEL prediction to the experimental values was below 24 %.

CAI The compression after impact tests following the impact tests and the damage detection connected visible impact damage with failure starting at the damaged area and therefore lower mechanical properties. Non-visible damage did not lead to a reduction of mechanical properties.
The failure mechanism in FML at low impact energies, where the impact did not damage the laminate, was compressive failure. The mechanical properties of virgin laminates were reached by impacted laminates without visible damage, therefore, defining the FML damage tolerant up to 41 J.
The laminates with visible impact damage showed reduced mechanical properties. The stiffness of the laminates was affected more extensively than the strength. The failure mechanism in FML was compressive failure starting from the impact area, which showed that the impact load decreased the mechanical resistance and acted as the failure initiation point. The FML specimens with visible damage delaminated due to insufficient interfacial properties in the brittle FML interface.
The FMEL showed damage tolerance up to 31 J, because starting with 41 J the impact zone acted as failure initiation area and reduced the mechanical properties. The elastomer interlayer prevented delamination of the FMEL at all load levels.
Other research focused on fatigue after impact due to a better proximity to the application; however, the compression load was more critical for the damaged laminate. It showed a clearer selectivity for the damage tolerance threshold, which defined the start of decreasing properties.

Kinsey et al. [85] showed on woven CFRP laminates the degradation of the CFRP properties due to the impact of 3 J on the specimens. The CFRP as a brittle material showed a drop of nearly 50 % in mechanical properties at the lowest impact energy resulting in low damage tolerance. The integration of an aluminum layer in the FML increased the damage tolerant behavior of the laminate as an impact with 5 J only led to a reduction of 15 %.
The FML, which are predominantly used in aviation, were commonly examined in fatigue after impact of 16 J to 64 J. Laliberte et al. [36] presented the fatigue performance of GLARE-3-2/1, GLARE-4-2/1, GLARE-5-2/1 and aluminum post impact, where a small, barely visible damage to the structure did not decrease mechanical properties significantly, showing the damage tolerance of the materials. The impact damage to FML in research needed to be large for a decrease in residual properties, as Beheshty et al. [145] presented marginal changes for CFRP in the tension properties after impact of 1 J to 5 J.
The laminates showed damage dependent behavior and the threshold for the reduction of CAI properties could be corresponded with visible damage to the structure, which also caused a change in failure mechanism.

5.5 Fatigue experiments and lifetime prediction

Fatigue experiments were conducted to describe the material behavior under recurring near application loads. The fatigue properties of the FMEL and FML were predicted using a superposition of constituent lifetime predictions. Additionally to tension-tension fatigue, tension-tension thermal mechanical fatigue experiments were conducted.
The differences caused by the elastomer interlayer in fatigue performance were determined in fatigue loading and additionally with superimposed thermal loads.

5.5.1 Tension-tension fatigue properties

The fatigue properties of the FMEL were evaluated concerning mechanical properties of the laminates, but also the fracture mechanics, concerning the possibility to describe and detect failure mechanisms, were characterized. The fracture of the constituents and load bearing capability during the fatigue experiments were evaluated. The influence of the interfacial properties on the fatigue properties was analyzed as well.
The specimens were tested at 80 %, 55 %, 40 % and 25 % of the ultimate tensile strength, as it was proposed in ISO 13003. However, since the FMEL experiments at 40 % did not meet the failure criterion at 2 million cycles, the 25 % load level was therefore omitted. It was shown that the fatigue endurance limit was higher than 40 % of UTS, as failure did not occur rendering experiments at lower loads non-essential.

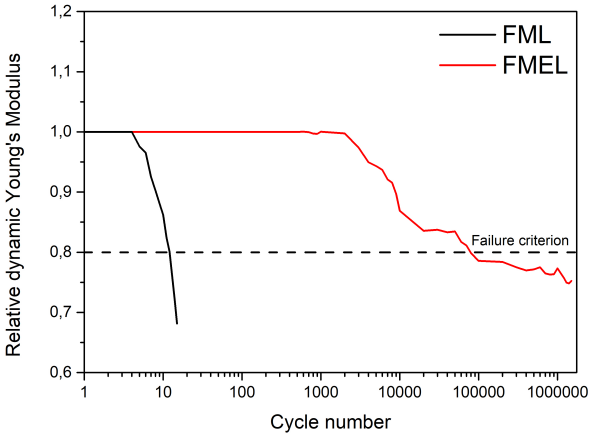

Figure 5.57: FML and FMEL relative dynamic Young's modulus over the loading cycle curve during the fatigue experiment at 55 % of UTS [150]

The FML showed low performances at all load levels proposed by the standard; therefore, an additional lower load level was added at 12 % of UTS. The FML and FMEL specimens showed degradation of mechanical properties during the experimental procedure, which is exemplary presented in figure 5.57. The laminate started with the initial stiffness, which decreased due to the fatigue loading and met the failure criterion of 20 % stiffness reduction. The relative dynamic stiffness in figure 5.57 met the failure criterion for FMEL at approximately 60.000 cycles, which was then used to obtain an S-N curve for the laminate. The FML only 12 cycles to failure.
The laminate, consisting partly of polymers, can exhibit increased temperature, which is caused by internal friction of the polymer components. Therefore, the temperature was monitored throughout the fatigue experiments to detect whether the temperature increase was below the threshold of 5 °C defined in ISO 13003 [100].

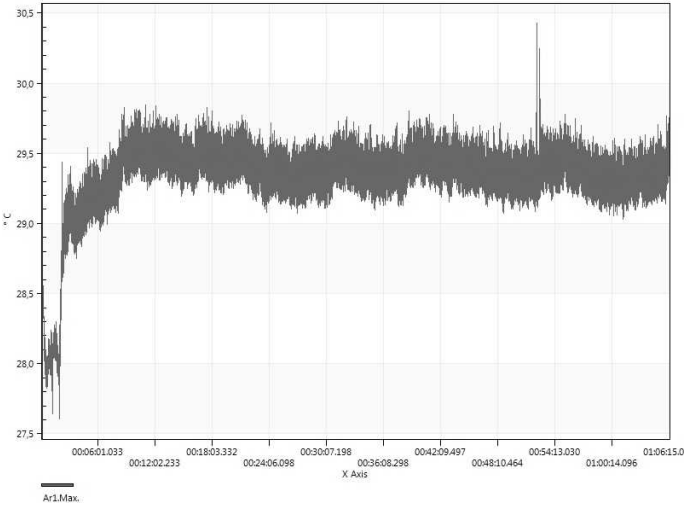

Figure 5.58: Temperature development of the FMEL specimen during the fatigue testing [150]

Figure 5.58 shows the temperature development in the FMEL specimen during the fatigue test at 80 % of UTS. The highest load level had the highest strain rate and highest loads, which caused the highest temperature increase in the laminate. A constraint was to monitor the temperature development during fatigue testing to analyze the validity of the experimental procedure. The threshold of 5 °C could not be exceeded for a valid experiment, therefore, the graph visualized the validity of the experiment as the temperature increase was approximately 1.5 °C. Lower stress levels had lower temperature increase values and all experiments were valid concerning the temperature threshold.

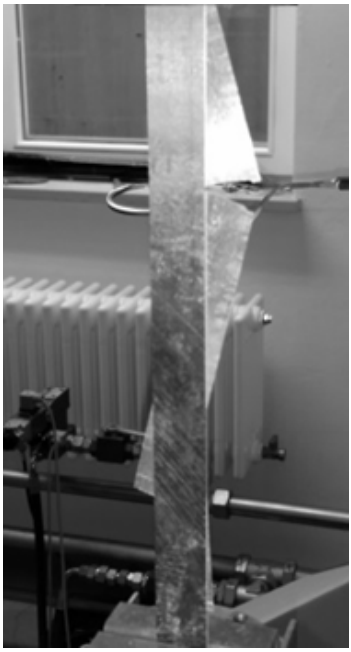

Figure 5.59: Delaminated FML specimen at the lowest load level of 25 %

The FML specimen presented in figure 5.59 shows delamination of the constituents and multiple fractures of the aluminum. The interface fractured in the FML resulting in three individual layers. The aluminum layer subsequently fractured and the failure criterion was met at low cycle numbers. The premature failure of the laminate was detected at all load levels defined in ISO 13003 resulting in an additional, lower load level at 12 % of UTS.

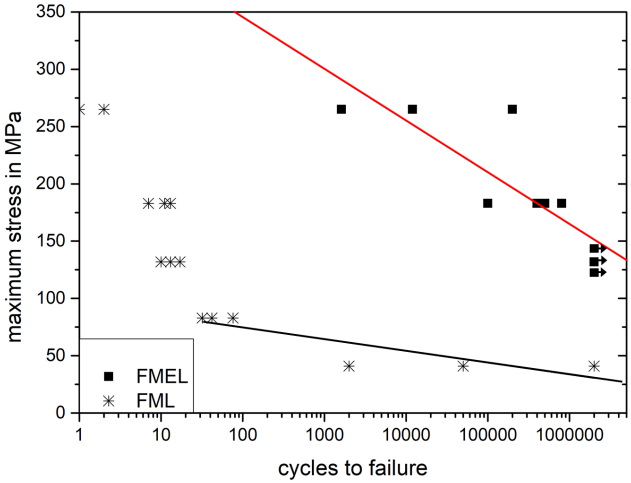

Figure 5.60: S-N curves for both laminates with data points from fatigue experiments [150]

Figure 5.60 shows the S-N curves for FML and FMEL. The curve for the FML was obtained by using data points with a minimum cycle to failure value of 20 cycles. The FMEL specimens failed due to a stiffness decrease caused by transverse matrix cracking in the CFRP component and aluminum fracture. The elastomer did not fracture or delaminate due to the high failure strain and good adhesion.

Specimen separation never occurred, because the elastomer inhibited delamination and the CFRP layers did not separate during the fatigue experiments. The FML specimens showed delamination. At the lowest load level the delaminated specimen did not show facture of the constituents, but at the four higher load levels the aluminum fractured after delamination as presented in figure 5.59.

The experimental data shows that the cycles to failure of the FMEL were higher than the FML at any given load level. The red line indicates an average performance of the FMEL specimens.

The fatigue experiment presented the lowest level in the fatigue endurance region, while the highest level was in the low cycle fatigue. The intermediate level shows high cycle fatigue properties. The FML showed low cycles to failure for 80 %, 55 %, 40 % and 25 % of UTS and high scattering at 12 %. The cycles to failure were lower compared to FMEL at identical load levels. The failure was delamination due to the brittle interfaces compared to aluminum fracture and transverse matrx cracking in the FMEL.

The highest load level of 80 % resulted in high scattering, which was attributed to the load being close to the tensile strength of the laminate. The scattering resulted in an inaccurate prediction of the laminate properties, as the failure mechanisms were difficult to predict due to high load.

Damage detection

To monitor damage of the FMEL specimens, experiments were conducted, where the specimens were scanned in the CT after every 1000 cycles. The CT-scans were used to detect damage in the laminate to find a correlation to the mechanical performance. Additionally, thermal imaging was used as a damage detection method to find temperature differences on the laminate surface, which were called hot spots. Since a locally higher load could have been caused by damage in the laminate, the temperature increase due to higher internal friction of the polymer could be detected.
The laminate was scanned before application of the fatigue load to generate a reference scan. The option to virtually remove every layer to show only the damaged layer was used to detect damage. The detection of aluminum cracks, although in the core layer of the laminate was possible. The non-destructive damage detection allowed a series of experiments, where the fatigue loading could be applied and the damage could be visualized at various stages. The damage evolution process in the laminate then could be used to interpret the mechanical data obtained from the fatigue experiments.

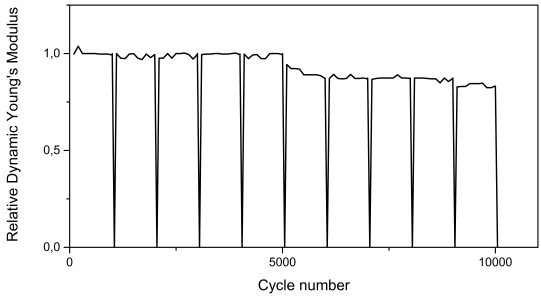

Figure 5.61: Relative dynamic stiffness of FMEL at 55 % of UTS with repeated unloading for CT-scanning every 1000 cycles [150]

Figure 5.61 shows the relative dynamic stiffness of an FMEL specimen at 55 % of UTS, which was scanned after every 1000 cycles without external load. The relative dynamic modulus degraded during the fatigue experiments, showing the behavior monitored in the continuous fatigue experiments. The cycle numbers of the CT-scans are indicated by a stiffness of 0, because the specimen was dismounted and transferred into the CT.
The initial stiffness of the specimen did not significantly change until 5000 cycles were reached, where a significant stiffness drop occurred. The stiffness drop was sharp, and the damage to the aluminum layer in the laminate was detected using the CT-scans visualized in figure 5.62. After the initial stiffness drop, the stiffness showed a slight but constant decrease.

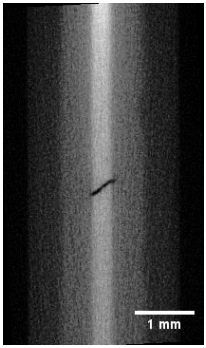

Figure 5.62: As-detected crack in the aluminum constituent of the FMEL fatigue specimen after 7000 cycles

Figure 5.62 shows the laminate with the lightest grey representing the aluminum core layer, the intermediate grey is the elastomer interlayer and the darkest grey is the CFRP face sheets. The image shows the fractured aluminum core layer, which correlated with a sharp stiffness decrease measured in the fatigue experiments. It is also visible, that the elastomer interlayer was not affected by the crack. It did not let the crack propagate further, but restricted it to the aluminum layer.

The stiffness decrease visible in figure 5.61 could be correlated to the fractured aluminum layer in the CT-scan, which additionally enabled the validation of the lifetime prediction for the aluminum constituent, because the exact cycles to failure of the aluminum in the FMEL could be measured.

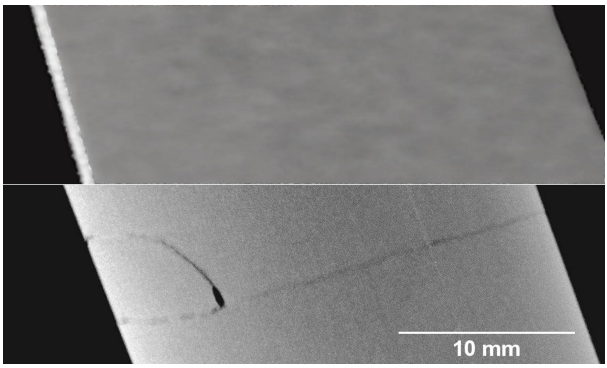

Figure 5.63: CT-scan of the intact aluminum constituent of a fatigue specimen after 5000 cycles (top) and fractured layer after 7000 cycles (bottom) at 55 % UTS

In order to visualize the whole crack in the aluminum, the aluminum core layer was extracted and visualized using Avizo. The aforementioned 5-layer laminate could be virtually disassembled into the constituents, which enabled the visualization of the sole aluminum core layer. The aluminum layer without the elastomer and CFRP is presented in figure 5.63 and shows the layer before and after the crack propagated through the aluminum constituent. The crack was perpendicular to the loading direction through the thickness and width of the fatigue specimen fully separating the aluminum layer into two segments.

Figures 5.64 (a) - (d) show the temperature of a fatigue specimen at 80 % of UTS. The maximum, average and minimum temperature is visualized. Figure 5.64 (a) shows the specimen before loading and therefore setting the

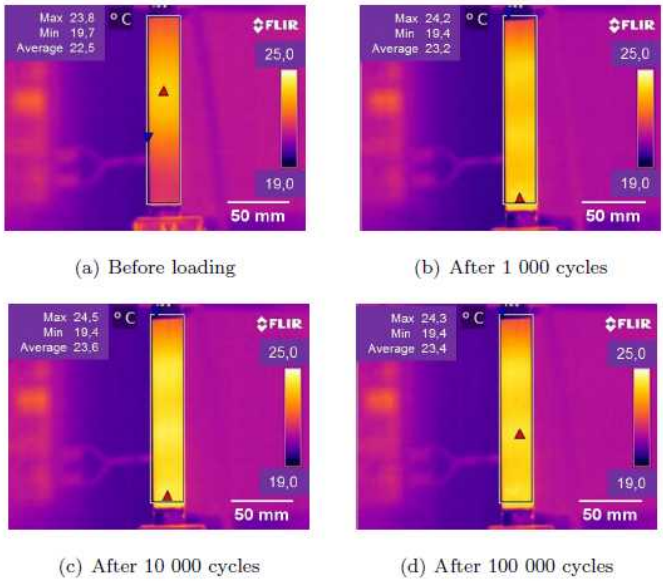

Figure 5.64: Thermal images of the fatigue specimen at 80 % of UTS before loading (a), after 1 000 cycles (b), after 10 000 cycles (c) and after 100 000 cycles (d) [150]

reference temperature. In (b) the specimen had a higher temperature due to the friction in the polymer of the FRP and elastomer constituents. The maximum temperature only rose 0.4 °C in the first 1000 cycles. After 10 000 cycles figure (c) showed a non homogeneous temperature distribution, which was at the maximum 0.9 °C higher than the average specimen temperature. The last picture shows the hot spots the best on the specimen. The images prove the temperature increase being below the threshold, but also inhomogeneous temperature distributions are visible, which indicated damage.

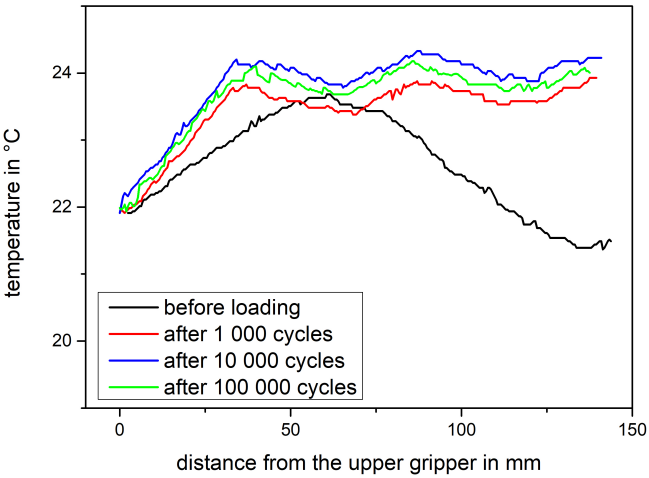

Figure 5.65: Temperature distribution over the length of the specimen before loading, after 1 000, 10 000 and 100 000 cycles

Figure 5.65 presents the temperature distribution of the fatigue specimen over the length. The temperature before loading shows a peak in the center and lower temperatures close to the grippers, which could have caused initial cooling due to high thermal conductivity. After 1 000 cycles, the average temperature was increased in the specimen and three temperature peaks are found on the specimen. The specimen exhibited the identical characteristics after 10 000 cylces and 100 000 cylces. The temperature was highest with 24.1 °C after 10 000 cylces. The three temperature peaks in the specimen were consistent throughout the experiment and are also visualized with enhanced contrast in figure 5.66.

Figure 5.66 shows the identical image as in figure 5.64 (d) with an enhanced contrast. The difference in temperature is clearly visible and three hot-spots could be defined, where damage was assumed within the laminate.

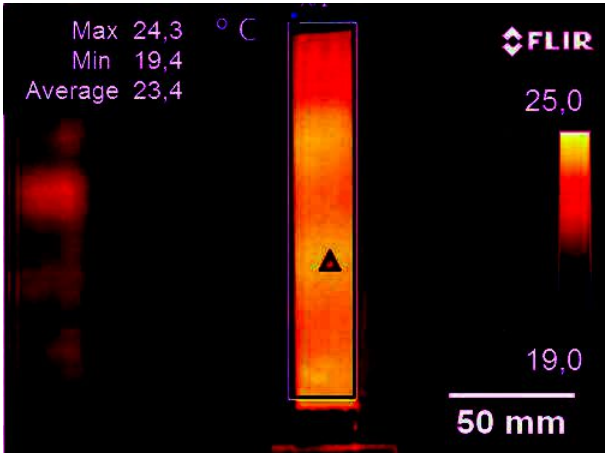

Figure 5.66: Thermal image of an FMEL fatigue specimen at 80 % of UTS after 100 000 cycles [150]

The locations on the specimen were marked and the specimen was analyzed in the CT. At every hot-spot an aluminum fracture was detected like in figure 5.63, proving the thermal measurements worthy of detecting damage during the experiment.

5.5.2 Lifetime prediction

The lifetime prediction for the laminate was conducted by superposition of lifetime predictions for the constituents under the constraint of an intact interface and iso-strain distribution. It was assumed, that the elastomer interlayer would not fail, because the high strain to failure of approximately 200 % would not be reached during fatigue experiments. Additionally it was assumed, that a fracture or reduction in load bearing capacity of one constituent would result in a stress redistribution according to the revised stiffness for the other constituents.

For example would an aluminum fracture result in 100 % of the load being transferred into the CFRP and elastomer constituent, which would be calculated by iso-strain assumption and the current stiffness of each constituent. Likewise would a stiffness degradation in the CFRP constituent lead to higher stresses in the aluminum layer and elastomer layer. The exact amount of load was calculated by an iso-strain assumption with the current stiffness of the constituents.
The lifetime prediction for FMEL and FML was identical, as the load bearing constituents were identical and an intact interface was assumed.

Aluminum

The lifetime prediction for the aluminum constituent was carried out according to Coffin-Manson. The data sheet of the aluminum showed that the constituent would fail due to low cycle fatigue [130].

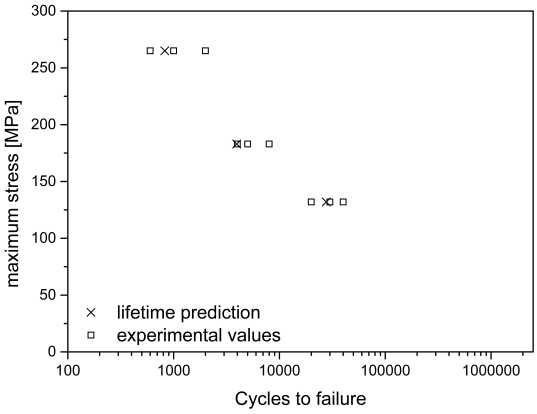

Figure 5.67: Lifetime prediction and experimental values for the aluminum constituent in the FMEL according to the Coffin-Manson

The aluminum fracture in fatigue experiments could be detected and therefore the lifetime prediction of the constituent could be validated with experiments. The aluminum fracture in the FML occurred after delamination and failure, leaving only the FMEL fractures to be compared to the prediction.
The lifetime prediction of the aluminum constituent and the experimentally obtained values are presented in figure 5.67. The lifetime prediction, marked with an x, fit the experimental values, marked with squares, very well. The aluminum failure was detected in the fatigue experiment, due to the characteristic change in laminate stiffness described in section 5.5.1, which enabled a correlation of the fracture and the cycle number from the fatigue experiment. The failure of the aluminum caused a stiffness reduction, which did not meet the failure criterion of the laminate. Therefore, the load carried by the aluminum was redistributed into the CFRP and elastomer layers. Thus, the fatigue properties of the CFRP component defined the cycles to failure of the laminate. At the predicted cycle to failure of the aluminum, the load was recalculated to define the remaining lifetime of the CFRP with the additional load previously carried by the aluminum layer.

CFRP

The prediction of the CFRP component was based on research from Ogin et al. [105], which predicted the lifetime for biaxially oriented unidirectional glass fiber reinforced polymer laminates. The application of the lifetime prediction for CFRP was proven by Berthelot et al., who analyzed GFRP and CFRP to find the matrix dominated stiffness decrease was invariant of the fiber [104]. The stiffness reduction was based on matrix cracks in the transverse layers. Likewise to Ogin et al. the stiffness reductions were monitored and the data fed into diagram 5.68.
Since the cycles to failure for the aluminum were already known, the stress hereafter was recalculated and the prediction for the CFRP was altered, so that the resulting prediction was applicable for the whole laminate.

Laminate

The laminate prediction was a superposition of lifetime predictions of the aluminum constituent and the CFRP constituent. The aluminum fracture was calculated into the CFRP lifetime prediction. The failure criterion for the whole laminate was then used to calculate the laminate lifetime prediction.

A diagram accounting for the stiffness reduction per cycle depending on the stress amplitude and the relative stiffness was used to define an average stiffness reduction. The stiffness reduction values are plotted in figure 5.68 indifferent of the load levels. The diagram connects the stiffness degradation with the maximum stress applied to the specimens. The resulting data points should follow a straight line in the double logarithmic diagram. The line can be fitted and the variables A and n can be taken from the equation for the line. The resulting line defines an average stiffness reduction per cycle depending on the load and current stiffness of the laminate, which can be used to calculate the cycles to failure for the laminate.

The variables A and n obtained from the fitted line in figure 5.68 were used in equation 5.2.

$$-\frac{1}{E_0}\frac{dE}{dN} = A\left[\frac{\sigma_{max}^2}{E_0^2(1-E/E_0)}\right]^n \tag{5.2}$$

The variables were put into the equation 5.2, which connected the change in stiffness per load cycle $\frac{dE}{dN}$ divided by the initial stiffness E_0 with the constant A, the maximum stress squared σ_{max}^2, the current stiffness E with the initial stiffness E_0 and the exponent n. The equation was integrated to obtain the relation between the current stiffness and the cycles to failure presented in equation 5.3.

$$\frac{E}{E_0} = 1 - \left(46.5 * (\frac{\sigma_{max}}{E_0})^{1.6} * N^{0.2}\right)^n \tag{5.3}$$

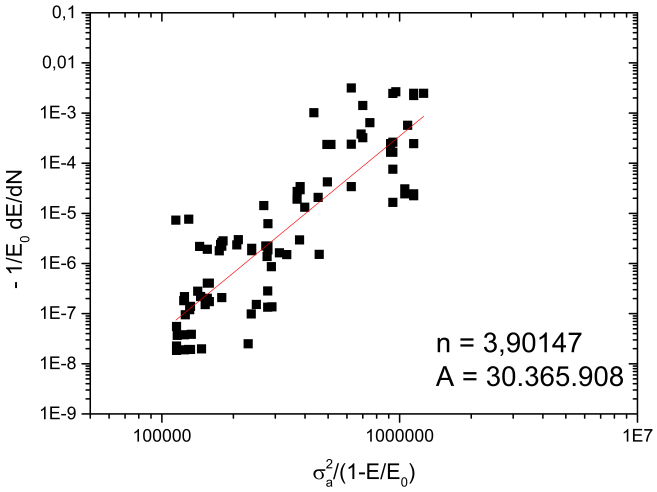

Figure 5.68: Stiffness reduction versus stress amplitude diagram of the CFRP in the laminate to generate values for the calculation of the lifetime prediction

The integrated equation was used to find the connection between the maximum stress and the cycle number for the given failure criterion as shown in equation 5.4. The current dynamic stiffness at failure was 80 % of the initial value and the cycles to failure could be calculated from the equation to generate the lifetime prediction shown in figure 5.69.

$$\sigma_{max} = \frac{823,3}{N^{0,128}} \tag{5.4}$$

Figure 5.60 shows the lifetime prediction of the laminates obtained by superposition of constituents' lifetime predictions and the correlating experimental fatigue results. The lifetime prediction presented in black fit the experimental results of the FMEL rather conservatively.

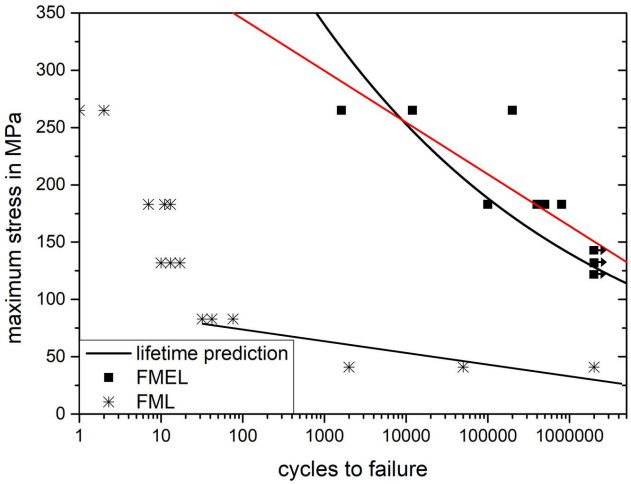

Figure 5.69: Fatigue life prediction and S-N curves for both laminates with data points from fatigue experiments [150]

The FML did not fit the lifetime prediction, as the failure due to delamination could not be monitored. The prediction was used for both laminates, as the load bearing constituents were identical. However, the difference in failure mechanism resulted in a big difference for the experiment and prediction for the FML. The distance of the data points to the lifetime prediction present the severity of the premature failure. The lifetime prediction could not be adapted to include delamination for the brittle interfaces.

The experimental properties show that the fatigue endurance limit was higher than the lowest loads tested at 40 % of UTS. However, the prediction did indicate, that the specimens should meet the failure criterion before reaching $2x10^6$ load cycles. Because the prediction was conservative, the laminates still had a relative stiffness of 82 % to 85 %, which resulted in a small difference of prediction and experiment.

5.5.3 Thermal mechanical fatigue properties

Thermal mechanical fatigue was carried out in tension-tension fatigue coupled with a thermal cycle from 10 °C to 80 °C. The cycle duration for one load and thermal cycle was 188 s. The failure criterion was also stiffness reduction of 20 %. The temperature and mechanical load were in phase in the experiments, while the fatigue endurance was defined at 1000 cycles.

Results of the thermal mechanical fatigue experiments

The load scheme of the thermal and mechanical load is presented in figure 4.17. The thermal load was generally conducted between 10 °C and 80 °C, while the mechanical load was conducted at the strain levels corresponding with 80 %, 55 %, 40 % and 25 % of UTS. A load level at 12 % of UTS was added for the FML specimens. The stiffness evolution of the FMEL specimens at 55 % and 40 % during the TMF experiments as well as FML at 25 % is presented in figure 5.70.
The curves of the FMEL specimen showed the stiffness degradation during TMF experiments and the failure criterion. The relative stiffness of 55 % of UTS decreased from the first cycle until failure, while the 40 % specimen had a constant stiffness for the first 30 cycles before the degradation started. The stiffness decrease was more significant with the higher load level, while the small stiffness degradation of the 40 % led to failure shortly before 1000 cycles. The higher load led to a stiffness decrease and the failure criterion was met at 17 cycles. The FML showed a sudden decrease after 20 cycles at 25 % of UTS. The stiffness decrease due to delamination was sharp and led to instant failure.

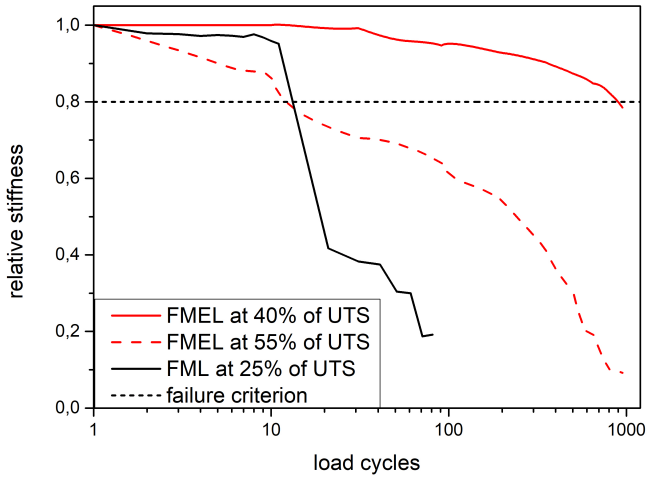

Figure 5.70: Diagram of the relative stiffness evolution of FML and FMEL during the TMF experiments against the failure criterion

Figure 5.71 shows the S-N curve for FMEL and FML under thermal mechanical fatigue loading using 50 % average performance S-N curve. Data points at identical cycles to failure and load levels were stacked to visualize the multitude of points, but the load was only varied in five levels. The experimental data is visualized figure 5.71 showing the results of the experiments. The thermal mechanical fatigue endurance limit of FMEL was above 25 %; therefore the load level was omitted.

The FML data points were marked with the asterisks and the failure occurred instantly in the load levels of 80 %, 55 % and 40 % of UTS. At 25 % of UTS the lifetime of the specimens was low and at 12 % the TMF performance of the laminate could be evaluated. The FML exhibited delamination as a premature failure like in the fatigue experiments.

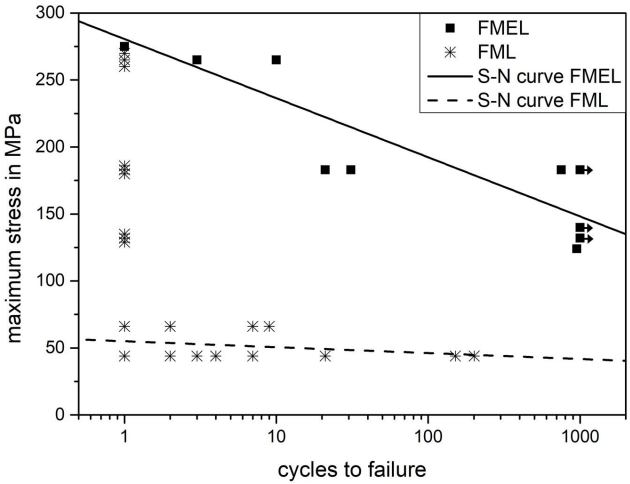

Figure 5.71: Diagram of the average load bearing capability of FMEL and FML and the experimental values of thermal mechanical fatigue

5.5.4 Discussion of the fatigue experiments and prediction

Fatigue The fatigue experiments of the FMEL showed a high fatigue endurance limit; because the lowest load level advised by the standard could be omitted [100]. The failure mechanism shown in the experiments, aluminum fracture and stiffness decrease in the CFRP constituent, showed that the elastomer interlayer remained intact throughout the experiment. The elastomer enabled load transfer from one constituent to another and compensated the difference in stiffness. The interfacial properties remained sufficient to prevent delamination and retain structural integrity of the laminate.
The failure of FML lacking the elastomer interlayer was delamination in the first cycles due to the difference in stiffness, which caused interfacial strain. The FML could be evaluated using a lower load level of 12 % of UTS.

The interfacial properties of the FML prevented high fatigue properties, as the strain induced by the experiment could not be balanced by the interface. Failure was initiated by delamination even at the lowest load level.
The elastomer, which itself had low stiffness and strength, increased the properties of the FML. The interlayer allowed relative displacement, which allowed the FMEL to remain intact after an aluminum fracture. The crack in the aluminum could not propagate into the elastomer and was confined to the aluminum layer, which was shown by the CT images. The resulting lifetime of the CFRP was enabled by the intact elastomer layer. The properties of the FML were increased by at least three decades due to the elastomer interlayer.
The comparison of the mechanical properties to GLARE showed that the fatigue in GLARE was conducted on notched specimens. The highest applied stress on GLARE for crack propagation at 140 MPa is comparable to the specimens below the fatigue endurance limit at 132 MPa.
The failure in the FMEL occurred without specimen separation, but through a stiffness decrease. The failure could be viewed as damage tolerant, because aluminum fracture did not cause the laminate to fail and sudden failure did not occur like in the FML. The FML failure occurred spontaneously at delamination, which caused the specimen to lose structural integrity. The FML showed a high scatter at the 12 % load level accounting for the brittle, spontaneous failure. The fatigue performance of the FML was significantly lower due to the lack of the elastomer interlayer and brittle interface.

Damage detection The damage detection using CT-scans could correlate the sharp stiffness drops with the aluminum fracture and enabled the detection of aluminum fracture during the fatigue experiment by monitoring the stiffness.
The sharp stiffness drop in the fatigue experiments could be correlated by the ex-situ CT-scans with the aluminum fracture. The intact aluminum layer was visualized in the top image of figure 5.63 before the stiffness dropped.

The aluminum after the stiffness reduction was presented in the lower image showing a crack through the aluminum layer. The crack was correlated to the change in stiffness, which enabled the characteristic stiffness drop to indicate fractured aluminum.

The detection of aluminum fracture in the experiment was used to validate the aluminum lifetime prediction. Carbon fiber and matrix cracking was not visible in the CT, as the fiber and crack was too small for the resolution of the system. The detector resolution of 2048 pixel x 2048 pixel and the specimen width of 25 mm defined in ISO 13003 [100] resulted in an optimum resolution of 12.2 μm/pixel. This resolution would not detect a single carbon fiber with a diameter of 7 μm. Also did the laminate cause beam hardening which overshadowed the absorption difference between carbon fibers and epoxy matrix. Stiffness degradation due to fiber and matrix cracking can only be researched with smaller specimens, which increased resolution. Jespersen et al. showed fiber and matrix fracture in small GFRP specimens [116]. However, in FML, fatigue was assessed with notched specimens, where the crack was visible from the surface [125].

Thermal imaging was used to detect hot spots on the specimen surface during the experiment. The hot-spots on the laminate were also correlated with the fractured aluminum using CT-scans. The indicated locations had increased stress in the CFRP layer due to the crack in the aluminum. The higher stress increased the internal friction and the temperature of the epoxy matrix. The correlation of hot spots with aluminum fracture allowed damage detection during the experiment.

The damage in the aluminum showed that the crack was held to the aluminum constituent. The high strains to failure of the elastomer combined with the good adhesive properties to the aluminum mastered the additional stress caused by the crack tip. The intact interfaces of the elastomer and the ability to stop cracks resulted in a lifetime of the laminate after initial failure and therefore a gradual failure mechanism.

Lifetime prediction The lifetime prediction for the laminates superimposed predictions for the individual constituents with the assumption of an iso-strain state throughout the experiments. The assumption was accurate for the FMEL specimens. The FML specimens, however, failed due to delamination and did not achieve the predicted cycles to failure.
The prediction of the aluminum constituent in the FMEL proved to be accurate, as the damage detection could define the aluminum fracture in the fatigue experiments. The values for the aluminum fracture agreed well with the predicted values using the Coffin-Manson prediction.
The CFRP prediction was integrated in the laminate prediction and was accurate as well. The prediction for the whole laminate was conservative but fit the experiments. The prediction technically allowed stresses higher than the tensile strength. Therefore, the prediction was reduced to stress values lower than the tensile strength of the laminate. The prediction underestimated the fatigue endurance limit of the laminate. Although the prediction was conservative, it fit the experimental values well.
The lifetime prediction did not represent the FML specimens, because the failure by delamination was not accounted for in the prediction. The premature failure significantly reduced the cycles to failure of the laminate. Therefore, the prediction was not applicable to the FML specimens.

TMF The TMF experiments could not be conducted with the desired thermal cycle from $-40\,^{\circ}\mathrm{C}$ to $80\,^{\circ}\mathrm{C}$ caused by excess heat produced by the peltier elements. Although an active cooling system with low temperatures was used to cool the peltier elements, lower temperatures could not be obtained. The thermal cycle duration and the high temperature achievable using the peltier elements was satisfactory.

The FMEL specimens showed lower properties in the TMF experiments compared to the fatigue experiments caused by the superimposed thermal load. The cycles to failure at 80 % of UTS were reduced to zero, while the cycles to failure at lower load levels were reduced by a factor of approximately 200. Since the thermal cycling without external load did not affect the FMEL specimens, the laminate suffered from the superposition of the loads. The identical load levels resulted in specimens reaching the fatigue endurance limit, however, the cycles to reach the limit were significantly lower. The thermal load reduced the cycles to failure of the laminates, which was indicated by the quasi-static experiments at $80\,^{\circ}\mathrm{C}$, which showed lower properties compared to ambient temperatures consistent for both laminates. The FML specimens showed consistent behavior with the fatigue performance, because only the 12 % of UTS load level resulted in significantly high cycles to failure. However, the cycles to failure were reduced by approximately the factor of 1000 at the identical load level due to the thermal load.

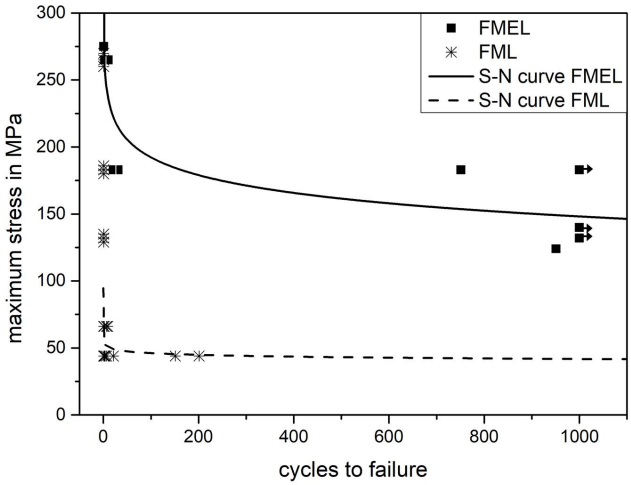

Figure 5.72: Diagram of the average logarithmic load bearing capability of FMEL and FML and the experimental values of thermal mechanical fatigue in a linear diagram

Figure 5.72 presents the identical diagram of TMF as in figure 5.71, but with a linear x-axis. The diagram better visualizes the small difference between the low cycles to failure. The FMEL exhibits a low performance at 80 % and high scatter at 55 %. The 40 % load level showed high properties.
The S-N curve for FML showed a low fatigue endurance limit for the FML. The FML specimens resulted in instant failure at 80 %, 55 %, 40 % and 25 %. Even at 12 % many data points were at low cycles to failure. The thermal cycling without external load of the FML already showed reduced properties at high cycle numbers increasing the damage detected in fatigue experiments. Additionally were the properties reduced in quasi-static experiments at elevated temperature. These two results combined with premature failure in fatigue experiments led to low TMF properties and the prominent benefit of the elastomer interlayer.

6 Discussion of the elastomer interlayer

The objective of this work was to examine, whether the FMEL would surpass the FML and how it would compete compared to the commercially available GLARE. The FML performance was determined from literature and also by FML specimens manufactured exactly like the FMEL to obtain comparable laminates. The elastomer interlayer altered the characteristics of the interface by changing the brittle nature to ductile fracture mechanisms. The interlayer also showed the possibility for increased properties especially concerning damping, corrosion and CTE-mismatch. The FMEL showed lower quasi-static properties than FML and GLARE, but the environmental experiments presented constant mechanical properties after thermal and corrosive loads. The mechanical properties of FML decreased drastically due to environmental loads proving the risk of combining CFRP with aluminum. The elastomer interlayer, reducing the mechanical properties, ensured applicability of the laminate.

In dynamic loadings the elastomer interlayer led to beneficial properties by preventing delamination. The Charpy energy of the FMEL doubled the FML properties due to the high strain to failure, although the bending properties of FML were higher. The failure of the FMEL remained identical to bending as the laminate failed due to tension and compression in the outer fiber. The failure of the FML changed from delamination to tension and compression failure of the entire CFRP layer. The failure of the FMEL was beneficial compared to the FML in Charpy experiments and also showed similar properties in the puncture experiments, where the FMEL only showed small delamination in the CFRP. The FML showed delamination of the hybrid interface and large parts of the CFRP layers.

The FML surpassed FMEL values, however, specimen clamping prevented delamination and FML properties could have been overestimated.
The damage tolerance of the laminates was examined using FML with thicker CFRP layers for identical axial moment of inertia. The damage to FML through impact tests was lower and the deflection was predicted with an error below 15 %. The FMEL showed more severe damage and the prediction had an error of 25 % caused by the lower stiffness of the elastomer. Subsequent CAI experiments showed damage to FML resulted in reduced mechanical properties due to delamination and compressive failure. The FMEL specimens did not delaminate and the effect of damage on the properties was lower. The elastomer layer prevented delamination, causing consistent mechanical properties after impact compared to FML.
The effect of the elastomer interlayer on the mechanical properties was exhibited in fatigue experiments, where the FMEL specimens showed failure due to aluminum fracture and stiffness degradation in the CFRP constituent. The FML specimens delaminated at identical load levels and presented premature failure. The fatigue endurance limit for the FMEL was 4 times higher than the limit for FML, as the elastomer interlayer prevented delamination after aluminum core layer fracture and distributed the load into the CFRP allowing the laminate cycles to failure to be reached after aluminum fracture and therefore extended the fatigue life of the laminate.
The thermal cycling, which damaged the FML without external load, and the fatigue properties resulted in low properties in TMF experiments. The interface, failing in fatigue experiments, was additionally thermally loaded and caused premature failure. The TMF endurance limit was increased by the factor of 4 through the elastomer interlayer. The elastomer layer enabled cycles to failure after aluminum fracture and prevented delamination.
The elastomer interlayer, reducing quasi-static properties, but enabled applicability by resistance to environmental loads led to higher FMEL properties in many dynamic and fatigue tests. The layer, which was not primarily load bearing, enhanced the mechanical properties in specific loads.

7 Conclusion

Materials selection and a process optimization were conducted for FMEL and FML with subsequent mechanical characterization. A variety of quasi-static experiments was followed by different dynamic tests leading to fatigue experiments. The effect of the elastomer interlayer was examined and described under different mechanical and environmental loading conditions.
The elastomer interlayer could be integrated into a manufacturing process using a machine press and the cycle time could be reduced to 150 s. The materials selection already showed, that the elastomer interlayer could solve problems arising from the combination of aluminum and CFRP, but would result in lower flexural stiffness compared to FML. The elastomer interlayer changed the interfacial properties to conduct a ductile behavior compared to the brittle interface of the FML. Lower mechanical properties caused by the elastomer interlayer were shown in tension, compression and bending.
The environmental loads showed that the elastomer interlayer could balance the CTE-mismatch and prevent corrosion, which caused a degradation of mechanical properties and delamination in FML, ensuring the applicability of the laminate through the interlayer.
The dynamic properties showed the benefit of the ductility of the elastomer interlayer starting with higher charpy energies and higher specific absorbed energies in the puncture test compared to the FML. The impact test showed good energy absorption properties of the FMEL at low levels, but extensive damage at higher loads. The FML showed in reduced mechanical properties in CAI experiments, when damage due to impact was visible, whereas the FMEL specimens showed more consistent behavior despite the more extensive damage in the impact tests.

The fatigue performance of FML was low due to premature delamination and resulted in four times lower fatigue endurance limit compared to the FMEL. The FMEL showed high fatigue endurance values and a well fitting lifetime prediction. Damage to the aluminum layer in the FMEL could be detected using CT-scans and thermal imaging. The FML showed similar behavior in the TMF experiments as in the fatigue experiments. Delamination occurred, which was aided by the additional loading of the interface due to the thermal cycling. The FMEL presentedö lower cycles to failure compared to the fatigue experiments due the thermal loads, but still presented a high fatigue endurance limit and gradual failure during the experiment.
The failure mechanism of FML was often delamination due to the brittle interface, while the elastomer interlayer presented good adhesive properties and the failure was caused by the constituents. The failure mechanisms in FMEL were frequently gradual, while the FML often failed suddenly.
The elastomer interlayer decreased the quasi-static properties, but ensured the application by solving the problems with environmental loads. The interlayer caused an increase in dynamic and fatigue properties and therefore, the integration of an elastomer interlayer can be beneficial.

8 Outlook

8.1 Elastomer layer thickness optimization

The elastomer layer, provided by Kraiburg Holding GmbH & Co. KG, had a minimum thickness of 0.5 mm. This thickness needed to be reduced to reach the optimum lightweight potential, as the load bearing capacity of the elastomer was lower than the other constituents. The reduction of the elastomer layer would result in a higher volume fraction of the high stiffness components in the laminate. The flexural stiffness of the laminate suffered from a high elastomer thickness, which could be optimized through thinner elastomer layers. Therefore a manufacturing process to reduce the elastomer thickness before curing was developed.

8.1.1 Manufacturing of thin elastomer layers

The reduction of the elastomer layer thickness was conducted through the objective to solve the uncured elastomer as in part (a) of figure 8.1, distribute it onto the aluminum layer visualized in (b), which would also function as a carrier material, and then evaporate the solvent in (c). The following stacking of the constituents (d) and manufacturing process in a press (d) was identical to the standard procedure in this work. The amount of elastomer in the process was defined by the resulting thickness of 0.1 mm. The solvent used for the elastomer was benzine. The amount of elastomer for the thin layers was calculated and cut from the thick layer. The elastomer was dissolved in benzine to obtain a well manageable solution.

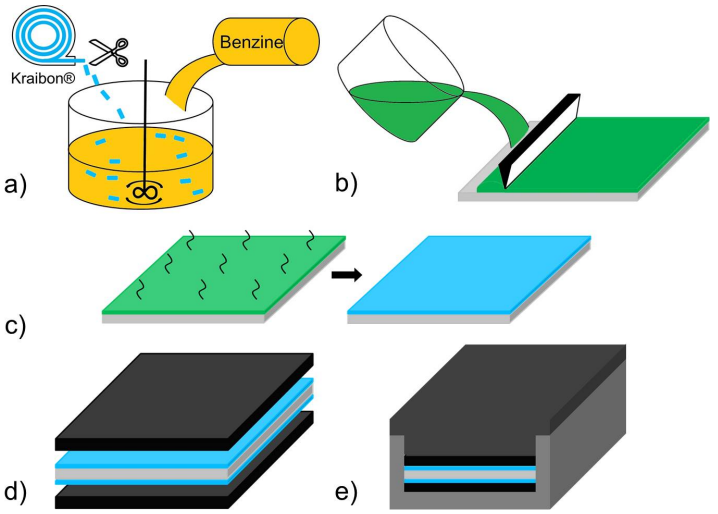

Figure 8.1: Schematic of the dissolution of elastomer in benzine (a), coating of the aluminum layer (b), evaporation of the benzine (c), stacking of the constituents (d), manufacturing of the laminate (e) [151]

The approximate elastomer content in the benzine was 16 %, because pretests showed that it was the perfect combination of adequate viscosity, so the solution could be spread on the metal layer, and solubility, where the elastomer could be dissolved entirely without chunks. The next step was to spread the solution on the metal sheet in a homogeneous layer. The metal acted as a substrate to carry the elastomer, which could not be handled without the metal substrate. The benzine was evaporated to obtain a pure elastomer layer with the same properties as the thick layer to receive comparable adhesive properties to the metal. The procedure was conducted for both sides of the metal sheet to generate the core layers of a symmetrical FMEL. The CFRP layers were added to the core layers and the manufacturing process was carried out.

The resulting laminate was desired to feature higher flexural properties compared to the standard FMEL, because the shear deformation of the elastomer layer would be reduced. Additionally was the volume content of the elastomer layer in the layer reduced, which also indicated higher properties.

8.1.2 Characterization of laminates with thin elastomer layers

The thin elastomer layers were distributed using a solvent and could impact the mechanical properties of the laminate. The extra manufacturing step could have altered the mechanical properties counteracting the higher lightweight potential. The adhesive interfacial properties were evaluated using edge shear tests, to detect changes in interfacial properties. The interface could have changed due to chemical reactions during the dissolution and by residual benzine in the interface, which could inhibit adhesion. The edge shear experiments were conducted like described in section 4.3.3 with a lower shear gap to account for the thinner interlayer.
The benefit of the lower volume fraction of elastomer in the laminate was determined using flexural experiments. The experiments were conducted like described in 4.4.3. The specimens were prepared using a Struers Accutom cutting machine with water cooling.

8.1.3 Results of the elastomer layer thickness optimization

The thickness optimization of the elastomer layer was conducted to increase mechanical properties especially the flexural stiffness. The optimization resulted in thinner laminates, because the CFRP and aluminum constituent thickness was kept constant to obtain comparable results. The laminate thickness was reduced to 1.7 mm instead of 2.5 mm due to the elastomer layer being reduced from 0.5 mm to 0.1 mm.

The specimens were tested by edge shear tests to investigate the adhesive properties of the elastomer and the possible change in behavior due to the solvent. Additionally flexural experiments were carried out to determine the increase in performance and describe the better lightweight potential.

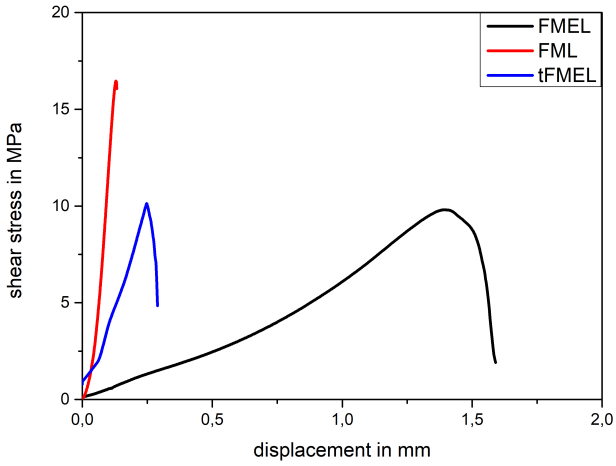

Figure 8.2: Curves of FMEL with standard and thin elastomer layers in the egde shear test [151]

Figure 8.2 shows the interfacial properties of the FMEL with reduced elastomer interlayers compared to the FMEL and FML laminates. The FMEL with thick interlayers shows a slightly higher shear strength and drastically higher shear energy compared to the FMEL with thin elastomer layers. The lower displacement caused by the thinner elastomer layer is visible in the diagram. The FML presents the highest shear strength and lowest displacement.

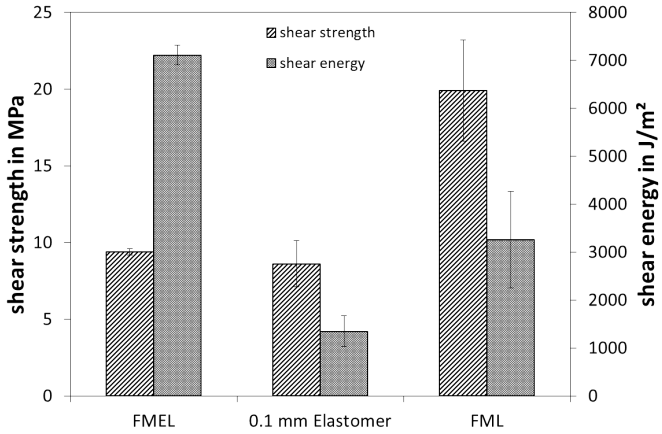

Figure 8.3: Interfacial properties of FMEL with standard and thin elastomer layers [151]

Figure 8.3 presents the interfacial properties of the the thin FMEL compared to FML and FMEL. The FML presented the highest shear strength with intermediate shear energy. The FMEL exhibited the highest shear energy and a slightly higher strength compared to the laminate with thin elastomer layers. The manufacturing process used for the reduced elastomer thickness using a solvent resulted could have impacted the adhesion and could be responsible for the reduction in shear strength. The shear strength of the elastomer layers is comparable in value, however the thin layer has a lower average strength and significantly higher scattering. The difference in shear energy is drastic, which originated from a large difference in displacement to failure. The thinner layer did not allow the deformation due to the lower thickness and therefore the shear energy resulted in lower values, which were about $1/5$ of the initial value. The FML presented higher shear energy compared to the thin FMEL caused by the higher shear strength.

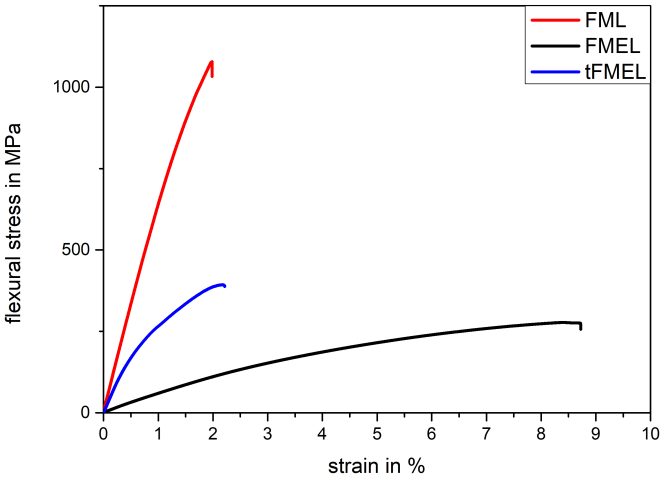

Figure 8.4: Flexural stress strain curves for FML, FMEL with standard and thin elastomer layers [151]

Figure 8.4 shows the flexural behavior of the thin FMEL compared to the laminates with thick elastomer interlayers and FML. The thinner elastomer layers result in a higher stiffness, lower strain to failure and a slight tendency for a higher strength compared to FMEL. The failure of the FMEL specimens did not differ due to the change in the interlayer showing the sufficient adhesion of both elastomer layers. The specimens all failed due to tension and compression failure in the outer fibers of the CFRP constituent.
The FML specimens exhibited higher flexural stiffness and strength compared to both FMEL laminates. The strain to failure was nearly identical to the FMEL with thin elastomer layers.

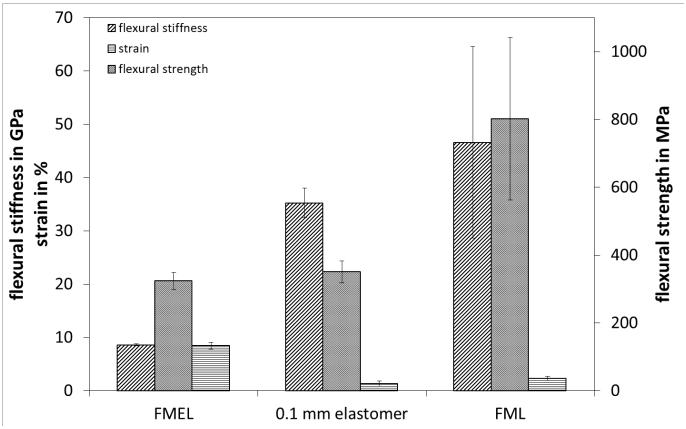

Figure 8.5: Flexural properties of FMEL with standard and thin elastomer layers [151]

Figure 8.5 presents the flexural properties of FML, FMEL and FMEL with thin elastomer interlayers. The FML showed the highest values in strength and stiffness with the highest scattering. The FMEL with thin elastomer layers had strength and stiffness properties between the FML and FMEL. Compared to the FMEL, the stiffness was increased by 300 % percent replacing the thick elastomer layer with the thinner version. However, the strain to failure was reduced by 84 % percent. Although the CTE-mismatch and corrosive properties of the thin layer were not proven, the lightweight potential exhibited by the thin elastomer layer was drastically increased compared to standard FMEL.

8.1.4 Discussion of the elastomer thickness optimization

The feasibility to manufacture laminates with thin elastomer interlayers was proven. Arising problems with residual solvent in the laminate could have resulted in slightly reduced interfacial properties. The process depositing the elastomer onto the aluminum sheet would need to be optimized and characterized regarding parameters influencing residual solvent before the manufacturing process could be reproduced with constant quality.The manufactured laminates showed comparable interfacial strength with increased scatter, which was attributed to the additional process step and possible residual solvent. The shear energy was significantly lower, which was due to lower deformations of the specimen. The thin layer was expected to reduce the shear energy, but increase the flexural stiffness.

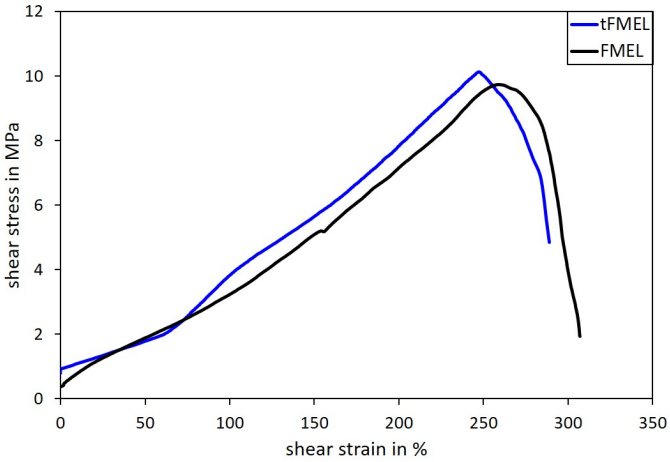

Figure 8.6: Stress strain curves for the standard and thin elastomer layer in the laminates in the edge shear test [151]

Figure 8.6 presents the stress-strain curves for the elastomer layers in the laminates. The FMEL with thin elastomer layers had lower displacements, but the data presented in figure 8.6 shows that the elastomer behaved consistently with the thick layer. The lower shear energy was reduced by a factor of five, as the thickness was reduced by the identical factor. Whether the beneficial impact of the elastomer layer on the dynamic and fatigue properties can be retained, although the shear energy is low, has to be proven in the future for the application of FMEL with thin elastomer layers.
The reduced thickness resulted in increased flexural stiffness but in lower deflection before failure occurred. The flexural stiffness was increased by 300 %, which was the intended result of the elastomer thickness reduction. The higher volume fraction of aluminum and CFRP lead to higher stiffness values and further reductions of the elastomer interlayer could result in significantly higher values.
The approximately constant values for the strength combined with the same failure mechanics show that the properties of the elastomer proved capable to prevent premature failure and good adhesion of both elastomer layers. The compression respectively tension failure of the outer CFRP fibers result in high flexural strength values. The strain to failure was reduced due to the lower elastomer thickness.

8.2 Forming of FMEL

Commercially available FML are only available in slightly curved sheets. Complex geometries could not be reached due to the manufacturing process. The Institute for Production Science (wbk) conducted experiments to form the laminates to small radii to prove the laminates can be formed at will in complex geometries.

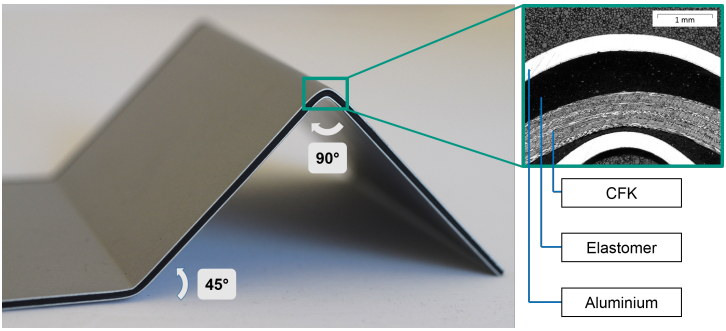

Figure 8.7: Formed FMEL with aluminum face sheets [128]

Figure 8.7 shows the results of the forming experiments and shows the laminate with angles of 45 ° and 90 ° within one laminate. The figure shows the first manufactured laminate, which had aluminum face sheets, because they were easier to manufacture due to the known forming characteristics of the face layer. Later standard laminates with CFRP face sheets were manufactured as well. The cross section polish at the right shows the difficulties, where the stiff carbon fibers displace the elastomer at the inner radius. The displacement of the elastomer can be viewed as an imperfection, however, the forming would not have worked without the elastomer allowing relative movement and a different radius in the CFRP. The FML would have had broken fibers and delamination in the radius.

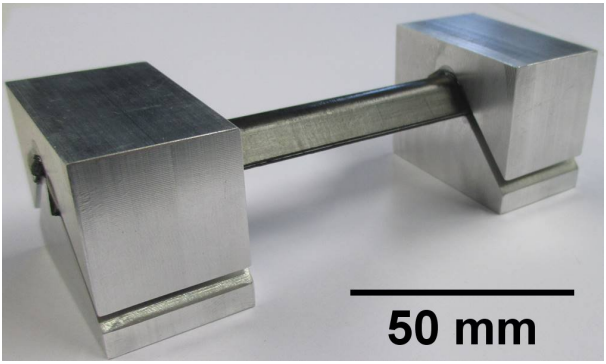

Figure 8.8: Specimen for the angular tension test [152]

Figure 8.8 presents the radius of the formed FMEL cut into specimen form to assess the properties of the laminate in the radius. The aluminum loading blocks were used to introduce load into the laminate.

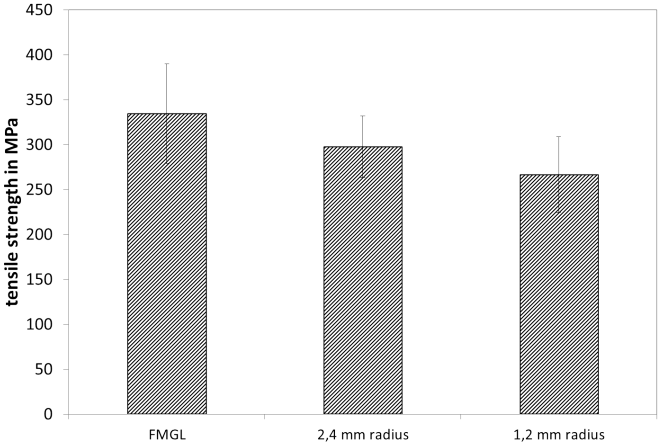

Figure 8.9: Mechanical properties of formed FMEL determined by angle tension test [152]

Figure 8.9 shows the mechanical properties of the FMEL and formed FMEL at two different radii. The specimens were cut out of the area, where the thickness and succession was disturbed. The angle tension test was used to determine the influence of the forming on the mechanical properties of the laminate. A clear reduction of tensile strength compared to FMEL can be seen, but the reduction is comparably low and shows the benefit of the elastomer balancing the laminate structure.

List of Figures

List of Tables

Bibliography

[1] L. B. Vogelesang and A. Vlot. Development of fiber metal laminates for advanced aerospace structures. *Journal of Materials Processing Technology*, (103):1–5, 2000.

[2] A. Vlot and J. W. Gunnink. *Fibre metal laminates / an introduction*. Springer Science & Business Media, Dordrecht, Netherlands, 2001.

[3] C. Vermeeren, T. Beumler, J. de Kanter, O. van der Jagt, and B. Out. Glare design aspects and philosophies. *Applied Composite Materials*, 10(4-5):257–276, 2003.

[4] J. J. Homan. Fatigue initiation in fibre metal laminates. *International Journal of Fatigue*, 28(4):366–374, 2006.

[5] A. Asundi and A. Choi. Fiber metal laminates: an advanced material for future aircraft. *Journal of Materials Processing Technology*, 63(1-3):384–394, 1997.

[6] R. C. Alderliesten and R. Benedictus. Fiber/metal composite technology for future primary aircraft structures. *Journal of Aircraft*, 45(4):1182–1189, 2008.

[7] F. Henning and E. Moeller. *Handbuch Leichtbau: Methoden, Werkstoffe, Fertigung*. Hanser, München, 2011.

[8] R. G. Pettit. Fiber/metal laminate. US Patent 5,227,216, 1993.

[9] C. Vermeeren. An historic overview of the development of fibre metal laminates. *Applied Composite Materials*, 10(4-5):189–205, 2003.

[10] A. Luukkonen, E. Sarlin, V. Villman, M. Hoikkanen, M. Vippola, M. Kallio, J. Vuorinen, and T. Lepistö. Heat generation in dynamic loading of hybrid rubber-steel composite structure. *Proceedings of 17th International Conference on Composite Materials, Edinburgh, Scotland*, pages 27–31, 2009.

[11] P. Cortes and W. J. Cantwell. The tensile and fatigue properties of carbon fiber-reinforced peek-titanium fiber-metal laminates. *Journal of reinforced plastics and composites*, 23(15):1615–1623, 2004.

[12] W.-X. Wang, Y. Takao, and T. Matsubara. Galvanic corrosion-resistant carbon fiber metal laminates. *Proceedings of the 16th International Conference on Composite Materials, Kyoto, Japan*, pages 8–13, 2007.

[13] C. T. Lin, P. W. Kao, and M.-H. R. Jen. Thermal residual strains in carbon fibre-reinforced aluminium laminates. *Composites*, (25):303–307, 1994.

[14] M. Verbruggen. *Aramid reinforced aluminium laminates: Arall: adhesion problems and environmental effects. Volume A: Adhesion and delamination*. Doctoral thesis, TU Delft, Netherlands, 1987.

[15] R. Rodi. *The residual strength failure sequence in fibre metal laminates*. Doctoral thesis, TU Delft, Netherlands, 2012.

[16] T. Beumler. *Flying Glare*. Doctoral thesis, TU Delft, Netherlands, 2004.

[17] J. Sinke. Manufacturing of glare parts and structures. *Applied composite materials*, 10(4-5):293–305, 2003.

[18] T. de Jong. *Forming of laminates*. Doctoral thesis, TU Delft, Netherlands, 2004.

[19] R. Alderliesten and R. Benedictus. Aircraft wing and fiber metal laminate forming part of such an aircraft wing. US Patent 9,636,891, 2017.

[20] G. Wu and J.-M. Yang. The mechanical behavior of glare laminates for aircraft structures. *JOM*, 57(1):72–79, 2005.

[21] R. Marissen. Fatigue crack growth in arall: A hybrid aluminium-aramid composite material: Crack growth mechanisms and quantitative predictions of the crack growth rates. *TU Delft, Netherlands, Faculty of Aerospace Engineering, Report LR-574*, 1988.

[22] P. Eyerer, T. Hirth, and P. Elsner. *Polymer engineering: Technologien und Praxis*. Springer Verlag, Berlin Heidelberg, 2008.

[23] P. Cortés and W. J. Cantwell. Interfacial fracture properties of carbon fiber reinforced peek/titanium fiber-metal laminates. *Journal of materials science letters*, 21(23):1819–1823, 2002.

[24] R. van Rooijen. *Bearing strength characteristics of standard and steel reinforced GLARE*. Doctoral thesis, TU Delft, Netherlands, 2006.

[25] D. W. Rhymer and W. S. Johnson. Fatigue damage mechanisms in advanced hybrid titanium composite laminates. *International Journal of Fatigue*, 24(9):995–1001, 2002.

[26] R. Alderliesten, C. Rans, and R. Benedictus. The applicability of magnesium based fibre metal laminates in aerospace structures. *Composites Science and Technology*, 68(14):2983–2993, 2008.

[27] G. Lucchetta, F. Marinello, and P. F. Bariani. Aluminum sheet surface roughness correlation with adhesion in polymer metal hybrid overmolding. *CIRP Annals-Manufacturing Technology*, 60(1):559–562, 2011.

[28] F. Bouquet, J. M. Cuntz, and C. Coddet. Influence of surface treatment on the durability of stainless steel sheets bonded with epoxy. *Journal of adhesion science and technology*, 6(2):233–242, 1992.

[29] G. Roebroeks. Fibre-metal laminates: recent developments and applications. *International Journal of Fatigue*, 16(1):33–42, 1994.

[30] A. Vlot, E. Kroon, and G. La Rocca. Impact response of fiber metal laminates. *Key Engineering Materials*, 141:235–276, 1998.

[31] A. Vlot. *Low-velocity impact loading on fibre-reinforced aluminium laminates (ARALL) and other aircraft sheet materials*. TU Delft, Netherlands, Faculty of Aerospace Engineering, Report LR-718, 1993.

[32] M. Kawai, M. Morishita, S. Tomura, and K. Takumida. Inelastic behavior and strength of fiber-metal hybrid composite: Glare. *International Journal of Mechanical Sciences*, 40(2):183–198, 1998.

[33] R. C. Alderliesten, M. Hagenbeek, J. J. Homan, P. A. Hooijmeijer, T. J. de Vries, and Vermeeren, C. A. Fatigue and damage tolerance of glare. *Applied Composite Materials*, 10(4):223–242, 2003.

[34] R. Alderliesten. *Fatigue crack propagation and delamination growth in Glare*. Doctoral thesis, TU Delft, Netherlands, 2005.

[35] J. Schijve, H. T. van Lipzig, G. F. van Gestel, and A. H. Hoeymakers. Fatigue properties of adhesive-bonded laminated sheet material of aluminum alloys. *Engineering Fracture Mechanics*, 12(4):561–579, 1979.

[36] J. F. Laliberte, C. Poon, P. V. Straznicky, and A. Fahr. Post-impact fatigue damage growth in fiber–metal laminates. *International Journal of Fatigue*, 24(2):249–256, 2002.

[37] E. C. Botelho, R. A. Silva, L. C. Pardini, and M. C. Rezende. A review on the development and properties of continuous fiber/epoxy/aluminum hybrid composites for aircraft structures. *Materials Research*, 9(3):247–256, 2006.

[38] E. C. Botelho, R. S. Almeida, L. C. Pardini, and M. C. Rezende. Influence of hygrothermal conditioning on the elastic properties of carall laminates. *Applied Composite Materials*, 14(3):209–222, 2007.

[39] W. J. Cantwell. The mechanical properties of fibre-metal laminates based on glass fibre reinforced polypropylene. *Composites Science and Technology*, 60(7):1085–1094, 2000.

[40] E. Sarlin. Characterisation of novel corrosion resistant stainless steel/rubber/composite hybrid structures. *Doctoral Thesis, Tampere University of Technology, Finland, Publication 1208*, 2014.

[41] E. Sarlin, M. Hoikkanen, L. Frisk, J. Vuorinen, M. Vippola, and T. Lepistö. Ageing of corrosion resistant steel/rubber/composite hybrid structures. *International Journal of Adhesion and Adhesives*, 49:26–32, 2014.

[42] E. Sarlin, Y. Liu, M. Vippola, M. Zogg, P. Ermanni, J. Vuorinen, and T. Lepistö. Vibration damping properties of steel/rubber/composite hybrid structures. *Composite Structures*, 94(11):3327–3335, 2012.

[43] M. F. Ashby. *Materials Selection in Mechanical Design: Das Original mit Übersetzungshilfen*. Spektrum Akademischer Verlag, München, thrid edition, 2007.

[44] J. Van Campen. *Optimum lay-up design of variable stiffness composite structures*. Doctoral thesis, TU Delft, Netherlands, 2011.

[45] I. Şen. *Lay-up Optimisation of Fibre Metal Laminates*. Doctoral thesis, TU Delft, Netherlands, 2015.

[46] F. Sket, R. Seltzer, J. M. Molina-Aldareguia, C. Gonzalez, and J. Llorca. Determination of damage micromechanisms and fracture resistance of glass fiber/epoxy cross-ply laminate by means of x-ray computed microtomography. *Composites Science and Technology*, 72(2):350–359, 2012.

[47] P. Schilling, B. Karedla, A. Tatiparthi, M. Verges, and P. Herrington. X-ray computed microtomography of internal damage in fiber reinforced polymer matrix composites. *Composites Science and Technology*, 65(14):2071–2078, 2005.

[48] B. Yu, R. Blanc, C. Soutis, and P. J. Withers. Evolution of damage during the fatigue of 3d woven glass-fibre reinforced composites subjected to tension–tension loading observed by time-lapse x-ray tomography. *Composites Part A: Applied Science and Manufacturing*, 82:279–290, 2016.

[49] G. Lawcock, L. Ye, Y.-W. Mai, and C.-T. Sun. The effect of adhesive bonding between aluminum and composite prepreg on the mechanical properties of carbon-fiber-reinforced metal laminates. *Composites Science and Technology*, 57(1):35–45, 1997.

[50] S. de Freitas and J. Sinke. Test method to assess interface adhesion in composite bonding. *Applied Adhesion Science*, 3(1):9, 2015.

[51] H. Truong, M. Martinez, O. Ochoa, and D. Lagoudas. An investigation on hybrid interface using on-line monitoring experiment and finite element analyses. *Proceedings of the 20th International Conference on Composite Materials, Copenhagen, Denmark*, pages 1359–1371, 2015.

[52] E. Sarlin, E. Heinonen, J. Vuorinen, M. Vippola, and T. Lepistö. Adhesion properties of novel corrosion resistant hybrid structures. *International Journal of Adhesion and Adhesives*, 49:51–57, 2014.

[53] E. Sarlin, M. Apostol, M. Lindroos, V-T Kuokkala, J. Vuorinen, T. Lepistö, and M. Vippola. Impact properties of novel corrosion resistant hybrid structures. *Composite Structures*, 108:886–893, 2014.

[54] A. Puck. *Festigkeitsanalyse von Faser-Matrix-Laminaten: Modelle für die Praxis*. Hanser, München, 1996.

[55] K. L. Reifsnider, editor. *Damage in Composite Materials: Basic Mechanisms, Accumulation, Tolerance, and Characterization*, volume 775. ASTM International, West Conshohocken, USA, 1982.

[56] S. E. Moussavi-Torshizi, S. Dariushi, M. Sadighi, and P. Safarpour. A study on tensile properties of a novel fiber/metal laminates. *Materials Science and Engineering: A*, 527(18):4920–4925, 2010.

[57] J. G. Carrillo and W. J. Cantwell. Scaling effects in the tensile behavior of fiber-metal laminates. *Composites Science and Technology*, 67(7):1684–1693, 2007.

[58] C. Schultheisz and A. Waas. Compressive failure of composites, part i: testing and micromechanical theories. *Progress in Aerospace Sciences*, 32(1):1–42, 1996.

[59] J. J. Remmers and R. de Borst. Delamination buckling of fibre–metal laminates. *Composites Science and Technology*, 61(15):2207–2213, 2001.

[60] M. Weiss, B. Rolfe, M. Dingle, and J. Duncan. Elastic bending of steel-polymer-steel (sps) laminates to a constant curvature. *Journal of applied mechanics*, 73(4):574–579, 2006.

[61] DIN 65148:1986-11. Prüfung von faserverstärkten kunststoffen; bestimmung der interlaminaren scherfestigkeit im zugversuch. 1986.

[62] S. Hinz, T. Omoori, M. Hojo, and K. Schulte. Damage characterization of fiber metal laminates under interlaminar shear load. *Composites, Part A: Applied Science and Manufacturing*, 40(6):925–931, 2009.

[63] J. W. Cook, S. Edge, and D. E. Packham. The adhesion of natural rubber to steel and the use of the peel test to study its nature. *International Journal of Adhesion and Adhesives*, 17(4):333–337, 1997.

[64] K. Weidenmann, L. Baumgärtner, and B. Haspel. The edge shear test - an alternative testing method for the determination of the interlaminar shear strength in composite materials. *Materials Science Forum*, 825:806–813, 2015.

[65] M. Hagenbeek. *Characterisation of fibre metal laminates under thermomechanical loadings*. Doctoral thesis, TU Delft, Netherlands, 2005.

[66] G. Zhu, Y. Xiao, Y. Yang, J. Wang, B. Sun, and R. Boom. Degradation behavior of epoxy resins in fibre metal laminates under thermal conditions. *Journal of Shanghai Jiaotong University (Science)*, 17(3):257–262, 2012.

[67] A. Vlot, T. Soerjanto, I. Yeril, and J. A. Schelling. Residual thermal stresses around bonded fibre metal laminate repair patches on an aircraft fuselage. *Proceedings of the 41st SAMPE Symposium, Oak Ridge, USA*, pages 888–903, 1998.

[68] J. Xue, W.-X. Wang, Y. Takao, and T. Matsubara. Reduction of thermal residual stress in carbon fiber aluminum laminates using a thermal expansion clamp. *Composites Part A: Applied Science and Manufacturing*, 42(8):986–992, 2011.

[69] B. Müller, S. Teixeira De Freitas, and J. Sinke. Thermal cycling fiber metal laminates: considerations, test setup and results. *Proceedings of the 20th International Conference on Composite Materials, Copenhagen, Denmark*, pages 1–11, paper 4212–3, 2015.

[70] E. C. Botelho, R. S. Almeida, L. C. Pardini, and M. C. Rezende. Elastic properties of hygrothermally conditioned glare laminate. *International Journal of Engineering Science*, 45(1):163–172, 2007.

[71] A. da Costa, D. da Silva, D. Travessa, and E. C. Botelho. The effect of thermal cycles on the mechanical properties of fiber-metal laminates. *Materials and Design*, 42:434–440, 2012.

[72] H. Biermann and L. Krüger. *Moderne Methoden der Werkstoffprüfung*. John Wiley & Sons, Weinheim, 2014.

[73] M. Sadighi, R. C. Alderliesten, and R. Benedictus. Impact resistance of fiber-metal laminates: A review. *International Journal of Impact Engineering*, 49:77–90, 2012.

[74] G. Caprino, G. Spataro, and S. Del Luongo. Low-velocity impact behaviour of fibreglass–aluminium laminates. *Composites Part A: Applied Science and Manufacturing*, 35(5):605–616, 2004.

[75] B. Liaw, Y. Liu, and E. Villars. Impact damage mechanisms in fiber-metal laminates. *Proceedings of the SEM Annual Conference on Experimental and Applied Mechanics, Portland, USA*, pages 536–539, 2001.

[76] M. de Freitas and L. Reis. Failure mechanisms on composite specimens subjected to compression after impact. *Composite Structures*, 42(4):365–373, 1998.

[77] F. Bagnoli, M. Bernabei, D. Figueroa-Gordon, and P. E. Irving. The response of aluminium/glare hybrid materials to impact and to in-plane fatigue. *Materials Science and Engineering: A*, 523(1):118–124, 2009.

[78] G. Wu, J.-M. Yang, and H. Hahn. The impact properties and damage tolerance and of bi-directionally reinforced fiber metal laminates. *Journal of Materials Science*, 42(3):948–957, 2007.

[79] F. D. Morinière, R. C. Alderliesten, M. Sadighi, and R. Benedictus. An integrated study on the low-velocity impact response of the glare fibre-metal laminate. *Composite Structures*, 100:89–103, 2013.

[80] K. N. Shivakumar. Prediction of impact force and duration during low velocity impact on circular composite laminates. *Journal of Applied Mechanics*, 52(3):674–680, 1983.

[81] M. Sadighi, T. Pärnänen, R. C. Alderliesten, M. Sayeaftabi, and R. Benedictus. Experimental and numerical investigation of metal type and thickness effects on the impact resistance of fiber metal laminates. *Applied Composite Materials*, 19(3-4):545–559, 2012.

[82] N. Tai, M. Yip, and J. Lin. Effects of low-energy impact on the fatigue behavior of carbon/epoxy composites. *Composites Science and Technology*, 58(1):1–8, 1998.

[83] S. Dietrich, J. Kuppinger, P. Elsner, and K. Weidenmann. Small mass impact testing of sandwich structures. *Materials Testing*, 52(11-12):765–770, 2010.

[84] W. J. Cantwell, P. T. Curtis, and J. Morton. Impact and subsequent fatigue damage growth in carbon fibre laminates. *International Journal of Fatigue*, 6(2):113–118, 1984.

[85] A. Kinsey, D. E. J. Saunders, and C. Soutis. Post-impact compressive behaviour of low temperature curing woven cfrp laminates. *Composites*, 26(9):661–667, 1995.

[86] X. Zhang, L. Hounslow, and M. Grassi. Improvement of low-velocity impact and compression-after-impact performance by z-fibre pinning. *Composites Science and Technology*, 66(15):2785–2794, 2006.

[87] A. Busch and R. Brandt. Development and characterization of a composite material made up by glass fiber reinforced plastics and high strength steel. *Proceedings of the 21st International Conference on Composite Materials, Xi'an, China*, pages 3541–3553, 2017.

[88] Y. Liu, A. Yaghoubi, and B. Liaw. Low-velocity impact study on glare fmls using various indenters. *Journal of Aerospace Engineering*, 27(2):325–335, 2014.

[89] W. Hufenbach, F. Marques Ibraim, A. Langkamp, R. Böhm, and A. Hornig. Charpy impact tests on composite structures – an experi-

mental and numerical investigation. *Composite Science and Technology*, 68(12):2391–2400, 2008.

[90] R. Alderliesten and C. Rans. The meaning of threshold fatigue in fibre metal laminates. *International Journal of Fatigue*, 31(2):213–222, 2009.

[91] R. Alderliesten, J. Schijve, and S. van der Zwaag. Application of the energy release rate approach for delamination growth in glare. *Engineering Fracture Mechanics*, 73(6):697–709, 2006.

[92] A. Vlot. *High strain rate tests on fibre metal laminates*. TU Delft, Netherlands, Faculty of Aerospace Engineering, Report LR-800, 1998.

[93] R. Alderliesten and J. Homan. Fatigue and damage tolerance issues of glare in aircraft structures. *International Journal of Fatigue*, 28(10):1116–1123, 2006.

[94] T. Austin, M. Singh, P. Gregson, and P. Powell. Characterization of fatigue crack growth and related damage mechanisms in frp - metal hybrid laminates. *Composite Science and Technology*, 68(6):1399–1412, 2008.

[95] D. Shim, R. Alderliesten, S. Spearing, and D. Burianek. Fatigue crack growth prediction in glare hybrid laminates. *Composites Science and Technology*, 63(12):1759–1767, 2003.

[96] S. Suresh. *Fatigue of materials*. Cambridge University Press, Cambridge, United Kingdom, 1998.

[97] D. Radaj and M. Vormwald. *Ermüdungsfestigkeit: Grundlagen für Ingenieure*. Springer-Verlag, Berlin Heidelberg, 2007.

[98] J. Morrow. Cyclic plastic strain energy and fatigue of metals. *Internal friction, damping, and cyclic plasticity*, pages 45–87. ASTM International, West Conshohocken, USA, 1965.

[99] O. Basquin. The exponential law of endurance tests. *Proceedings of the Annual Meeting of the American Society for Testing Materials*, 10:625–630, 1910.

[100] ISO 13003:2003. Fibre-reinforced plastics–determination of fatigue properties under cyclic loading conditions. 2003.

[101] R. Khan. *Delamination growth in composites under fatigue loading*. Doctoral thesis, TU Delft, Netherlands, 2013.

[102] A. Poursartip, M. Ashby, and P. Beaumont. The fatigue damage mechanics of a carbon fibre composite laminate: development of the model. *Composites Science and Technology*, 25(3):193–218, 1986.

[103] S. Garcea, M. Mavrogordato, A. Scott, I. Sinclair, and S. Spearing. Fatigue micromechanism characterisation in carbon fibre reinforced polymers using synchrotron radiation computed tomography. *Composites Science and Technology*, 99:23–30, 2014.

[104] J.-M. Berthelot. Transverse cracking and delamination in cross-ply glass-fiber and carbon-fiber reinforced plastic laminates: Static and fatigue loading. *Applied Mechanics Reviews*, 56(1):111–147, 2003.

[105] S. Ogin, P. Smith, and P. Beaumont. Matrix cracking and stiffness reduction during the fatigue of a (0/90)s gfrp laminate. *Composites Science and Technology*, 22(1):23–31, 1985.

[106] C. Qian. *Multi-scale modelling of fatigue of wind turbine rotor blade composites*. Doctoral thesis, TU Delft, Netherlands, 2013.

[107] F. Lahuerta Calahorra. *Thickness effect in composite laminates in static and fatigue loading*. Doctoral thesis, TU Delft, Netherlands, 2017.

[108] P. Hähner, C. Rinaldi, V. Bicego, E. Affeldt, T. Brendel, H. Andersson, T. Beck, H. Klingelhöffer, H.-J. Kühn, A. Köster, M. Loveday,

M. Marchionni, and C. Rae. Research and development into a european code-of-practice for strain-controlled thermo-mechanical fatigue testing. *International Journal of Fatigue*, 30(2):372–381, 2008.

[109] V. Bellenger, A. Tcharkhtchi, and P. Castaing. Thermal and mechanical fatigue of a pa66/glass fibers composite material. *International Journal of Fatigue*, 28(10):1348–1352, 2006.

[110] M. Jen, Y. Tseng, and W. Lin. Thermo-mechanical fatigue of centrally notched and unnotched as-4/peek apc-2 composite laminates. *International Journal of Fatigue*, 28(8):901–909, 2006.

[111] L. Qian, Z. Wang, H. Toda, and T. Kobayashi. High temperature low cycle fatigue and thermo-mechanical fatigue of a 6061al reinforced with sicw. *Materials Science and Engineering: A*, 291(1):235–245, 2000.

[112] W. Schütz and H. Zenner. Schadensakkumulationshypothesen zur lebensdauervorhersage bei schwingender beanspruchung. teil 1: Ein kritischer überblick. *Materialwissenschaft und Werkstofftechnik*, 4(1):25–33, 1973.

[113] P. Chang, P. Yeh, and J. Yang. Fatigue crack initiation in hybrid boron/glass/aluminum fiber metal laminates. *Materials Science and Engineering: A*, 496(1):273–280, 2008.

[114] Z. Hashin and A. Rotem. A fatigue failure criterion for fiber reinforced materials. *Journal of Composite Materials*, 7(4):448–464, 1973.

[115] W. Hwang and K. Han. Fatigue of composites–fatigue modulus concept and life prediction. *Journal of Composite Materials*, 20(2):154–165, 1986.

[116] K. Jespersen, Y. Wang, J. Zangenberg, T. Lowe, P. Withers, and L. Mikkelsen. Ex-situ time-lapse x-ray ct study of 3d micro-structural

fatigue damage evolution in uni-directional composites. *Proceedings of the 17th European Conference on Composite Materials, München*, 17:5149–5156, 2016.

[117] B. Harris, N. Gathercole, H. Reiter, and T. Adam. Fatigue of carbon-fibre-reinforced plastics under block-loading conditions. *Composites Part A: Applied Science and Manufacturing*, 28(4):327–337, 1997.

[118] N. Gathercole, H. Reiter, T. Adam, and B. Harris. Life prediction for fatigue of t800/5245 carbon-fibre composites: I. constant-amplitude loading. *International Journal of Fatigue*, 16(8):523–532, 1994.

[119] T. Adam, G. Fernando, R.F. Dickson, H. Reiter, and B. Harris. Fatigue life prediction for hybrid composites. *International Journal of Fatigue*, 11(4):233–237, 1989.

[120] H. Hosseini-Toudeshky, M. Sadighi, and A. Vojdani. Effects of curing thermal residual stresses on fatigue crack propagation of aluminum plates repaired by fml patches. *Composite Structures*, 100:154–162, 2013.

[121] T. Sinmazcelik, E. Avcu, M. Bora, and O. Coban. A review: Fibre metal laminates, background, bonding types and applied test methods. *Materials and Design*, 32(7):3671–3685, 2011.

[122] M. Kawai, A. Hachinohe, K. Takumida, and Y. Kawase. Off-axis fatigue behaviour and its damage mechanics modelling for unidirectional fibre–metal hybrid composite: Glare 2. *Composites Part A: Applied Science and Manufacturing*, 32(1):13–23, 2001.

[123] N. Tsartsaris, M. Meo, F. Dolce, U. Polimeno, M. Guida, and F. Marulo. Low-velocity impact behavior of fiber metal laminates. *Journal of Composite Materials*, 45(7):803–814, 2011.

[124] A. Vlot. Impact loading on fibre metal laminates. *International Journal of Impact Engineering*, 18(3):291–307, 1996.

[125] T. Takamatsu, T. Matsumura, N. Ogura, T. Shimokawa, and Y. Kakuta. Fatigue crack growth properties of a glare3-5/4 fiber/metal laminate. *Engineering Fracture Mechanics*, 63(3):253–272, 1999.

[126] C. Sun, A. Dicken, and H. Wu. Characterization of impact damage in arall laminates. *Composites Science and Technology*, 49(2):139–144, 1993.

[127] S. Song, Y. Byun, T. Ku, W. Song, J. Kim, and B. Kang. Experimental and numerical investigation on impact performance of carbon reinforced aluminum laminates. *Journal of Materials Science & Technology*, 26(4):327–332, 2010.

[128] J. Fleischer, S. Roth, and C. Sommer. Faser-metall-gummi-hybridlaminate. *ZWF Zeitschrift für wirtschaftlichen Fabrikbetrieb*, 111(9):483–486, 2016.

[129] Hexcel Corporation. *Product data sheet HexPly M77/42%/UD90/CHS*, 2009.

[130] Cambridge Engineering Selector by Granta Design Limited. *Material data sheet aluminum 2024-T3*, 2017.

[131] Kraiburg Holding GmbH & Co. KG. *Product data sheet Kraibon SAA9579/52*, 2014.

[132] Kraiburg Holding GmbH & Co. KG. *Manufacturing data sheet Kraibon SAA9579/52*, 2012.

[133] Hexcel Corporation. *Manufacturing data sheet HexPly M77*, 2014.

[134] DIN EN ISO 527-5:1997. 1997.

[135] DIN EN ISO 14126:1999. *Bestimmung der Druckeigenschaften in der Laminatebene*, 1999.

[136] DIN EN ISO 14125:2011. Faserverstärkte kunststoffe bestimmung der biegeeigenschaften. 2011.

[137] ASTM D5528-13 Standard. Standard test method for mode i interlaminar fracture toughness of unidirectional fiber-reinforced polymer matrix composite. 2007.

[138] DIN EN ISO 6603-2:2000. Kunststoffe–bestimmung des durchstoßverhaltens von festen kunsstoffen, instrumentierter schlagversuch. 2000.

[139] DIN EN ISO 9227:2017. Korrosionsprüfungen in künstlichen atmosphären–salzsprühnebelprüfungen. 2017.

[140] DIN EN ISO 179:2006. *Kunststoffe–Bestimmung der Charpy-Schlageigenschaften*, 2010.

[141] DIN ISO 18352:2017. *Kohlenstofffaserverstärkte Kunststoffe - Ermittlung der Compression-After-Impact-Eigenschaften bei spezifischer Aufprallenergie*, 2017.

[142] J. Berthelot, M. Assarar, Y. Sefrani, and A. El Mahi. Damping analysis of composite materials and structures. *Composite Structures*, 85(3):189–204, 2008.

[143] Quick-Ohm Kuepper & Co. GmbH. *Product data sheet peltier element QC-241-1.6-20.0 MM*, 2015.

[144] J. Schindelin, I. Arganda-Carreras, E. Frise, V. Kaynig, M. Longair, T. Pietzsch, S. Preibisch, C. Rueden, S. Saalfeld, B. Schmid, et al. Fiji: an open-source platform for biological-image analysis. *Nature methods*, 9(7):676, 2012.

[145] M.H. Beheshty, B. Harris, and T. Adam. An empirical fatigue-life model for high-performance fibre composites with and without impact damage. *Composites Part A: Applied Science and Manufacturing*, 30(8):971–987, 1999.

Own publications

[146] M. Stoll and K. Weidenmann. Materials selection for a fiber-metal-laminate with elastomer interlayers. *Proceedings of the 21st International Conference on Composite Materials, Xi'an, China*, pages 3795–3801, 2017.

[147] M. Stoll and K. Weidenmann. Characterization of interface properties of fiber-metal-laminates (fml) with optimized interfaces. *Proceedings of the Euro Hybrid Materials and Structures, Kaiserslautern*, pages 38–43, 2016.

[148] M. Stoll and K. Weidenmann. The impact of environmental stress on the mechanical behavior of fiber-metal-laminates with elastomer interlayers (fmel). *Proceedings of the 17th European Conference on Composite Materials, München*, 17:4870–4876, 2016.

[149] M. Stoll, F. Stemmer, S. Ilinzeer, and K. Weidenmann. Optimization of corrosive properties of carbon fiber reinforced aluminum laminates due to integration of an elastomer interlayer. *Key Engineering Materials*, 742:287–293, 2017.

[150] M. Stoll and K. Weidenmann. Fatigue of fiber-metal-laminates with aluminum core, cfrp face sheets and elastomer interlayers (fmel). *International Journal of Fatigue*, 107:110–118, 2018.

[151] M. Stoll, V. Sessner, M. Kramar, J. Technau, and K. Weidenmann. The effect of an elastomer interlayer thickness variation on the mechanical properties of fiber-metal-laminates (in review). *Composite Structures*, 2018.

[152] S. Roth, M. Stoll, S. Coutandin, K. Weidenmann, and J. Fleischer. A new process route for the manufacturing of highly formed fiber-metal-laminates with elastomer interlayers (fmel) (in review). *Journal of Materials Processing Technology*, 2018.